

博士論文

Doctoral Dissertation

Time Dependent Charge-Parity Violation in  $B^0 \rightarrow K_s^0 K_s^0 K_s^0$  in Belle

II early operation

(Belle II 初期データを使った  $B^0 \rightarrow K_S^0 K_S^0 K_S^0$  崩壊の時間に依存する  
荷電・パリティ非保存の研究)

令和2年12月博士(理学)申請

A Dissertation Submitted for the Degree of Doctor of Philosophy

December 22nd, 2020

東京大学大学院理学系研究科物理学専攻

Department of Physics, Graduate School of Science,  
The University of Tokyo

万 琏

Wan Kun



**Time Dependent Charge-Parity Violation in  $B^0 \rightarrow K_s^0 K_s^0 K_s^0$  in  
Belle II early operation**

by

Kun Wan

Submitted to the Department of Physics  
on December 22nd, 2020, in partial fulfillment of the  
requirements for the degree of  
Doctor of Philosophy

**Abstract**

Belle II experiment is a next-generation B-factory experiment that is aimed to search for New Physics. Most of data will be collected at the  $\Upsilon(4S)$  resonance using SuperKEKB facility. It's designed at luminosity of  $8 \times 10^{35} \text{ cm}^{-2}\text{s}^{-1}$  which is 40 times higher than its predecessor KEKB.

The thesis is based on the time dependent  $CP$  violation study of  $B^0 \rightarrow K_S^0 K_S^0 K_S^0$  decay. The purpose is to precisely measure the  $CP$  parameters  $\mathcal{S}$  and  $\mathcal{A}$  in penguin-dominated  $b \rightarrow s$  transition. It's sensitive to New Physics effects and quite interesting compared to other modes with tree-level contamination. Any undisputed deviation on  $CP$  parameters could be a signal beyond the Standard Model. Such precise measurements mainly require clean signal extraction,  $B^0$  vertex reconstruction, flavor tagging and proper decay time resolution modeling. This thesis covers the development and optimization of analysis tools on the four aspects above. The blind fit and toy MC study are also included before using data, which show a reasonably good consistence in  $CP$  parameter measurements. By using data from Belle II 2019 and 2020 (Spring and Summer) operation at about  $62.8 \text{ fb}^{-1}$  integral luminosity, the measurement results of  $\mathcal{S}$  and  $\mathcal{A}$ :  $\mathcal{S} = -\sin(2\phi_1) = -0.82 \pm 0.85 \text{ (stat)} \pm 0.07 \text{ (syst)}$  and  $\mathcal{A} = -0.21 \pm 0.28 \text{ (stat)} \pm 0.06 \text{ (syst)}$  are obtained. The result is dominated by statistical uncertainty and currently consistent with the Standard Model and the previous results in Babar and Belle.

Thesis Supervisor: Hiroaki Aihara  
Title: Professor



# Contents

<b>1</b>	<b>Introduction</b>	<b>9</b>
1.1	The Standard Model . . . . .	9
1.2	Symmetry Violation . . . . .	11
1.3	CKM mechanism . . . . .	14
1.4	Time Dependent $CP$ violation . . . . .	19
1.4.1	$CP$ violation in neutral B system . . . . .	19
1.4.2	$\phi_1$ from $B^0 \rightarrow J/\psi K_S^0$ . . . . .	22
1.4.3	$\phi_1$ from penguin-dominated mode $b \rightarrow q\bar{q}s$ . . . . .	23
1.4.4	$\phi_1$ from $B^0 \rightarrow K_S^0 K_S^0 K_S^0$ . . . . .	24
<b>2</b>	<b>Belle II Experiment</b>	<b>27</b>
2.1	Belle II and SuperKEKB overview . . . . .	27
2.2	Vertex detector (VXD) . . . . .	29
2.3	Central drift chamber (CDC) . . . . .	31
2.4	TOP and ARICH detectors . . . . .	32
2.5	Electromagnetic calorimeter (ECL) . . . . .	34
2.6	$K_L^0$ muon detector (KLM) . . . . .	35
2.7	Trigger and DAQ system . . . . .	35
2.8	Analysis Software . . . . .	37
2.8.1	BASF2 Core Structure . . . . .	38
2.8.2	Event Processing Workflow . . . . .	39
2.8.3	mDST structure . . . . .	41
2.8.4	Conditional Database . . . . .	42

2.9	Belle II simulation . . . . .	44
2.10	Belle II data taking . . . . .	47
<b>3</b>	<b><math>K_S^0</math> Reconstruction Study</b>	<b>49</b>
3.1	Cut-based $K_S^0$ Reconstruction . . . . .	50
3.2	MVA-based $K_S^0$ Identification: KsFinder . . . . .	52
3.2.1	Experience from Belle . . . . .	52
3.2.2	FastBDT algorithm . . . . .	54
3.2.3	Decay Topology of $K_S^0 \rightarrow \pi^+ \pi^-$ . . . . .	56
3.2.4	Determination of training observables from $K_S^0$ decay . . . . .	59
3.2.5	Training, Testing and Application of KsFinder . . . . .	62
3.2.6	The Performance and Over-fitting check . . . . .	62
3.2.7	Data Validation for Classifier . . . . .	66
3.2.8	KsFinder Effects on Kinematics Evaluation . . . . .	68
3.2.9	Summary . . . . .	70
<b>4</b>	<b>Analysis Strategies</b>	<b>71</b>
4.1	Data Sample and Event Selection . . . . .	71
4.1.1	$K_S^0$ Selection . . . . .	72
4.1.2	$B^0$ Signal Reconstruction . . . . .	76
4.1.3	Continuum Suppression . . . . .	78
4.1.4	Resonance Background . . . . .	84
4.1.5	$B\bar{B}$ background and self-cross feed . . . . .	85
4.1.6	Signal Extraction . . . . .	87
4.1.7	Kinematics and Vertexing Dependence on KsFinder . . . . .	94
4.1.8	Summary . . . . .	99
<b>5</b>	<b><math>CP</math> Parameters measurement</b>	<b>101</b>
5.1	Vertex Resolution Model . . . . .	102
5.1.1	$CP$ -side resolution function . . . . .	102
5.1.2	Tag-side resolution function . . . . .	106

5.1.3	Background events distribution . . . . .	108
5.2	Flavor Tagging . . . . .	110
5.3	<i>CP</i> Fitter . . . . .	114
5.4	Blind Fit . . . . .	115
5.4.1	<i>CP</i> fit on MC samples . . . . .	115
5.4.2	Linearity Test . . . . .	117
5.4.3	Toy MC Fit Pull . . . . .	118
5.4.4	Lifetime and $\Delta m_d$ Fit . . . . .	119
5.5	<i>CP</i> fit on data . . . . .	121
5.6	Systematic Uncertainty . . . . .	121
5.7	Summary . . . . .	125
<b>6</b>	<b>Conclusion and Prospective</b>	<b>127</b>
<b>A</b>	<b>Training Observables for <math>K_S^0</math> Classifier</b>	<b>131</b>
<b>B</b>	<b>Data Validation Plots for <math>K_S^0</math></b>	<b>135</b>
<b>C</b>	<b><math>K_S^0</math> mass fit with varied cut value</b>	<b>139</b>



# Chapter 1

## Introduction

### 1.1 The Standard Model

In the classical view of our physical world, even from the very early phase of human's history of understanding the universe, people have been convinced that all matter is made of some fundamental elements, and studying the elementary structure of the matter along with the interaction between those elements help us better understand the world and innovates the new technologies that deeply changes human society. Compared to the rather long history we start to think about question : what's the matter made? We only approached a mostly correct yet not perfectly precise answer of this old puzzle in the recent decades. Thanks to a few generation marvelously talented physicists' efforts, the Standard Model ( SM ) was built in the late 70th of 20th century, which describes the matter and interactions using an incredibly nice-looking table that contains a bunch of fundamental particles in two categories - fermions and bosons.

The fermions are the ones that assemble the matter and the bosons are for mediating the force between the fermions. They also have an essential difference in its spin number, which presents the different statistics rules they have to follow when describing their field functions.

In the fermion family, there are six leptons, classified based on their charge ( $Q$ ), electron number ( $L_e$ ), muon number ( $L_\mu$ ) and tau number ( $L_\tau$ ). Similarly, there are

also six “flavors” of quarks, which are classified based on their charge, strangeness ( $S$ ), charm( $C$ ), beauty( $B$ ) and truth ( $T$ ). The last two can also be called as “bottom” and “top” number. Unlike leptons, quarks are all fractional charged, which naturally divides them into two sides. All up-side quarks have  $+\frac{2}{3}$  unit charge and all down-side quarks have  $-\frac{1}{3}$ . Besides, all quarks are colored, meaning each one of them has an inner quantum number presenting 3 kinds of colors. One thing obvious is that all these fermions have its own antimatter correspondences, with all these quantum number reverse-signed but leaving mass identical valued. This comes to a fact that there are 36 different particles of them in total. According to the leptons and quarks flavors, charge and lepton numbers, they nicely fit in 3 generations, as Figure 1-1 shows.

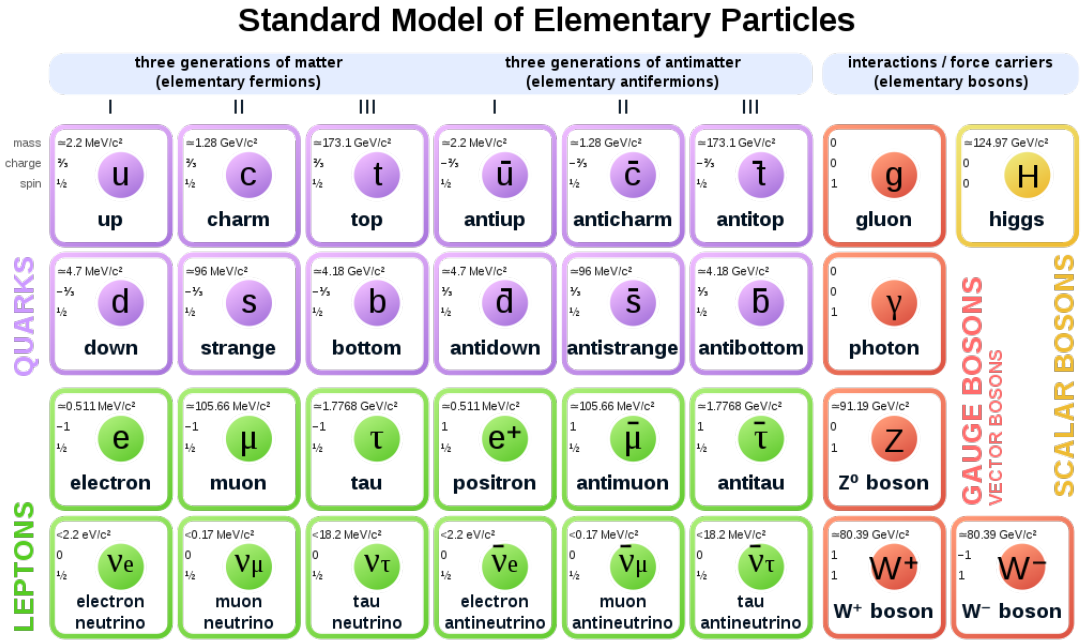


Figure 1-1: Elementary particles in the Standard Model.[1]

The SM not only accounts for the matter composition, but also explains the interaction of fermions and bosons in a picture where they interact through exchange of certain force carriers which are bosons as well. More specifically, each set of these carriers mediate one type of fundamental interaction. The force in which most of classical objects interact is electromagnetic interaction and it's mediated by photons.

The force that plays a role in the  $\beta$  decay is weak interaction, of which the mediators are  $W$  and  $Z$  bosons. When a proton and a neutron interact within a nuclei transforming into each other, the actual force carriers are 8 types of gluons (or  $\pi$  mesons between nucleus), and it's called strong force. Last but not least, in the quantum field theory, all of these particles has zero mass if there's no spontaneous symmetry breaking by introducing one another boson - Higgs boson, in the Lagrangian formalism of all interactions. With this being said, the "mass" is taken as the weight of how strong all these particles interact with Higgs field.

This complete set of elementary particles describes the whole picture of the Standard Model. It leads to a comprehensive and symmetric theory of fundamentals in particle dynamics. However, the SM prediction does not perfectly match with experimental observations. Since the day theory was built, generations of particle physics experiments have been searching for evidences beyond the SM, as known as New Physics (NP). New Physics is expected to unfold a more profound truth of nature which hopefully explains these observed mismatches. The studies on these fields naturally draw a large attention from modern physicists, focusing on discovering and explaining the mismatches between the SM predictions and experiments. Among these research fields, the studies of symmetry violations (or called as asymmetries) plays an important role. The studies of symmetries was once the driving force for physicists when building the modern theory about particle physics. It is no wonder that now the violation of symmetries, which physicists didn't expect to happen , has become the cutting edge research topics for New Physics.

## 1.2 Symmetry Violation

Symmetries have been one of the focuses in modern physics research since physicists found the internal link between symmetries and conservation laws. The invariance of physical system under infinitesimal transformation is regarded as "continuous symmetry". For instance, any infinitesimal shift on space and time holds physics law in the same form, which implies the physical processes should hold the conservation

law of momentum and energy. Such statement is stated as “Noether’s theorem”[2]. Symmetries become a powerful tool in discovering physics laws due to this reason. When the known symmetries are found to be broken, it usually leads to a discovery of the new theory.

There are three types of discrete symmetric operations which play important roles in particle physics. Charge-conjugation  $C$  is the operation that turns particle to its anti-particle. Parity transformation  $P$  is the one that puts a negative sign before all the spatial related vector such as  $\vec{r} \rightarrow -\vec{r}$ , feeling like look at a physical process in a mirror. The time-reversing operation  $T$  is to reversely proceed a physical process backward time. Physicists are convinced that each of these three kinds of symmetric operations makes no change to any physical system. In 1950s, Lee and Yang [3] first questioned that parity symmetry might be broken in weak interactions. They offered a few possible ways to test it and then by Wu [4], an observation on the  $\beta$  decay of  $^{60}\text{Co}$  was presented that the electrons emitted from  $^{60}\text{Co}$  decay prefer to flying against the direction of nuclear spin that can be control by the external magnetic field, see Figure 1-2.

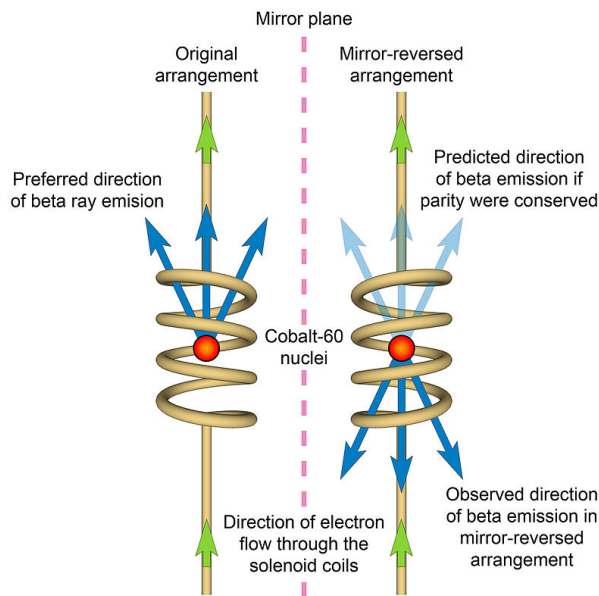


Figure 1-2:  $^{60}\text{Co}$  decay violates the parity because of the unbalance of electron emissions.

Soon, the fact that coupling of weak interaction only involves either neutrinos (left-

handed) or anti-neutrinos (right-handed) was realized. So  $C$  symmetry is also violated since no left-handed anti-neutrino was found which should be theocratically possible in weak interaction. But if one performs  $CP$  operation on such weak interaction involving neutrinos, then such process “seems” to be equally possible, indicating the conservation of  $CP$  in weak interaction for a moment.

The first evidence of  $CP$  violation was found in the Kaon system. Charged Kaon identification was called mystery of “ $\tau - \theta$ ”, because they yield different decay modes with different parity, but have identical mass between  $\tau$  and  $\theta$ . It turns out that they are both charged Kaon meson  $K^+$ , whose decay violates the conservation of  $CP$ . In the neutral Kaon system, Cronin and Fitch’s experiment was the first experiment that proves the violation of  $CP$ . They measured the decay products at 57 foot of a neutral kaon beamline assuming all the particle in the beam should be long lifetime  $K_L$ , nearly no  $K_S$ . But 0.002% of them decay through the  $K_L \rightarrow \pi^+ \pi^-$  ( $CP = 1$  in final states, yet  $K_L$  has  $CP = -1$ ). Given that the expected distance to have 0.002% of  $K_S$  at about speed of light is no more than 1 meter, such deviation at 57 foot is an obvious evidence that  $CP$  conservation is also violated in the neutral Kaon system.

In 1973, Kobayashi and Maskawa introduced the third generation of quarks, and the mixing of flavor eigenstates and weak eigenstates is described by a  $3 \times 3$  unitary matrix, which is called Cabibbo-Kobayashi-Maskawa (CKM) matrix[5]. The theory allows a free complex phase in CKM matrix and it accounts for the origin of  $CP$  asymmetries of weak interactions in the Standard Model. The experimental evidence of  $CP$  violation in  $b$  meson system was observed in 2001 by Belle and Babar Collaborations. They measured the time-dependent decay time difference of  $B$  and  $\bar{B}$  in the decay of  $B \rightarrow J/\psi K_S^0$ . This channel provided a outstandingly clearness in theoretical prediction and has relatively large branching fraction, thus it’s called the “golden mode”. In 2008, Kobayashi and Maskawa were rewarded the Nobel Prize to highly value their contribution in the discovery of the mechanism of the  $CP$  violation. The Belle experiment was regarded as a great success for validating the theory. Later in 2010, the upgrade of Belle, Belle II and the upgrade of KEK accelerator, SuperKEKB, were both approved by Japan to further push the understanding of  $CP$  violation in

$b$  sector along with other excitingly interesting topics in New Physics.

### 1.3 CKM mechanism

$$\Phi = \begin{pmatrix} \phi^+ \\ \nu + \frac{H+i\chi}{\sqrt{2}} \end{pmatrix} \quad (1.1)$$

Equation 1.1 is the Higgs potential doublets.  $H$ 's value is 174 GeV as the expected Higgs potential for vacuum and  $\phi$  and  $\chi$  are the pseudo-Goldstone fields which are appearing when introducing Higgs field  $\phi$  without breaking the gauge symmetry. The idea of introducing Higgs is to naturally solve the mass origin of particles under the gauge symmetry in the SM, as Equation 1.2 presents.

$$\mathcal{L}_{Yuk}^q = -Q^\dagger Y^d \Phi d'_R - Q^\dagger Y^u \epsilon \Phi^* u'_R + h.c. \quad (1.2)$$

Here the primed fields stand for the weak eigenstates of quarks.  $\epsilon$  is a  $2 \times 2$  matrix.  $Q^\dagger$  is the left-handed doublets that stand for weak eigenstates of up and down types quarks.

$$\epsilon = \begin{pmatrix} 0 & 1 \\ -1 & 0 \end{pmatrix} \quad (1.3)$$

$$Q = \begin{pmatrix} u' & d' \\ c' & s' \\ t' & b' \end{pmatrix}_L \quad (1.4)$$

Yukawa matrix is an arbitrary  $3 \times 3$  complex matrix  $Y^{u,d}$  which give the rise of two types of massive quark field  $M^{u,d} = Y^{u,d}\nu$ . The choosing the weak eigenstates makes these matrices un-diagnosed. So the “rotation” of weak eigenstates to diagnose them is done by:

$$S_{L,R}^u \begin{pmatrix} u' \\ c' \\ t' \end{pmatrix}_{L,R} = \begin{pmatrix} u \\ c \\ t \end{pmatrix}_{L,R} \quad (1.5)$$

$$S_{L,R}^d \begin{pmatrix} d' \\ s' \\ b' \end{pmatrix}_{L,R} = \begin{pmatrix} d \\ s \\ b \end{pmatrix}_{L,R} \quad (1.6)$$

In Equation 1.5 and 1.6,  $S_{L,R}^{u,d}$  are all unitary matrices since they are actually generated by the normalized eigenstate vectors of the Yukawa matrix, which means  $S_{L,R}^{u,d\dagger} S_{L,R}^{u,d} = I$ . The mass items  $M_q$ , arised after the “rotation” can be presented as:

$$\mathcal{L}_m = - \sum_{q=u,c,t,d,s,b} M_q q^\dagger q \quad (1.7)$$

where  $q = (q_L + q_R)$  is four-component Dirac field, and  $q_L^\dagger q_L = q_R^\dagger q_R = 0$ . The matrix  $S_{L,R}^{u,d}$  are contributing to the weak interactions as Equation 1.8 shows.

$$\mathcal{L}_W^q = \frac{g}{\sqrt{2}} \left[ \begin{pmatrix} \bar{u} & \bar{c} & \bar{t} \end{pmatrix}_L \gamma^\mu W_\mu^+ V_{CKM} \begin{pmatrix} d \\ s \\ b \end{pmatrix}_L + \begin{pmatrix} \bar{d} & \bar{s} & \bar{b} \end{pmatrix}_L \gamma^\mu W_\mu^- V_{CKM}^\dagger \begin{pmatrix} u \\ c \\ t \end{pmatrix}_L \right] \quad (1.8)$$

The Lagrangian hereby clearly declar the transition of different charged quarks through the coupling of charged current  $W^{+/}$ . Interestingly, such coupling only applies for the left-handed quarks. For example, a left-handed c quark only transits to left-handed s quark by giving out a  $W$  boson. If the Parity conjugation is applied to the Lagrangian, the left-handed quarks becomes right-handed. The same thing happens if the Charge conjugation is applied, cause it changes the chirality of the 4 components quark fields and charge sign at the same time. This means the weak interaction will not conserve the Parity and the Charge symmetries. However, if the  $CP$  conjugation is applied, all left-handed quark fields’ chirality are unchanged and

only the conjugation of quark fields are made, as Equation 1.9 shows.

$$\left(\bar{u} \quad \bar{c} \quad \bar{t}\right)_L \gamma^\mu W_\mu^+ V_{CKM} \begin{pmatrix} d \\ s \\ b \end{pmatrix}_L \Leftrightarrow \left(u \quad c \quad t\right)_L \gamma^\mu W_\mu^- V_{CKM} \begin{pmatrix} \bar{d} \\ \bar{s} \\ \bar{b} \end{pmatrix}_L \quad (1.9)$$

Comparing Equation 1.9 and 1.8, the  $CP$  symmetry requires:

$$u_L^i V_{ij} \bar{d}_L^j \gamma^\mu W_\mu^- = u_L^n V_{nm}^* \bar{d}_L^m \gamma^\mu W_\mu^- \quad (1.10)$$

The same indices  $ij$  and  $nm$  are summed over on both side. This is equivalent to:

$$V_{ij} = V_{ij}^* \quad (1.11)$$

On the one hand, if the CKM matrix is real,  $CP$  will be conserved in the weak interaction in the SM. On the other hand, from Equation 1.10, it's still possible to make Lagrangian unchanged even if  $V_{CKM}$  is not real. By introducing non-physical phases for each quark field  $u_L^k e^{(i\phi_{uk})}$  and  $d_L^j e^{(i\phi_{dj})}$ , the Equation 1.11 becomes:

$$V_{kj} e^{i(\phi_{dj} - \phi_{uk})} = V_{kj}^* e^{i(\phi_{uk} - \phi_{dj})} \quad (1.12)$$

Assuming the complex phase of CKM  $kj$ -th element is  $\theta_{kj}$ , it's obviously required that:

$$\theta_{kj} = \phi_{uk} - \phi_{dj} \quad (1.13)$$

Historically, before the 3rd generation of quarks is discovered,  $k, j$  can only be either 1 or 2, and  $V_{CKM}$  is 2 dimensional unitary matrix. With two generations of quarks, there are 8 real parameters in CKM matrix, 4 describe amplitudes and 4 describe complex phases. Unitary condition  $V_{CKM}^\dagger V_{CKM} = 1$  gives 4 equations, containing 2 real equations and 2 complex equations. The 2 complex equations are identical so only 3 independent equations arise. 2 complex equations leads to 2 equations about phases plus 2 equations are about amplitude. Based on this, the degree of freedom

of phases on 2 dimensional CKM matrix is  $4 - 2 = 2$ . Thus it's always possible to make CKM real by properly render the non-physical phases. This means with only existence of 2 generations of quarks, there is no spontaneous explanation for  $CP$  violation in the SM. When Kobayashi and Maskawa realized that this is no longer true if 3rd generation of quarks exists, they presented CKM matrix as a  $3 \times 3$  matrix. In such case, there will always be one irreducible complex phase parameter in the CKM matrix, which means  $CP$  symmetry is no longer conserved in the weak interactions.

The  $3 \times 3$  unitary CKM matrix can be written as Equation 1.14.

$$V_{CKM} = \begin{pmatrix} V_{ud} & V_{us} & V_{ub} \\ V_{cd} & V_{cs} & V_{cb} \\ V_{td} & V_{ts} & V_{tb} \end{pmatrix} \quad (1.14)$$

It can be parameterized:

$$V_{CKM} = \begin{pmatrix} c_{12}c_{13} & s_{12}c_{13} & s_{13}e^{-i\delta} \\ -s_{12}c_{23} - c_{12}s_{23}s_{13}e^{-i\delta} & c_{12}c_{23} - s_{12}s_{23}s_{13}e^{-i\delta} & s_{23}c_{13} \\ s_{12}s_{23} - c_{12}s_{23}s_{13}e^{-i\delta} & -c_{12}c_{23} - s_{12}c_{23}s_{13}e^{-i\delta} & c_{23}c_{13} \end{pmatrix} \quad (1.15)$$

where the  $c_{jk} = \cos(\theta_{jk})$  and  $s_{jk} = \sin(\theta_{jk})$ ,  $\delta$  is the irreducible complex phase. By measuring the relative branching ratio of  $b \rightarrow c$ ,  $s \rightarrow u$  and  $b \rightarrow u$  in a tree level transitions:

$$|V_{ub}| \ll |V_{cb}| \ll |V_{us}| \quad (1.16)$$

and the following relations are often used to simplify CKM matrix presentation:

$$s_{13} = \lambda, s_{23} = A\lambda^2, s_{13}e^{i\delta} = A\lambda^3(\rho - i\eta) \quad (1.17)$$

By using Equation 1.17, CKM matrix is parameterized as:

$$V_{CKM} = \begin{pmatrix} 1 - 1/2\lambda^2 & \lambda & A\lambda^3(\rho - i\eta) \\ -\lambda & 1 - 1/2\lambda^2 & A\lambda^2 \\ A\lambda^3(\rho - i\eta) & -A\lambda^2 & 1 \end{pmatrix} + \mathcal{O}(\lambda^4) \quad (1.18)$$

Using the unitary condition, the following equation is obtained.

$$1 + \frac{V_{ud}V_{ub}^*}{V_{cd}V_{cb}^*} + \frac{V_{td}V_{tb}^*}{V_{cd}V_{cb}^*} = 0 \quad (1.19)$$

Plotting the relation in a complex 2D plane using Equation 1.19,

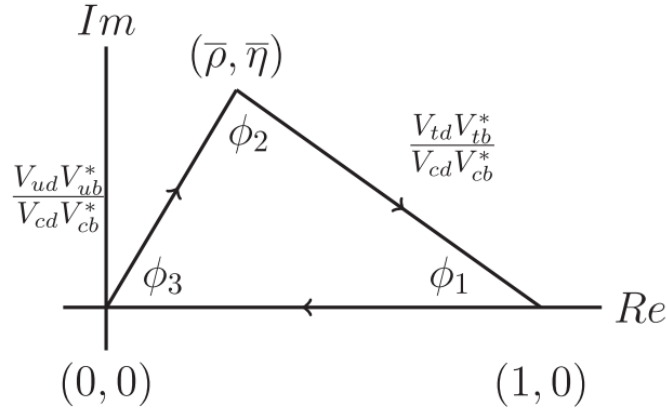


Figure 1-3: The unitary angles of CKM

$$\bar{\rho} + i\bar{\eta} = -\frac{V_{ud}V_{ub}^*}{V_{cd}V_{cb}^*} \quad (1.20)$$

$$1 - (\bar{\rho} + i\bar{\eta}) = -\frac{V_{td}V_{tb}^*}{V_{cd}V_{cb}^*} \quad (1.21)$$

These angles are obtained by drawing the  $(\bar{\rho}, \bar{\eta})$  on the complex coordinates, and they are also well-known in the names as:  $\phi_1 = \beta$ ,  $\phi_2 = \alpha$ ,  $\phi_3 = \gamma$ . The results presenting the measurement of CKM angles or  $(\bar{\rho}, \bar{\eta})$  in 2019 is shown in Figure 1-4.

The measurement of  $\phi_1$  and  $\phi_2$  are coming from the time-dependent  $CP$  violations (TDCPV).  $\phi_1$  in the tree-level dominated decays has been precisely measured thanks to the small hadronic uncertainties. FCNC process rises through the  $B_d^0 - \bar{B}_d^0$  mixing in

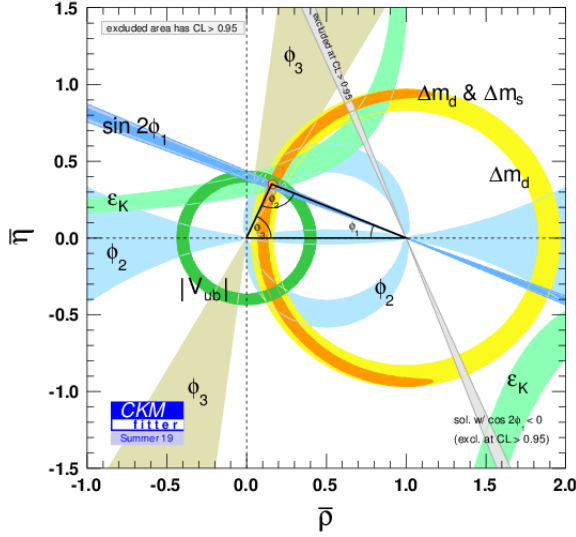


Figure 1-4: The CKM angles fit in the complex plane of  $\bar{\rho} - \bar{\eta}$ .[6]

box diagram, and it's believed that potential New Physics processes might contribute to the difference in between results of CKM angles measured from experiments. For example, angle  $\phi_1$  that is observed from tree-level dominated process like  $B^0 \rightarrow J/\psi K_s^0$  could be different from penguin-dominated  $b \rightarrow s$  transition. The Standard Model provides an approximated correction on how large the deviation might be, where it requires much precise measurement on each decay channel to validate the potential New Physics effect. The prospective large Belle II data and more precise time resolution performance will be much helpful to clear the tension in future.

## 1.4 Time Dependent $CP$ violation

### 1.4.1 $CP$ violation in neutral B system

The  $\phi_1, \phi_2$  and  $\phi_3$  are essentially measuring the CKM  $CP$  violating phase since there's only one complex phase in CKM and it can be determined by these 3 angles. And  $\phi_{1,2}$  are related to mostly in the time dependent decay rate difference. From Figure

1-3, one can obtain:

$$\phi_1 = \text{Arg}\left(-\frac{V_{td}V_{tb}^*}{V_{cd}V_{cb}^*}\right) \quad (1.22)$$

$$\phi_2 = \text{Arg}\left(-\frac{V_{td}V_{tb}^*}{V_{ud}V_{ub}^*}\right) \quad (1.23)$$

The general strategy to extract the  $\phi_{1,2}$  is to measure the time-dependent  $CP$  violation. The mass eigenstates which are driving the propagation of B meson states in the mixing are:  $|B\rangle_{H,L} = p|B\rangle \pm q|\bar{B}\rangle$ , where  $H$  and  $L$  stand for the larger and smaller eigenvalues corresponded states.  $|B\rangle$  and  $|\bar{B}\rangle$  are the flavor eigenstates. The Hamiltonian matrix can be written using flavor eigenstates:

$$M_\Gamma = \begin{bmatrix} m - i/2\Gamma & M_{12} - i/2\Gamma_{12} \\ M_{12}^* - i/2\Gamma_{12}^* & m - i/2\Gamma \end{bmatrix} \quad (1.24)$$

and the time evolution of mass eigenstates are defined as (using the notation of  $B_{H,L}$  as physical states at  $t = 0$ ):

$$B_H(t) = e^{-im_H t} e^{-\Gamma_H t/2} B_H \quad (1.25)$$

$$B_L(t) = e^{-im_L t} e^{-\Gamma_L t/2} B_L \quad (1.26)$$

where  $M_{H,L}$  and  $\Gamma_{H,L}$  are the masses and decay width of two mass eigenstates. By expanding the mass eigenstates using flavor eigenstates,

$$B(t) = (1/2p)e^{-im_H t} e^{-\Gamma_H t/2}(pB + q\bar{B}) + (1/2p)e^{-im_L t} e^{-\Gamma_L t/2}(pB - q\bar{B}) \quad (1.27)$$

$$\bar{B}(t) = (1/2q)e^{-im_H t} e^{-\Gamma_H t/2}(pB + q\bar{B}) - (1/2q)e^{-im_L t} e^{-\Gamma_L t/2}(pB - q\bar{B}) \quad (1.28)$$

and replacing  $g_\pm(t) = \frac{1}{2}(e^{-im_H t - \Gamma_H/2t} \pm e^{-im_L t - \Gamma_L/2t})$ , above two equations become:

$$B(t) = g_+(t)B + \frac{q}{p}g_-(t)\bar{B} \quad (1.29)$$

$$\bar{B}(t) = g_+(t)\bar{B} + \frac{p}{q}g_-(t)B \quad (1.30)$$

Considering all the phases space of the decay from flavor eigenstates to final states  $f(\bar{f})$  are included in the amplitudes  $\mathcal{A}_f(\bar{\mathcal{A}}_f)$ , one needs to expand the flavor eigenstates using such amplitude to have the differential decay rate  $\Gamma(B \rightarrow f, t)$ . From  $B(t) \propto \mathcal{A}_f \psi_f + h.c$  and  $(\bar{B}(t) \propto \bar{\mathcal{A}}_f \psi_{\bar{f}} + h.c)$ :

$$\Gamma(B \rightarrow f, t) = |\mathcal{A}_f|(|g_+(t)|^2 + |\lambda_f|^2 |g_-(t)|^2 + 2\text{Re}(\lambda_f g_+^*(t) g_-(t))), \quad (1.31)$$

$$\Gamma(\bar{B} \rightarrow \bar{f}, t) = |\bar{\mathcal{A}}_f|(|g_+(t)|^2 + |\bar{\lambda}_{\bar{f}}|^2 |g_-(t)|^2 + 2\text{Re}(\bar{\lambda}_{\bar{f}} g_+^*(t) g_-(t))) \quad (1.32)$$

where the parameter  $\lambda_f$  is

$$\lambda_f \equiv (q/p)(\bar{\mathcal{A}}_f / \mathcal{A}_f) \quad (1.33)$$

$$\bar{\lambda}_{\bar{f}} \equiv (q/p)(\mathcal{A}_{\bar{f}} / \bar{\mathcal{A}}_{\bar{f}}) \quad (1.34)$$

$q/p$  is introduced by the coefficient of mass eigenstates from weak eigenstates. Using the Hamiltonian matrix,  $q/p$  can be presented as:

$$q/p = \frac{\Delta M - i/2\Delta\Gamma}{2(M_{12} - i/2\Gamma_{12})} \quad (1.35)$$

where the  $M_{12}$  and  $\Gamma_{12}$  stands for the contribution of non-diagnosed term in the Hamiltonian matirx.  $\Delta M = M_H - M_L$  and  $\Delta\Gamma = \Gamma_H - \Gamma_L$  are the difference of mass and decay width for two mass eigenstates. It's obvious that if  $|\mathcal{A}_f| \neq |\bar{\mathcal{A}}_{\bar{f}}|$ , direct  $CP$  violation will occur.

The time-dependent decay rate difference is defined as Equation 1.36:

$$\begin{aligned} A_{CP}(t) &\equiv \frac{\Gamma(B \rightarrow f, t) - \Gamma(\bar{B} \rightarrow \bar{f}, t)}{\Gamma(B \rightarrow f, t) + \Gamma(\bar{B} \rightarrow \bar{f}, t)} \\ &= \frac{S_f \sin(\Delta M t) - A_f \cos(\Delta M t)}{\cosh(\Delta\Gamma t/2) + A_{\Delta\Gamma}^f \sinh(\Delta\Gamma t/2)} \end{aligned} \quad (1.36)$$

, where

$$\mathcal{S} = \frac{2\text{Im}(\lambda_f)}{1 + |\lambda_f|^2}; \mathcal{A} = \frac{1 - |\lambda_f|^2}{1 + |\lambda_f|^2}; A_{\Delta\Gamma}^f = -\frac{2\text{Re}(\lambda_f)}{1 + |\lambda_f|^2} \quad (1.37)$$

The origin of time is set to the flavor tagged moment. The time-dependent CP

violation parameters are  $\mathcal{S}$  and  $\mathcal{A}$ , which are determined by  $\lambda_f$ .

### 1.4.2 $\phi_1$ from $B^0 \rightarrow J/\psi K_S^0$

If final states are  $CP$  definite, the amplitude then equals to:  $\mathcal{A}_f \equiv \langle f | H | B \rangle$  and  $\bar{\mathcal{A}}_f \equiv \langle f | H | \bar{B} \rangle$ . In  $B_d^0 - \bar{B}_d^0$ ,  $q/p$  can be treated as  $e^{i\phi_d}$  safely as pure phase term. This relative phase accounts the transition from  $b$  to up-type quarks to  $s$  in mixing, so it can be presented as  $\phi_d = \text{Arg}(V_{td}^* V_{tb}) / (V_{tb}^* V_{td}) \approx 2\phi_1$  based on negligible correction to the SM. In the golden mode  $B^0 \rightarrow J/\psi K_S^0$ , considering  $\Delta\Gamma$  can be treated as zero safely in the Standard Model[7] in this case, Equation 1.36 can be reduced to:

$$A_{CP}(t) = \mathcal{S}\sin(\Delta M t) - \mathcal{A}\cos(\Delta M t) \quad (1.38)$$

For decay amplitude, which receive contribution from tree-level and loop-level processes shown in Figure 1-5 ,

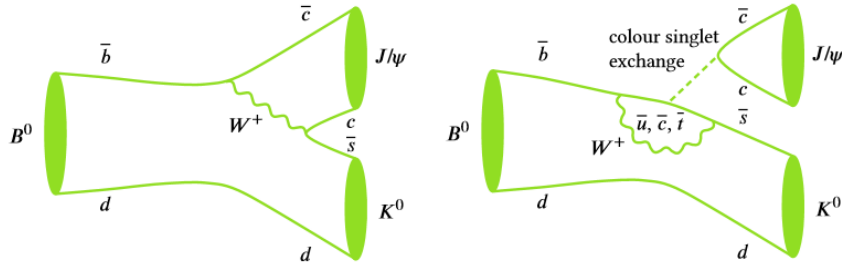


Figure 1-5: The dominated tree-level (left) and the suppressed loop-level (right) of  $B \rightarrow J/\psi K^0$ , in which  $K^0$  particles are detected  $K_S^0$ . [8]

Using the relation  $|V_{ub}| \ll |V_{cb}| \ll |V_{us}| < |V_{cs}|$ , it's obvious that  $V_{ub}^* V_{us} \ll V_{cb}^* V_{cs}$ , so the penguin-mode is suppressed in the Standard Model. Defining  $\eta_f$  as the  $CP$  eigenvalue for  $CP$  definite final states,

Given  $\eta_f = 1$  and  $|\lambda_f| = 1$  in  $B^0 \rightarrow J/\psi K_S^0$ , from 1.37,  $CP$  parameters can be presented as:

$$\mathcal{S} = \text{Im}(\lambda_f) = -\sin(\phi_d)\eta_f = -\sin(2\phi_1); \mathcal{A} = 0 \quad (1.39)$$

From Equation 1.39 ,  $\phi_1$  can be accessed pretty precisely in the measurement of time-dependent  $CP$  violation in  $B^0 \rightarrow J/\psi K_S^0$ , whose branching fraction is relatively

high.

### 1.4.3 $\phi_1$ from penguin-dominated mode $b \rightarrow q\bar{q}s$

Compared to  $B^0 \rightarrow J/\psi K_S^0$  channel, the measurement of  $\mathcal{S}$  and  $\mathcal{A}$  from penguin-dominated channels through  $b \rightarrow q\bar{q}s$  where  $q$  is  $u, d, s$  can be different due to the varied tree-to-penguin amplitude ratio. Furthermore, they are quite interesting for the following reasons[9]. First, they can probe  $B^0 - \bar{B}^0$  through different short-distance vertices than the tree-level dominated decays. Second, the relatively small penguin amplitude may be more sensitive to the NP effects than tree-dominated modes. Last but not least, they comprise a large number of different final states, which can help disentangling non-perturbation long-distance physics from short-distance information, such as  $\phi_1$  or NP contributions to the weak Hamiltonian.

Considering possible New Physics contribution as  $A_f^{NP}$ , the decay amplitude can be rendered as:

$$\mathcal{A}_f = \lambda_u^s T_f + \lambda_c^s P_f + A_f^{NP} \quad (1.40)$$

where  $T_f$  and  $P_f$  are tree-level and penguin-level amplitude. The coefficients are determined from CKM matrix elements:  $\lambda_i^q \equiv V_{ib}^* V_{iq}$ . Note that compared to the  $B^0 \rightarrow J/\psi K_S^0$ , the tree level amplitude  $T_f$  is suppressed and penguin amplitude  $P_f$  is dominated in  $b \rightarrow q\bar{q}s$ . It is worth noting that  $T_f$  contains both tree-level W exchange, QCD and electroweak penguin contributions. These carry the combination of CKM matrix elements  $\lambda_t^s = V_{ts} V_{tb}^* = -(1 + \epsilon_{uc}) \lambda_c^s$  where  $\epsilon_{uc} \equiv \lambda_u^s / \lambda_c^s = \mathcal{O}(\lambda^2)$ . In the Standard Model with neglected  $\epsilon$ ,  $b \rightarrow q\bar{q}s$  modes are pure penguin with the same weak phase as  $B^0 \rightarrow J/\psi K_S^0$  has. Thus, direct  $CP$  violation vanishes and time-dependent  $CP$  violation reflects  $\mathcal{S}$  in the same way as  $B^0 \rightarrow J/\psi K_S^0$  does.

Departures from this limit, non-neglected tree amplitude  $T_f$  (often called “tree pollution”), as well as possible NP effects, could give different results on  $\phi_1$ . Introducing the tree-penguin ratio  $r_f^T = T_f / P_f$  and NP-to-SM ratio  $r_f^{NP} = \mathcal{A}_f^{NP} / (\lambda_c^s P_f)$ , the following statements usually used[9]:

- Branching ratios are affected at  $\mathcal{O}(|\epsilon_{uc} r_f^T|, |r_f^{NP}|)$

- Direct CPV in the SM are of  $\mathcal{O}(\epsilon_{uc}\text{Im}(r_f^T))$
- $-n_f^{CP}\mathcal{S}_f = \sin(2\phi_1) + \Delta\mathcal{S}_f$ , where  $\Delta\mathcal{S}_f = 2\cos 2\phi_1 \sin \phi_3 |\epsilon_{uc}| \text{Re}(r_f^t) + \Delta\mathcal{S}_f^{NP}$

#### 1.4.4 $\phi_1$ from $B^0 \rightarrow K_S^0 K_S^0 K_S^0$

Since Belle reported the time-dependent  $CP$  analysis on various  $b \rightarrow q\bar{q}s$  which experimentally showed that the difference on  $\phi_1$  has a margin for NP effects[10], the expectation on the more precised measurement with larger data collection is popularly discussed. The decay channel  $B^0 \rightarrow K_S^0 K_S^0 K_S^0$  is one of the most promising modes for this purpose. The  $CP$  eigenstates of three  $K_S^0$  are positive definite ( $CP = +1$ ). Since there's no up-quark shown in the final states, the potential contribution of  $b \rightarrow u\bar{u}s$  re-scattered into  $b \rightarrow s\bar{s}s$  is almost of absence in terms of phenomenology. This makes  $B^0 \rightarrow K_S^0 K_S^0 K_S^0$  a cleaner channel than  $B^0 \rightarrow K^+ K^- K_S^0$  which has a different weak phase contribution [11]. Any NP effects that is expected in the  $B^0 \rightarrow \phi K_S^0$  should also affect  $B^0 \rightarrow K_S^0 K_S^0 K_S^0$  and the absence of NP effects will lead the same  $CP$  violation effects as  $J/\psi K_S^0$  [11]. Currently there's no specific calculation on the  $\Delta\mathcal{S}$  for three-body  $B^0 \rightarrow K_S^0 K_S^0 K_S^0$  using theoretical approaches. However, due to the same weak phase of this decay as  $\eta' K_S^0$  and  $\phi K_S^0$ , the theoretical prediction on  $\Delta\mathcal{S}$  is usually applied to  $B^0 \rightarrow K_S^0 K_S^0 K_S^0$ , also see [11]. Using QCDF(scan) approach [12], the expected range on  $\Delta\mathcal{S}$  is typically at level of  $\sim 0.05$ , which requires the expected precision improvement for both statistical and systematic uncertainty in future data. The result of  $\phi_1$  from  $B^0 \rightarrow J/\psi K_S^0$  using full Belle data is presented as  $\mathcal{S}_{J/\psi K_S^0} = +0.670 \pm 0.029(\text{stat}) \pm 0.013(\text{syst})$ . The expected center value for  $\mathcal{S}$  in  $B^0 \rightarrow K_S^0 K_S^0 K_S^0$  within the SM correction is at  $-0.68 \sim -0.72$  without any uncertainty ideally. In the meantime, the latest result of  $\phi_1$  from  $B^0 \rightarrow K_S^0 K_S^0 K_S^0$  using full Belle data [13] is presented as:  $\mathcal{S}_{3K_S^0} = -0.71 \pm 0.23(\text{stat}) \pm 0.05(\text{syst})$ , and the previous result from BaBar [14] is:  $\mathcal{S}_{3K_S^0} = -0.94^{+0.21}_{-0.24}(\text{stat}) \pm 0.06(\text{syst})$ . Both results have shown a slight room for NP effects while the margin is large mostly due to statistical uncertainties. In  $B^0 \rightarrow K_S^0 K_S^0 K_S^0$ , the experimental sensitivity of  $\Delta\mathcal{S}$  will be dominated by  $\mathcal{S}_{3K_S^0}$  because the total uncertainty from  $J/\psi K_S^0$  will be reduced to about 0.005[9] at  $50 \text{ ab}^{-1}$  Belle II data. The Figure 1-6 shows the scaled  $\Delta\mathcal{S}$

uncertainty regarding the luminosity in Belle II prospective[15], which only includes the statistical uncertainty of Table 1.1 . If the conservative estimation of systematic uncertainty from Belle is considered, the red arrow shows the approximate luminosity where the experimental sensitivity becomes comparable with theoretical prediction at  $\sim 0.05$ . If the future result is different from  $J/\psi K_S^0$  with a few times of the uncertainty at about 0.05, then it could be an evidence for NP effects. Of course, smaller the total uncertainty is, easier to identify the existence of NP effects.

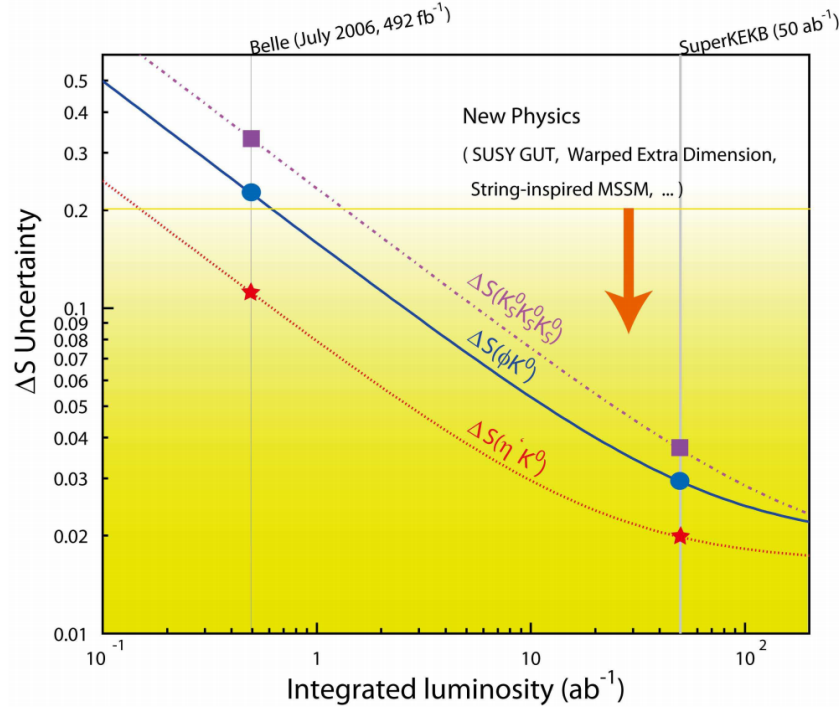


Figure 1-6: Expected sensitivity of  $\Delta\mathcal{S}$  regarding the integrated luminosity of Belle II prospective.[15]

Table 1.1:  $\Delta\mathcal{S}$  scaled uncertainty (statistical) with integral luminosity [15].

Observable	Belle ( $0.5 \text{ ab}^{-1}$ )	Belle II ( $5 \text{ ab}^{-1}$ )	Belle II ( $50 \text{ ab}^{-1}$ )
$\Delta\mathcal{S}_{\phi K_S^0}$	0.22	0.073	0.029
$\Delta\mathcal{S}_{\eta' K_S^0}$	0.11	0.038	0.020
$\Delta\mathcal{S}_{K_S^0 K_S^0 K_S^0}$	0.33	0.105	0.037



# Chapter 2

## Belle II Experiment

### 2.1 Belle II and SuperKEKB overview

The fundamental goals of Belle II experiment are to search for evidence of New Physics in the luminosity frontier, and to improve the precision of the measurement of the SM parameters, such as  $CP$  parameter.[9] It uses SuperKEKB accelerator as its particle collider at the center-of-mass energy in the region of  $\Upsilon(4S)$  resonances. The majority of the production will at the  $\psi(4S)$  resonance that is slightly above the mass of two  $B$  mesons. The electron and positron beams are designed at 7 GeV and 4 GeV, respectively, with boost factor of 0.28. This creates an environment for measuring time-dependent  $CP$  violation by displacing the decay vertices of a  $B$  meson pair in a measurable distance along the boosted direction. SuperKEKB has a targeted luminosity of  $8 \times 10^{35} \text{ cm}^{-2}\text{s}^{-1}$ , 40 times higher than its predecessor, KEKB at peak luminosity. The expected operation period is from 2019 to the end of 2030. These facilities are located in KEK, Tsukuba City, around 70 km in the north of Tokyo, Japan. Some key parameters of SuperKEKB are listed in Table 2.1. The overview of SuperKEKB and Belle II are shown in Figure 2-1.

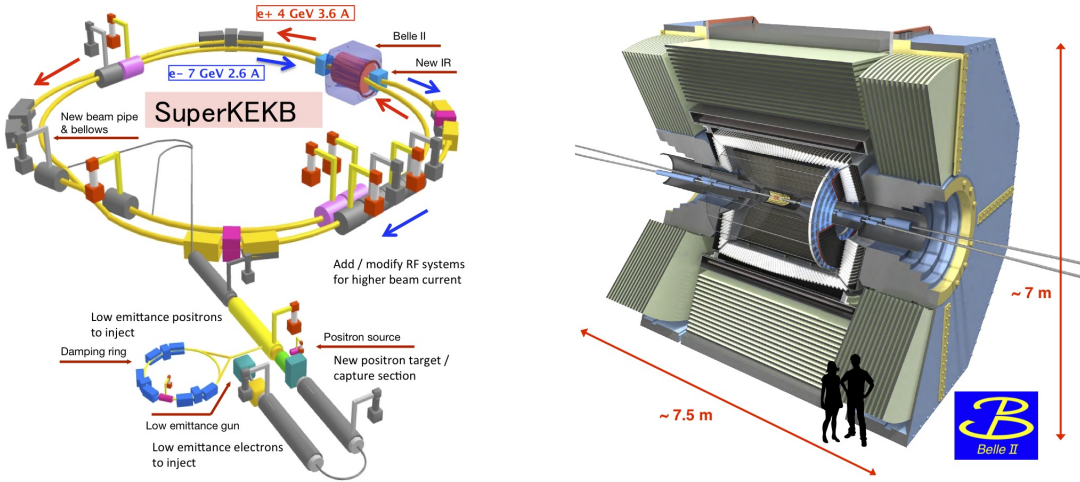


Figure 2-1: Overview of SuperKEKB and Belle II detector [15].

Table 2.1: SuperKEKB parameters for low energy (LER) and high energy (HER) rings.[9]

Parameters	LER( $e^+$ )	HER( $e^-$ )	Unit
Energy	4.0	7.0	GeV
Half crossing angle	41.5		mrad
Horizontal emittance	3.2	4.6	nm
Emittance ratio	0.27	0.25	%
Beta functions at IP (x / y)	32/0.27	25/0.30	mm
Beam currents	3.6	2.6	A
Beam-beam parameter	0.0881	0.0807	
Luminosity	$8 \times 10^{35}$		$\text{cm}^{-2}\text{s}^{-1}$
Perimeter of ring	3		km

Belle II detector has a similar size as Belle so that it fits in the previous shell, but all sub-detectors and components have been either newly built or considerably upgraded. The advantage of SuperKEKB requires that Belle II has to be able to

stably operate at 40 times higher events rates as well as 10 to 20 times higher beam background compared to Belle at its peak luminosity. This means the mitigation of the effects caused by such high beam background is essential to the success of Belle II. Higher background level leads to high occupancy and radiation damage to the detectors at close range, along with more fake hits in the vertex detectors, pile-up noises in electromagnetic calorimeter and neutron-induced hits in muon detector. Data-acquisition system (DAQ) and trigger are also upgraded not only to adapt to higher luminosity but also for low-multiplicity event sensitivity to support a broader search especially in dark sector. Belle II detector top view is shown in Figure 2-2, and expected performances are summarized as follows:

- vertex resolution of  $B$  mesons of  $\sim 50 \mu\text{m}$ ,
- excellent reconstruction efficiency for charged tracks down to several 100 MeV and fairly good efficiency for charged tracks down to  $\sim 50 \text{ MeV}$ ,
- excellent momentum resolution up to  $8 \text{ GeV}/c$ ,
- highly efficient particle identification to separate  $\pi^\pm$ ,  $\mu^\pm$ ,  $e^\pm$ ,  $K^\pm$  and  $p$  at full energy range of experiment,
- full cover of experimental acceptance solid angle,
- ultra fast and highly efficiency DAQ and trigger system to cope with large data quantities and fast triggering frequency.

The success of Belle II detector depends on the complex of sub-detectors which each of them is design for specific purposes. The critical components and features are explained in the following sections.

## 2.2 Vertex detector (VXD)

There are two components in VXD, the silicon based pixel detector (PXD) and silicon based vertex detector (SVD), where total 6 layers are placed in the inner-most region from interaction point (IP). As for PXD, two layers are placed at radii of  $r = 14 \text{ mm}$  and  $r = 22 \text{ mm}$  with DEPFET type pixel sensors, respectively. The PXD layers are the closest to Interaction point (IP) so the vertex resolution can be much improved.

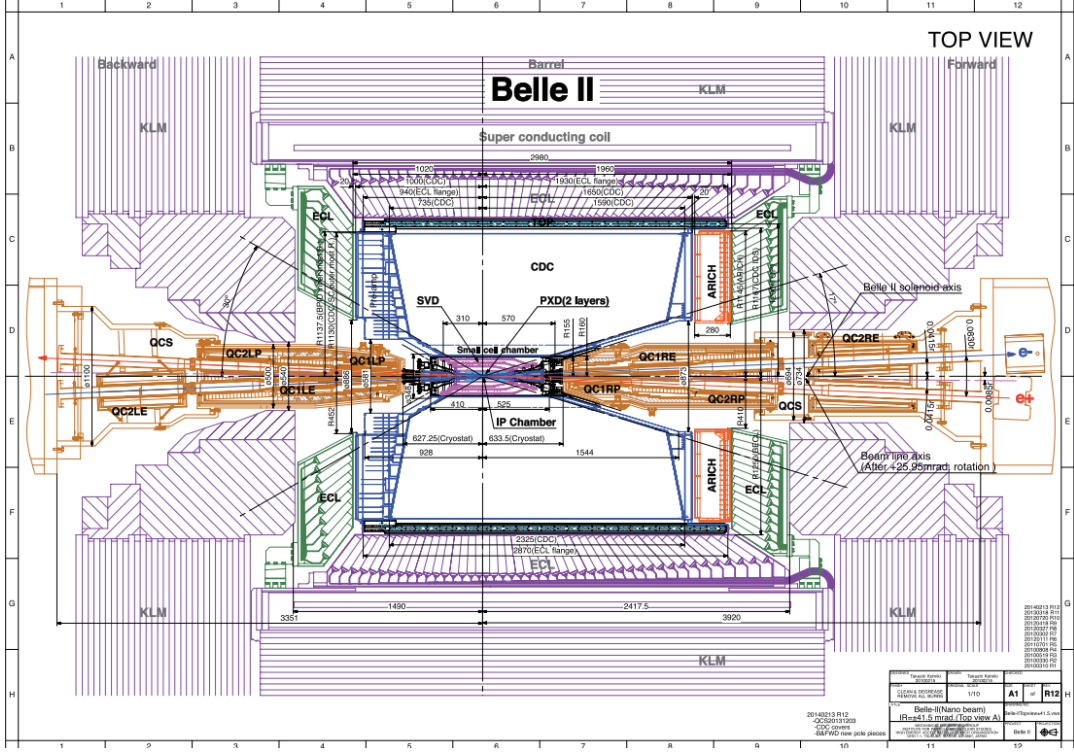


Figure 2-2: Belle II detector top view [9].

However, much higher events rate comes with much higher background level on PXD sensors. The overloaded occupancy leads to severe dead time and incredibly large data size from PXD if no data reduction scheme is implemented. In order to trim down data from PXD, a fast online tracking system is built up. In the data taking workflow, the data from PXD will be first readout to a system called “ONSEN” which can store large size temporary data up to 5 seconds. In this timing window, a fast online tracking system will perform a track fitting extrapolate the fitted tracks backward to PXD plane so the region of interest (ROI) on PXD sensors can be defined. The data outside of the ROI are not read out from ONSEN system to external tapes where offline data is written. This scheme helps reduce large fraction of data especially in the very high luminosity.

For the SVD detector, the sensors are made of “double-sided silicon strip sensors” (DSSD) with 4 layers at 39 mm, 80 mm, 104 mm, and 135 mm. The geometry of VXD from the is shown in Figure 2-3. The outmost layer of SVD is also larger than Belle SVD1/2. This could be helpful for ensure the reconstruction efficiency for the decay

like  $K_S^0 \rightarrow \pi^+ \pi^-$ . However, the current hit filter of SVD doesn't allow the "single-hit seeding" in the track reconstruction, which means any track candidate should have at least two SVD hits. This is due to the concern of the large fraction of single-hit background. For the  $K_S^0$  with long flight length, if the daughter  $\pi^\pm$  only hits one layer of SVD, the reconstruction efficiency is dropped.

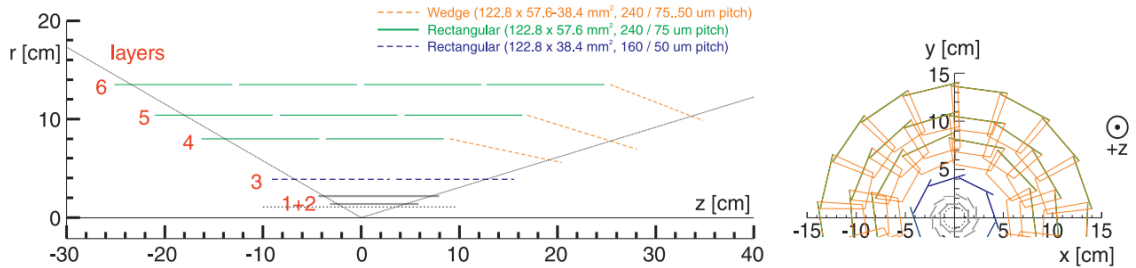


Figure 2-3: A schematic view of PXD (2 layers in gray) and SVD (4 layers in green and orange) [15].

## 2.3 Central drift chamber (CDC)

The central tracking system is the core component of spectrometer in Belle II, which consists of a fairly big drift chamber made of many small drift cells filled with He-C<sub>2</sub>H<sub>6</sub> gas. The out radius of CDC has been extended to 1130 mm from 880 mm of Belle thanks to the much thinner layers in barrel region. The whole CDC contains 14336 sense wires in 56 layers, placed in the axial direction or the stereo direction. Such design can utilize the information from axial and stereo wires to construct a full 3 dimensional hits which forms helix tracks in CDC volume. Thus, CDC is one of the key components for measuring the helix parameters for tracking system. The example of CDC tracking of a cosmic ray event is shown in Figure 2-4

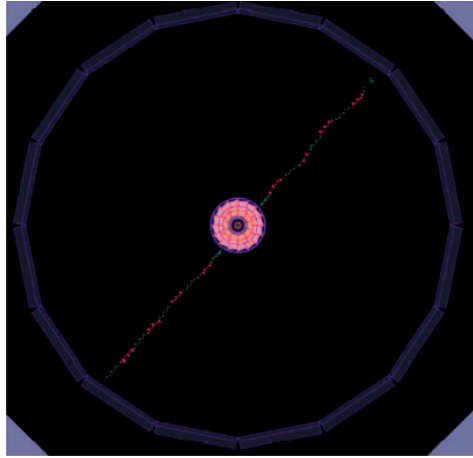


Figure 2-4: CDC tested with a cosmic ray event [9]

## 2.4 TOP and ARICH detectors

The particle identification system of Belle II mainly consists of two parts, time-of-propagation counter (TOP) and aerogel based Cherenkov radiation imaging ring (ARICH). TOP is the specialized detector that can reconstruct Cherenkov radiation's time of arrival and generated position by a photon detector placed at the end of a 2.6 cm quartz bar. Due to the ultra-fast flying time of photon, the TOP detectors has to achieve timing resolution at around 100 ps. A 16 channels micro-channel plate photon-multiplier (MCP-PMT) with custom-made waveform electronics of readout is used. The resolution of starting time is achieved about 50 ps. [15].

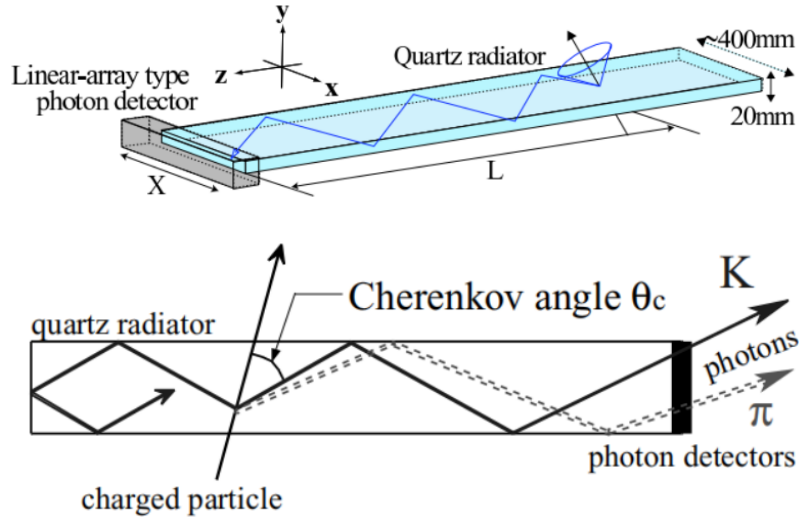


Figure 2-5: Schematic view of TOP counter (up) and its imaging process of  $K^\pm$  and  $\pi^\pm$  (down)[15].

As for ARICH, it uses areogal as the sensitive material to approximately image the Cherenkov ring by a special focusing structure to identify charged particles. ARICH should be able to separate charged particles in a momentum range from 0.5 GeV to 4 GeV. ARICH requires single-photon-sensitive high-granularity sensor to reconstruct the Cherenkov angle with small photon yield. Hamamatsu Corporation, Japan, has developed a hybrid avalanche photon detector (HAPD) to meet the requirements. Each sensor is  $73 \times 73 \text{ mm}^2$  embedded with 144 channels to accelerate emitted electrons in a 8 kV field. Avalanche photo-diodes (APD) are used for the detection of electrons at the end of electron acceleration, see Figure 2-6. The ARICH detector outlook and the ring image of cosmic  $\mu$  on the HAPD sensors are shown in Figure 2-7.

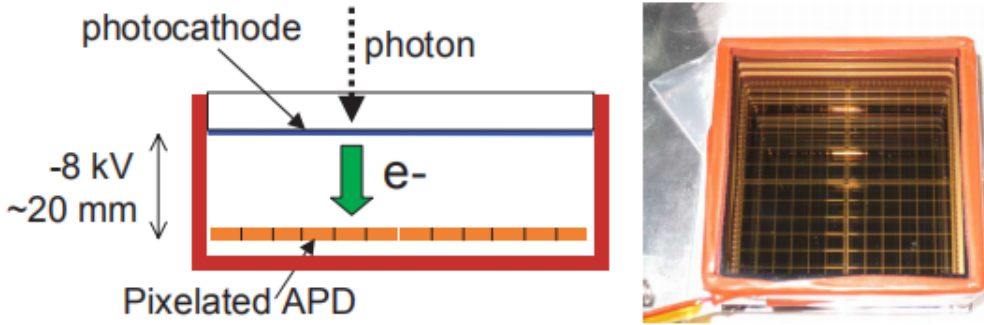


Figure 2-6: Photon-electrons acceleration (left) and pixelated APD (right) at the end[15].

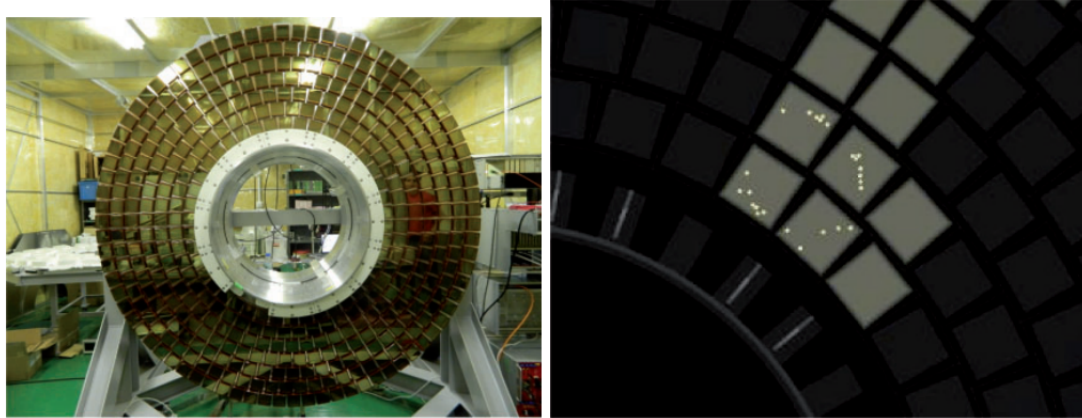


Figure 2-7: ARICH detector (left) and the ring image of cosmic  $\mu$  on the HAPD sensors[9]

## 2.5 Electromagnetic calorimeter (ECL)

The electromagnetic calorimeter of Belle II is mainly responsible for the detection of  $\gamma$  radiation and electrons. The thallium doped caesium iodide CsI(Tl) crystals are assembled tightly in all three different regions, backward/forward end-caps and barrel region. Compared to the previous ECL in Belle, the pre-amplifiers and the structures remain unchanged, while the readout electronics have been upgraded. The estimated background level in Belle II ECL will cause the much longer decay time in the scintillation of CsI(Tl). This will lead to the pile-up effect of readout noise. To compensate this effect, wave-form sampling electronics are embedded with the photon

detectors (PMT). Especially in the forward direction of the electron beamline, where the level of beam background is much higher, the effect of pile-up noise becomes even worse and the performance of ECL will be of trouble if no special measure taken. In this situation, the pure CsI crystal is chosen as the material of detector to achieve a fast wave-shaping time and higher radiation tolerance compared to the dosed CsI(Tl).

## 2.6 $K_L^0$ muon detector (KLM)

KLM system of Belle II consists of a sandwich stacked iron plates and detectors at outside of the superconducting solenoid. The iron plates serve as the interaction materials with  $> 3.9$  times the interacting length of material compared to the ECL, allowing  $K_L^0$  particles to shower through. The Belle KLM material uses the glass-electrode resistivity plate chambers (RPC) which is not suitable for Belle II due to high background level. Neutrons dose is significantly larger due to the much more electromagnetic radiation reaction on detector materials. The long dead time of RPC under such dose rate will reduce the efficiency of KLM. Besides, the mis-identification possibility would be raised so PID contribution from this part of detector will be meaningless. To mitigate this problem, the RPCs are replaced by the layers of scintillator strips with wavelength-shifting fibers, read out by silicon photomultipliers (called “SiPMs”, Geiger mode operated APDs) as light sensors, which is proven to be able to reliably operate by setting up the discrimination threshold [9].

## 2.7 Trigger and DAQ system

The interesting topics in Belle II physics analysis highly depend on the trigger system. With the upgraded capabilities to study a wide range of physics analysis at a very high luminosity in Belle II, the trigger system is expected to properly operate at a high event rate. The Belle II trigger system is composed of two levels: a hardware-based, low-level trigger called “L1” trigger, and a software-based high-level trigger (HLT). The L1 trigger has a latency of  $\sim 5\mu\text{s}$  and the maximum trigger output rate

is 30 kHz, which is limited by the read-in rate of data acquisition system (DAQ). Considered the high event rate and background level from future Belle II luminosity, a series of upgrades have been implemented for L1 trigger. The key improvements of L1 come from the firmware-based reconstruction algorithm and trigger logic. It's worth noting that a specialized set of hardware trigger lines for dark sector researches are implemented, which improves the trigger efficiency for single energetic photon in the final states.

HLT, as the second level of Belle II trigger systema, plays an important role in DAQ. As discussed in the section of PXD, the data size in PXD is huge at high luminosity and the ROI selection must be applied to reduce the online event rate. The event rate reduction relies on the tracking extrapolation on PXD plane, which is the key function of HLT. HLT can suppress the event rate down to 15 kHz using the information from the CDC tracking and ECL reconstruction. The event rate is further reduced to 10kHz by using full reconstruction information.

Since the primary goal of Belle II is focusing on  $B$  physics studies, it is natural that the trigger system should be able to operate over all of the interesting  $B$  physics conditions, with normally 3 or more CDC tracks and large energy deposition in ECL. By offline reconstructing the simulated events and studying the efficiency, close to 100%  $B$  decays are recorded by Belle II trigger system. However, the extensive capabilities of studying a large range of physics not only in  $b$  sector brings a challenge to Belle II trigger and DAQ system. Belle II is expected to show the excellence at performing measurements on other important topics such as  $\tau$  physics and dark sector researches. These topics usually suffer from the high beam background. Thus, the control of beam background becomes essential. With SuperKEKB, beam background is about 10 to 20 times higher than Belle at the peak instantaneous luminosity. This rises a challenge for Belle II trigger and DAQ system. The main sources of beam background are beam-gas scattering, synchrotron radiation, the radioactive Bhabha scattering, the two-photon process, beam-beam effects, and Touschek effect. Their impacts depend on many factors such as beam current, luminosity and vacuum conditions, etc. One of the featured topology of these beam background events is the

combination of two charged tracks in CDC and one or two clusters in ECL. Beam background events are often assembled with low-multiplicity events from primary collision, and the latter is the main focus of dark sector studies. It's quite important to distinguish these low-multiplicity events from various beam backgrounds. The simulated beam background rate and their sources are listed in Table 2.2.

Table 2.2: Simulated beam background rate (12th BG campaign)[9]

Type	Source	Rate (MHz)
Radiative Bhabha	HER	1320
Radiative Bhabha	LER	1294
Radiative Bhabha(wide angle)	HER	40
Radiative Bhabha (wide angle)	LER	85
Touschek scattering	HER	31
Touschek scattering	LER	83
Beam–gas interactions	HER	1
Beam–gas interactions	LER	156
Two-photon QED	-	206

The improvements on both L1 and HLT triggers, along with DAQ upgrade has shown a good potential in dark sector researches[16][17], thanks to the improved discriminating ability of low-multiplicity events against beam background. In future, several modifications on the current trigger system is under consideration, such as the partially pre-scaled trigger lines, which is expected to be optimized for dark sector studies[9].

## 2.8 Analysis Software

The data acquired by the Belle II experiment or simulation can be processed by Belle II Analysis Software Framework, called BASF2. It has a good capability to handle the tasks of sophisticated algorithms for simulation, reconstruction, visualization, and analysis. The official BASF2 is developed in different release versions, light-versions and featured-versions. In this thesis, release-05-01-01 version is used.

### 2.8.1 BASF2 Core Structure

The core structure of BASF2 contains three major parts: the analysis codes specifically required by the needs of Belle II data (called Belle II codes), the external libraries that are the third-party software which Belle II utilize, and the tools for configuring and installing the BASF2 software.

The Belle II codes consists of many packages. They are categorized based on the different levels of Belle II detector components, like the packages of base-level system control called “framework”, the package for track reconstruction called “tracking”, and the one for post-reconstruction data analysis called “analysis”. Users can work either with compiled binary version of BASF2 installed centrally on working servers, or build from the source based on their own need.

As for the externals, it contains the many packages or libraries that provide functionalities BASF2 needs during the execution or installation. For example, some basic packages, like gcc compiler, cmake, tar, wget, Python and git are included. In particular, due to the dependence of the analysis tools that may be frequently used by Python, around 100 additional Python packages are installed as the externals, such as “Numpy” and “matplotlib” packages that provide functions for statistical calculations and plotting. The complexity of building all of these external software could be tough for users so that the compiled versions that cover the common platforms are available from BASF2 official repository.

Tools are collections of shell or Python scripts for setting up BASF2 and externals environment. It can easily handle the need of setting up an environment of specific BASF2 version and the externals tied to that version. It also provides a function to setting up the environment of developing BASF2, where developers can get one developing copy of BASF2 and write the additional codes as the modification, so the compatibility of BASF2 could be easily maintained by building a release version from the developing branches. In this thesis, two new packages are developed and built with release-05-01-01 version BASF2. This developing version of BASF2 contains all functions that release-05-01-01 has. The details will be discussed later.

## 2.8.2 Event Processing Workflow

The data from Belle II detector or from the simulation, are organized into a set of runs that are defined by either experimental conditions or simulation conditions. For instance, the simulation data from a certain detectors' condition are packed together, marked with the conditions' database index that is used during the simulation. Such data sample then is divided into different runs based on estimated luminosity from experiment, which can contain the different number of events in each run. This scheme is used for categorizing experimental data as well, so that users can easily know which experiment conditions are used. In a run, every event is recorded as an independent measurement of an electron-positron collision, a cosmic ray injection or background event. Such experiment-run-event structure is the basic data structure that BASF2 handles. Thus, when BASF2 processes a data set, the functions are called for every event based on different configurations that are corresponding to the different experiment conditions. For example, in a data set where events are recorded with the different magnetic fields, BASF2 can automatically change the configurations of the magnetic fields event-by-event to provide a better track measurement. Based on this idea, all BASF2 functions (called “modules”) are developed based on a python module class which contains following embedded functions to be called at event-based level:

- initialize: called at the start of processing a event to properly set up constants needed for this run.
- beginRun: called at the start of calling this module, including setting up database conditions used in this run (run-dependent configurations) or event (event-based configurations).
- event: called for each event. This is the actual processing step, such as perform tracking or combining all daughters to find a mother particle.
- endRun: called at the end of a run, usually to register all processed information to the storage, such as physics variables from all reconstructed particles.
- terminate: called at the end of the processing of all events, release the buffered

space and memory.

BASF2 executes a series of modules loaded dynamically to process the data set according to above sequence. The selection, configuration and executed order of the modules are defined by a file called “steering file” written in Python. The modules parameters are attributes which can be set during the runtime using the steering file. For example, the “Path” object declared in a steering file stores the sequence of modules that will be executed, to which allow other modules such as “mdstInput” or “reconstructDecay” to be added. Users can use “boolean” type variable set in “event” function to create a conditional branch of a “Path” in case that one event needs to be processed with different modules at the same time. For instance, in the decay reconstruction package, if a decay chain is not fulfilled by missing one particle in the “event” functions, other back-up decay chains can be checked to see if a successful reconstruction is possible.

The object that interacts with BASF2 I/O is called “DataStore”. This implementation doesn’t depend on the event data model. The only mandatory component is called “EventMetaData” which presents the experiment, run and event number of a event. “Unpacker” module converts the raw digits into digits-based object in BASF2. In simulation, digitization is done by module called “digitizer”. The digits-based objects are further processed to form hits or clusters depending on detector types. Higher level functions such as tracking and decay reconstructions are implemented based on these basic information by their packages. Eventually, BASF2 writes out the information based on users’ needs, like kinematics variables, to ROOT[18] format files, or simply prints out processing statistics to the standard output.

In practice, BASF2 starts running when it checks there is at least one module specifying the number of events to be processed in a “path” from the “steering file”, then it reads in the information from “DataStore” in the input ROOT file, execute all the requested modules in the “steering file” and return the time and number of events as information printed in standard output. In Figure 2-8, an example of “steering file” is shown, with a “path” called “main” created and a module called “EventInfoSetter” added. This steering file will process 100 event, set their experimental numbers, run

numbers and event numbers.

```
#!/usr/bin/env python3
# -*- coding: utf-8 -*-

# Generate 100 events with event numbers 0 to 99
# that contain only the event meta data.

import basf2
main = basf2.create_path()
main.add_module('EventInfoSetter', evtNumList=[100])
basf2.process(main)
```

Figure 2-8: An minimal example of BASF2 steering file, setting up a basic processing of 100 events in “path” called “main”.

### 2.8.3 mDST structure

The output from BASF2 processing can contain several detector-specific objects, which are restored as mini data summary table (mDST) type ROOT file. For instance, in a mDST file, the object called “RecoTracks” will be created if track pattern recognition is called and “Track” object will be created if the track fit is performed. For a mDST level analysis, the goal is usually aimed to find particles from physics processes and reconstruct decay information. A output mDST ROOT file could typically contain the following objects:

- Track: object presenting any charged particle trajectory. It’s linked to multiple track fit results using different nominal mass hypotheses as well as their track fit quality to help select good tracks.
- TrackFitResult: the fitting result of tracks with different mass hypotheses. It consists of five helix parameters, their covariance matrix and p-value from the fit. It also stores the information of hit pattern on vertex detector and CDC.
- V0: object for the relative long-lived neutral particles that fly out of interaction region but mostly decay or interact inside detector region. In Belle II, these are mostly  $K_S^0$ ,  $\Lambda$  and photon converted to electron pairs. V0 also stores their relation to

the charged daughter tracks and track fit results for further selections.

- PIDLikelihood: it presents for the possibility of a charged track to be an electron, muon, charged kaon and pion, proton and deuteron provided by particle identification system.
- ECLCluster: reconstructed cluster in ECL detector. It consists of energy deposition and hit positions as well as other hit shape related variables. If a cluster is matched with an extrapolated track, a relation between them will also be created.
- Reconstructed cluster KLM detector. It consists of momentum and position measurement. If a cluster is matched with an extrapolated track, a relation between them will also be created.
- KLId:  $K_L^0$  candidates with the particle identification as related to KLM and ECL clusters.
- TRGSummary: L1 trigger information.
- SoftwareTriggerResult: HLT information mapped by trigger names to trigger results.
- MCParticle: simulated particles containing momentum, production and decay vertex, relations to mother and daughter particles, and traversed detector components. Particle-detectors relations are created if simulated particles are correctly reconstructed as tracks or clusters.

The size of mDST level data is very important to BASF2 offline processing performance. Thus, mDST level data is restricted from contain non-physical analysis related information such as raw digits or calibration constants. For detailed detector or reconstruction algorithm performance studies, and also for calibration tasks, a dedicated format higher than mDST, called cDST (calibration data summary table), is used.

#### 2.8.4 Conditional Database

In addition to the physics data, analysis relies on various conditional data that are different calibration of detector, weight files for multi-variate analysis usage like PID and so on. This data is stored in a central database server called central Conditional

Database (CDB).

Conditions are made of payloads and each payload has its own “Intervals of Validity” (IoV). It defines in which runs the payload is valid. A set of payloads and IoVs are called a global tag (GT). Considered the GT that is required by the different analysis purposes may change even though the experiment condition is still same, GT is subjected to be updated once new calibrations of detectors or weight files for MVA tools are available. On the users’ side, except for just using central database, a local database back-end that takes GT information such as calibration data while uses a local database, such as a customized PID weight file, is also possible. It automatically download the needed database files that are required for a BASF2 execution and stores them in a local folder. This means even if the computer is offline or the CDB is not reachable, one can still run BASF2 as long as the local folder was there.

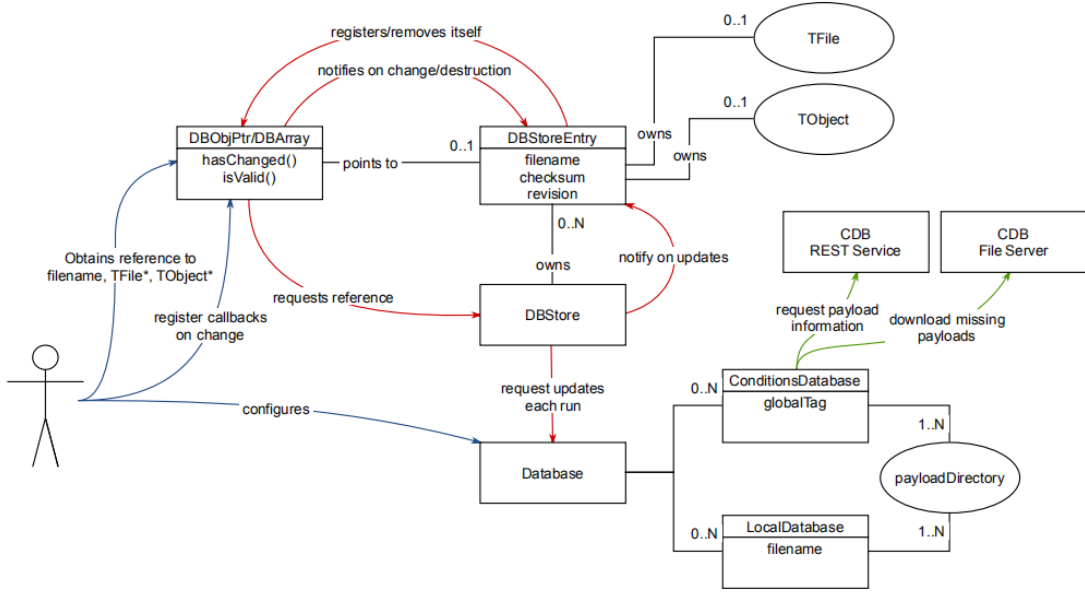


Figure 2-9: Relations of all entities in CDB[19], showing the management logic from users’ end to each CDB files and services.

The management of CBD with the extension of local database gives a good convenience for users to perform their own analysis and share the results with collaborators. Users’ access to conditions objects in the CDB is provided by two interface classes, one

for single objects called “DBObjPtr” and one for arrays of objects called “DBArray”. To facilitate easy creation of new conditions data – for example, during calibration – we provide two payload creation classes, “DBImportObj” and “DBImportArray”. They have an interface very similar to DBObjPtr and DBArray[19]. Users instantiate one of the creation classes, add objects to them and commit them to the configured database with a user-supplied IoV. This includes the support for run dependency as well. The capability to use a local file-based database allows for easy preparation and validation of new payloads before they are uploaded to the CDB. The scheme of this entities and how users interact with CDB object is demonstrated in Figure 2-9. For example, user can perform their analysis and first locally generate weight files or calibration data based on different run conditions and reconstruction criteria, which are stated by their names of the IoVs. Once the results are good to share, they can create a GT in CDB of which they have the full ownership, add all database files into the GT and open it to Belle II collaboration. Anyone who would like to re-calibrate data or use their weight files for PID and so on, can simply use the built-in function “basf2.useCentralDB()” in BASF2 to directly access the corresponding data. However, only the creator of the CDB objects has the right to add, recall, replace and remove the GT, which guarantees the stability of the CDB and responsibilities for each user.

## 2.9 Belle II simulation

This section briefly describes simulation (MC) used in the studies presented in this thesis. As for the focus of this analysis is in  $b$  sector which is mainly from  $\Upsilon(4S)$  decay, the discussed simulation is based on the collisions with center-of-mass (CMS) energy at  $\sqrt{s} = 10.58$  GeV.

In the previous section, it’s shown that many packages and functionalities have been integrated with BASF2, including the core components of Belle II simulation in  $B$  decay: “evtgen” as event generator and “GEANT4” as the simulator of detectors. Along with the active development of BASF2 in the early stage of Belle II, the versions

of software that is used for simulation and reconstruction are often different. For the simulation used in this analysis, BASF2 version release-04-02-08 was used. For the event reconstruction, the used BASF2 version is release-05-01-01. This is not a problem thanks to the CDB management, allowing modified software to use the same constants such as magnetic field distribution for the consistence between simulation and reconstruction.

All simulations start with at least one event generator that configures the physics processes. In Belle II, the configuration of “evtgen” requires a decay file called “xxx.dec” that describes the decay chain from a certain mother particle, branching fraction for all processes and decay-related information such as flavor mixing or  $CP$  violation information. For different type of decays, the different decay files are prepared. MC sample is centrally produced using Belle II GRID computing service based on these files periodically, so that the latest improvements of software can be applied. Each round of MC sample is called a campaign named with their index, such as “MC13”, which is the 13th (latest in 2020 Winter) Belle II official MC production (in the following content of this thesis, MC13 will be used referring this group of MC samples).

For the analysis in this thesis, there are two MC samples, one is called “signal MC” and the other is called “generic MC”. Both MC samples use “evtgen” as event generator. Signal MC, as its name suggests, is the MC sample that describes the whole decay chain of  $B^0 \rightarrow K_S^0 K_S^0 K_S^0$ . The mother particle of the decay chain is  $\Upsilon(4S)$ , then it decays into a pair of  $B^0 - \bar{B}^0$  at branching fraction of 100%, with the model “EvtVSSMix”[20] describing the decay model. Then, one of the  $B$  meson is set to decay into three  $K_S^0$  based on phase-space model (“PHSP”) at 100% branching fraction. To be noted, the phase-space model doesn’t provide any time-dependent  $CP$  violation. The default configuration of “evtgen” can not handle multi-bodies charmless  $B$  decay with TDCPV. A modified decay model profile is under-development and not fully validated yet. Thus, MC sample of  $B^0 \rightarrow K_S^0 K_S^0 K_S^0$  yields zero  $CP$  parameters by default. As for the other  $B$  meson, it decays into all possible final states that are described by Belle II generic decay file.

Table 2.3: Production cross section for different hadronic flavors from collision at  $\sqrt{s} = 10.58$  GeV used in Belle II generic MC.[9]

Processes	$\Upsilon(4S)$	$u\bar{u}(\gamma)$	$d\bar{d}(\gamma)$	$s\bar{s}(\gamma)$	$c\bar{c}(\gamma)$
Cross section [nb]	$1.110 \pm 0.008$	1.61	0.40	0.38	1.30

As for generic MC, all hadronic processes in a  $\sqrt{s} = 10.58$  GeV collision are simulated. The total production cross section receives contributions from not only  $\Upsilon(4S)$  ( $b$ -flavor decay dominated), but also  $u, d, s, c$ . Their relative branching fractions are taken from cross sections at  $\sqrt{s} = 10.58$  GeV as shown in Table 2.3. Generic MC sample contains 6 types of MC samples due to this production arrangement, where  $\Upsilon(4S)$  produces “mixed” (neutral) and “charged”  $B$  meson pairs and the rest are “uubar”, “ddbar”, “ccbar” and “ssbar”, respectively. In this thesis, the latter 4 types of MC samples are combined and called “qqbar” for simplicity. In the mixed MC sample, the branching fraction of  $B^0 \rightarrow K_S^0 K_S^0 K_S^0$  is set at  $6 \times 10^{-6}$  and the branching fraction of  $K_S^0 \rightarrow \pi^+ \pi^-$  is set at 0.692. Both values are taken from PDG[21]. Same as signal MC,  $CP$  violation is set to zero for signal events in generic MC since they use the same model at generator level.

In addition to the simulation of physics processes, MC campaigns are produced with at least two beam background conditions, called “BG0” and “BG1”. The former stands for no beam background and the latter is produced with one overlay of beam background. The components of them have been discussed briefly in section 2.7. The mixing of simulated beam background to simulated physics events is done by adding simulated hits on each sub-detector output. Possible pile-up of hits is therefore inherently included. The average number of background events of a given type to be added to a single simulated event is determined from the rate  $R$  of a particular background sample and the time window  $\Delta t$  in which the background is mixed in Equation 2.1:

$$\bar{N} = sR\Delta t \quad (2.1)$$

where  $s$  is an optional scaling factor. The injected background events are based

on a Poisson distribution with mean  $\bar{N}$ . Within the timing window, the background events are shifted randomly to simulate contributions from different bunches. To use real experiment background events (data-based beam background), the random triggered events are measured and added to simulated BG0 MC sample for a more precised background configuration. This method can give a more realistic description of actual beam background but with a possibility to introduce bias due to the pile-up effect of multiple background events in a short timing window. In the early stage of Belle II, the level of background is not high and the background pile-up effect is small. Therefore, for MC13, BG1 sample is produced with data-based beam background.

In total, there are 2 million events generated in signal MC. Half of the signal MC (1 million) is produced without beam background for cross-checking the reconstruction performance. For generic MC,  $1 \text{ ab}^{-1}$  sample including mixed, charged and  $q\bar{q}$  events are produced with beam background at  $\sqrt{s} = 10.58 \text{ GeV}$ .

## 2.10 Belle II data taking

Belle II Phase I operation started in 2016 which was focused on the commissioning and test of SuperKEKB. Later in 2018, the commissioning of Belle II detector and SuperKEKB was finished. From 2019 April, Phase III operation that marked the beginning of official physics runs has started. By the end of 2020, Belle II has been operating in Phase III for 4 total run seasons. The integrated luminosity collected during this period of time is about  $84.73 \text{ fb}^{-1}$ , see Figure 2-10. The official processing of recorded data is performed along with the data taking. For the analysis reported in this thesis, the experimental data collection from experiment number 7, 8, 10 and 12 is used. Only the data collected at  $\Upsilon(4S)$  energy is included. Correspondingly, the integrated luminosity that is used for this thesis is about  $62.8 \text{ fb}^{-1}$ .

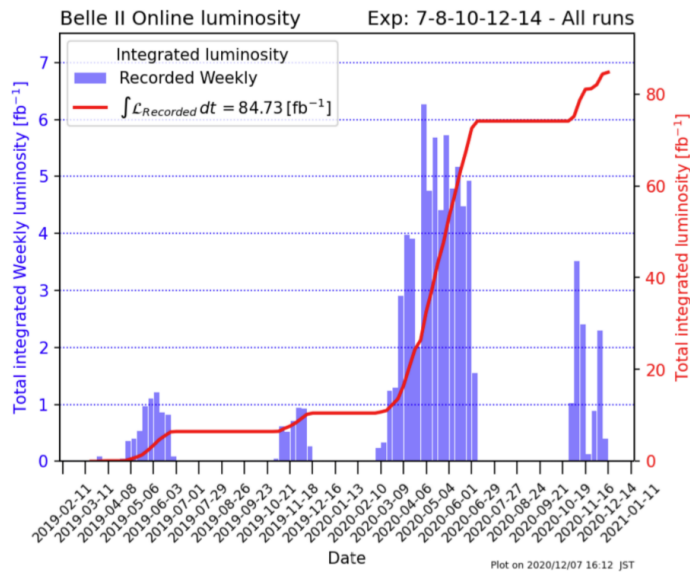


Figure 2-10: Belle II online luminosity from 2019 April to the end of 2020[22].

# Chapter 3

## $K_S^0$ Reconstruction Study

The final states of  $B^0 \rightarrow K_S^0 K_S^0 K_S^0$  only depends on the decay of  $K_S^0$ . The main decay channels of  $K_S^0$  is to either  $\pi^+ \pi^-$  at branching fraction of about 0.692, or to  $\pi^0 \pi^0$  at branching fraction of 0.307, which are referenced from PDG[21]. The characteristics of these two decays are much different in terms of the response from Belle II detector. The charged decay that yields  $\pi^+ \pi^-$  leaves two tracks originating from VXD or CDC volumes with opposite charges. On the other hand, the  $\pi^0$  main decay channel is  $\pi^0 \rightarrow \gamma\gamma$ . This creates a bunch of clusters on ECL. The reconstruction of the decay channel is performed through  $\pi^+ \pi^-$ . There are mainly two reasons for not selecting  $\pi^0$  as final states. First,  $\pi^0 \rightarrow \gamma\gamma$  can yield a large fraction of fake  $K_S^0$ . The reconstruction of two ECL clusters provides no constrain on  $K_S^0$  vertex so it's almost impossible to suppress the combinatorial background using vertexing quality in this case. The only reliable selection will be the mass of  $K_S^0$  which is typically distributed around its nominal mass with a few hundred of keV. The  $\gamma$  however, could be originating from many other resources, such as beam background and charged track radiation. Using mass window of  $K_S^0$  could not effectively reject the noticeable fraction of fake  $K_S^0$ . Second, with  $K_S^0$  reconstructed from neutral pions , the events of  $B^0$  that consist of one or more such  $K_S^0$  have poorly reconstructed vertices. To be noted that even with  $B^0 \rightarrow K_S^0 K_S^0 K_S^0$  which only uses  $K_S^0$  from charged pions as the final states, there is no direct charged tracks from the interaction region, which leads to the worse resolution of vertex position compared to the channel like  $B^0 \rightarrow J/\psi K_S^0$ , which has two direct

charged tracks of  $e^+e^-$  or  $\mu^+\mu^-$  thanks to the very short flight distance of  $J/\psi$ . If one (or more) of  $K_S^0$  has the poor vertexing quality from its decay products, it can further reduce the precision of vertex positions of  $B^0$ . This leads to a large uncertainties in defining the decay time of signal  $B^0$  and the decay time difference. The latter is the key observable in TDCPV measurement. Based on above, only  $K_S^0$  reconstructed using charged pions are considered in this analysis.

### 3.1 Cut-based $K_S^0$ Reconstruction

The  $K_S^0$  has average life time at  $(8.954 \pm 0.004) \times 10^{-11}$  s. Therefore, the flight length of  $K_S^0$  is comparable with the scale of detector size. In the typical Belle II energy scale, the flight length of  $K_S^0$  is in a range from a few micrometer away from  $B$  vertex, to more than 14 cm that is outside of the last layer of SVD ladder, see Figure ??.

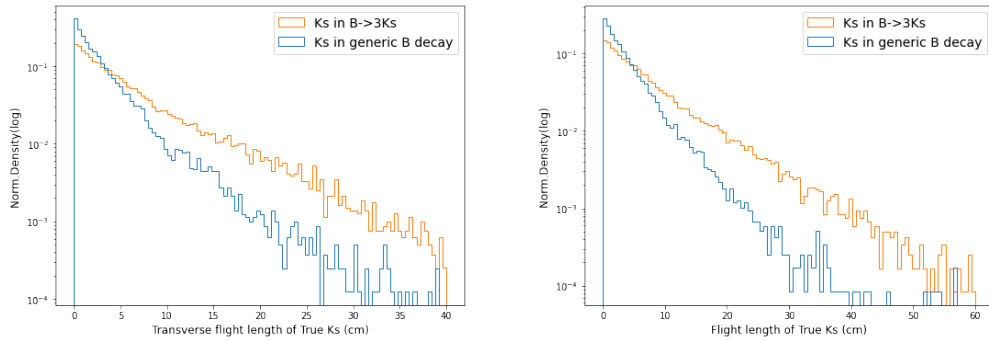


Figure 3-1: The left is transverse flight length and the right is the total flight length from true  $K_S^0$ . The blue is from generic MC and the orange is from signal MC. It's clear that the average  $K_S^0$  flight length in signal MC is longer. Both plots are normalized.

Due to the different topology of  $B^0$  decay, the average momentum of  $K_S^0$  in generic MC is different from the ones from signal MC. While it's clear that the fraction of  $K_S^0$  decaying outside the IP is the majority in both MC samples and therefore there's no reason to constrain  $K_S^0$  decay vertices in IP. In general, the cut-based reconstruction for  $K_S^0$  is first performed by the selection of invariant mass from its decay products. After the selection on invariant mass is applied, a vertex fit for each  $K_S^0$  using charged pions' tracks is done without IP constraint. This reconstruction

is mainly achieved by using standard BASF2 particle list called “stdKshort:merged”. In this “stdKshort:merged” list, two  $K_S^0$  particle collections are first reconstructed and then merged.

We first take all the “V0” objects from BASF2 Datastore which use 2 online reconstructed charged tracks with opposite charges and a converged fitted vertex. The invariant mass “M” from two pions’ 4-vector is calculated. The  $K_S^0$  candidates with “M” between  $0.45 < M < 0.55$  GeV are selected, named “Ks:V0”. In addition to these  $K_S^0$  from “V0” objects, another  $K_S^0$  collection from offline reconstruction is also formed. In this step, charged tracks with mass hypothesis of  $\pi^\pm$  is used, which the tracks and PID of charged pions are pre-selected by the criteria in Table 3.1. Then  $K_S^0$  are found by combining all of these tracks and the candidates with “M” in between  $0.3 \sim 0.7$  GeV before the vertex fit are kept. Then, vertex fit is perform for these candidates and the ones that have converged vertices and  $0.45 < M < 0.55$  GeV are considered as the  $K_S^0$  candidates, named “Ks:reco”, which uses the same criteria as “V0”-based reconstruction. In both cases, the vertex fit is performed using “TreeFit”[23] that is the recommended algorithm in Belle II. It’s clear that there are duplication of  $K_S^0$  if two collections are merged directly. Therefore, the objects’ index of two daughters’ tracks in the Datastore are compared between  $K_S^0$  from these two collections, from which the identical combinations are removed to avoid duplication.

The  $B^0$  reconstruction efficiency is highly sensitive to the efficiency of charged pions because the final states particles are three identical  $K_S^0$  decaying to 6 charged pions. That’s why only a very loose selection on  $\pi^\pm$  is applied. The selected  $K_S^0$  collection using cut-based method therefore contains many fake candidates, see the distribution of “M” from cut-based selected  $K_S^0$  from signal MC in Figure 3-2.

Table 3.1: Pre-selection criteria of  $\pi^+\pi^-$  for  $K_S^0$  offline reconstruction.

Selection Criteria	$\theta$	CDC Hits Number	PID
CDC acceptance		$> 20$	pionID $> 0.1$

The  $K_S^0$  candidates from “stdKshort:merged” is the default way to obtain  $K_S^0$  in the current BASF2, however, the limitation of this cut-based  $K_S^0$  reconstruction is the

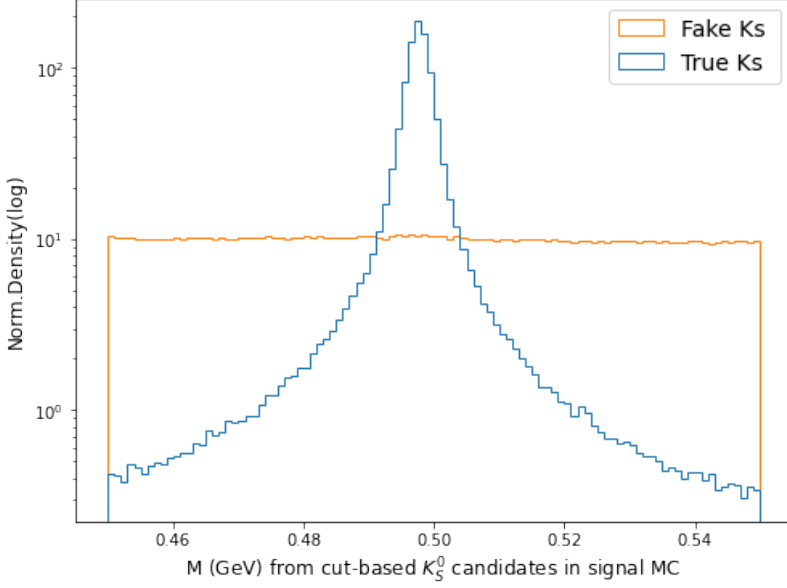


Figure 3-2: “M” of  $K_S^0$  from cut-based selection in signal MC (normalized). The blue line is the true  $K_S^0$  and the orange is the fake  $K_S^0$ .

pollution from fake  $K_S^0$ . Using these  $K_S^0$  candidates to reconstruct  $B^0 \rightarrow K_S^0 K_S^0 K_S^0$ , as long as one of three  $K_S^0$  is fake, the reconstructed  $B^0$  is fake, too. This creates high fake rates in  $B^0$  candidates and costs a large extra processing time for computing the kinematics and vertex fit of  $B^0$  which should be avoided. Further, the number of combinatorial backgrounds in  $B^0 \rightarrow K_S^0 K_S^0 K_S^0$  becomes high. It largely reduces the signal significance and introduce bias to the result of  $CP$  parameters. Thus, a multi-variate analysis (MVA) based  $K_S^0$  identification package, called “KsFinder”, is developed to further reject the fake  $K_S^0$  from cut-based selected candidates.

## 3.2 MVA-based $K_S^0$ Identification: KsFinder

### 3.2.1 Experience from Belle

As mentioned in the last section, in order to improve the reconstruction performance of  $K_S^0$  from cut-based selection, a MVA-based package called “KsFinder” has been developed. The reconstruction of  $K_S^0$  can be treated as a typical classification problem. The input is a set of observables that describes the characteristics of  $K_S^0 \rightarrow \pi^+ \pi^-$

decay. The training target is the true or fake flag from the MC truth-matching variable called “isSignal” where  $\text{isSignal} = 1$  ( $0$ ) stands for being a true (fake)  $K_S^0$ . In the experience of Belle, the  $K_S^0$  reconstruction was first done by using cut-based method to select primary candidates, then a MVA-based classifier was implemented by assigning two likelihood indicators to each  $K_S^0$  candidates. The package used by Belle is called “nisKsFinder”[9] conventionally. It outputs the two likelihood variables based on “NeuroBayes” algorithm[24], which defines the goodness of  $K_S^0$ , called “nb\_nolam” and “nb\_vlike”, respectively. As their names suggest, “nb\_nolam” is the likelihood of not being a  $\Lambda$  particle and “nb\_vlike” is the likelihood of being a V0-like particle. A good  $K_S^0$  candidate from “nisKsFinder” is the one with a low likelihood of being  $\Lambda$  particle and a high likelihood of being a V0-like particle, assuming the major backgrounds for  $K_S^0$  is the mis-identified  $\Lambda$  among V0-like particles. By putting cuts on these two variables, a purification of  $K_S^0$  can be made, see Figure 3-3. It can effectively reduce fake  $K_S^0$  from cut-based selected candidates, however, there are a few disadvantages about this method. First, “NeuroBayes” is a commercial product that was developed over 10 years ago. The official support and update is stopped nowadays, so it’s not an ideal method for an experiment like Belle II that has a quite long prospective in operation. Second, the classification is based on a joint cut on two variables, which might make the cut values hard to choose, for example, two different cuts might have very close purity. Last but not least, the classification of  $K_S^0$  is not the directly targeted output of the neuro-network. Instead, it classifies the V0-like particle and “ $\Lambda$ ”. Besides, the computation speed of this method is not very optimized compared to other popular methods in today’s view.

In Belle II, such a dedicated  $K_S^0$  classification tool is not implemented yet in BASF2 framework until 2019. Considered the limitation of Belle method, the development of  $K_S^0$  classifier demands another algorithm and structure. The stochastic gradient-boosted decision trees are widely employed for multivariate classification and regression tasks in modern high energy physics field. Particularly, a speed-optimized and cache-friendly implementation of such method called FastBDT (FBDT) is popularly used[25]. Compared to other popular classification algorithms such as TMVA,

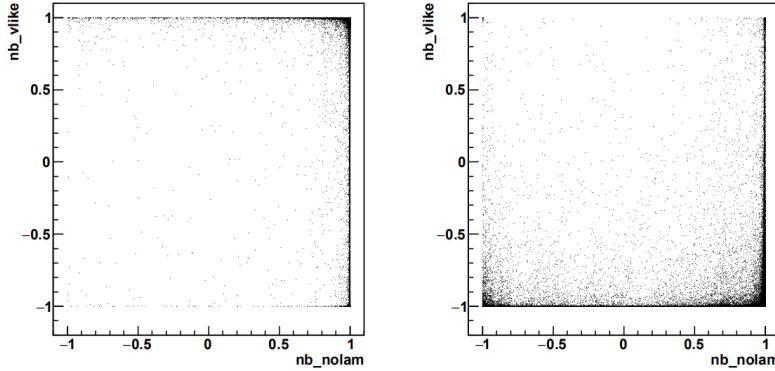


Figure 3-3: The distribution of two variables output from “nisKsFinder”: “nb\_nolam” and “nb\_vlike” for  $K_S^0$  candidates from Belle signal MC. The left is from true  $K_S^0$  and the right is from the fake  $K_S^0$ . In Belle, the standard cuts for  $K_S^0$  is  $\text{nb\_vlike} > 0.5$  and  $\text{nb\_nolam} > -0.4$ [13].

scikit-learn and XGBoost, FastBDT method is proven to be one order of magnitude faster during the training and applying phases[25].

### 3.2.2 FastBDT algorithm

As the basic component of BDT, a general DT (decision tree) performs classification using a number of consecutive cuts at each tree nodes, where tree nodes are distributed on the layers of a tree. The maximum number of the layers is called “depth of tree” and it’s a hyper-parameter of a DT. Each data point contains labels (variables) called “features” in DT. There are generally two phases in using DT for classification. One is “training” (or “fitting”) phase that determines the best cut at each nodes. The other is called “applying” phase that uses a trained DT to classifier a new data set. In training phase, training data points are fed to a DT and separated based on their features. At each node with a cut value, a cumulative probability histogram (CPH) can be defined by counting the signal and background data points. The histograms are used to determine the separation gain for a cut value at each position in these histograms. The feature and cut value (or equivalently bin) with the highest separation power are used as the cut for the node. Hence, each cut value locally maximizes the separation gain between signal and background on the given training sample. Eventually, on the last layer (called terminal layer), the signal fraction of all

training data points in the same terminal node is used for the signal probability for a testing data point which ends up in the same terminal nodes, shown as Figure 3-4. In applying phase, a new data set, such as a test sample, is fed to the trained DT with fixed cut values at each nodes, to evaluate the performance of a DT or use it to separate the signal and background.

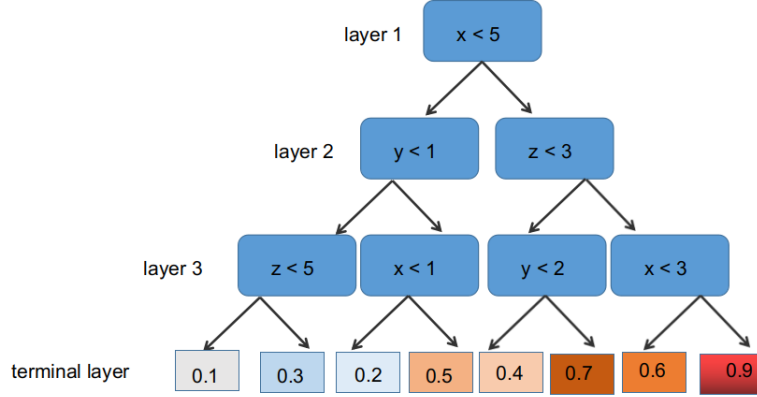


Figure 3-4: Basic structure of a DT with depth = 3 and labels (features) of x,y,z. The terminal layer contains training data points and are separated by cuts on layer 1 to 3. The number (color demonstrated) is the signal fraction of training data points in each terminal node, which is used for testing data points signal probability.

The mathematical idea behind this method is to treat the data points as a data set defined on a multi-dimension hyper-space. As long as the signal/background data points show certain concentration in a sub-region of the hyper-space, it's possible to locally increase the signal fraction by consecutively cutting on the edge where signal and background are separated. The cut on labels at each node is the edge of the sub-region. A very deep DT (too many layers) means the edges of the sub-region of the hyper-space is cut too finely so that even small statistical fluctuation could be separated. Therefore, training data points in the sub-region can give a over-fitted signal fraction. As a result, the classifier is over-trained and performs poorly on new data points since the fluctuation is random in new data set. There are pruning algorithms which automatically remove cuts prone to over-training from a DT, details can be found here [26].

Avoiding the over-training of a DT limits the depth of a tree strongly. For a

problem of  $K_S^0$  classification, the number of observables (features) is much more than the usual tree depth (a few layers). A single DT can only roughly separate the signal and background and thus, it's called a weak-learner. To improve the separation power, a sequence of many shallow DTs is formed during the training phase. For all the DTs, a negative binomial log-likelihood loss-function is minimized in the training phase. By using the results from many DTs (many weak learners), a well-regularized classifier with large separation power is constructed. The number of trees  $N$  is called “boosting steps”, which is also the hyper-parameters for the training model. Such improved model is called “Boosted Decision Trees” (BDT). There are a few different strategies to further optimize the performance of BDT such as “Gradient Boost Decision Trees” and “Stochastic Gradient Boost Decision Trees” which use different methods to define the model output or increase the training speed, details are discussed here[27].

The FastBDT implements a optimized algorithm from a derived Gradient BDT method (GBDT)[28] and gain an order of magnitude faster execution time. The comprehensive comparison between FastBDT and other popular methods in Belle II scope is described in here [25].

### 3.2.3 Decay Topology of $K_S^0 \rightarrow \pi^+\pi^-$

The first step for developing  $K_S^0$  MVA classification is to determine the input variables for FastBDT method which should represent the decay feature of  $K_S^0$ . The remaining background of  $K_S^0 \rightarrow \pi^+\pi^-$  after the cut-based reconstruction comes from different resources. In these resources, the main contributions are false combination of tracks, V0-like particle mis-identification, and looped tracks.

The false combination of tracks includes two major cases. First is when one of the two daughter is  $\pi^{+/-}$  and the other is not. This often happens when a charged pions from a neutral mother with a capability of decaying into multiple charged tracks, like  $D^+ \rightarrow \mu^-\nu_\mu K^-\pi^+$ . On the other hand, it's also possible that both of two tracks are correctly reconstructed from  $\pi^{+/-}$  but they are not from the same mother, or the mother is not a  $K_S^0$  particle due to the missing of other daughters, such as  $D^+ \rightarrow K_S^0(\rightarrow \pi^+\pi^-)\pi^+$ . The decay shape resembled the above cases are illustrated

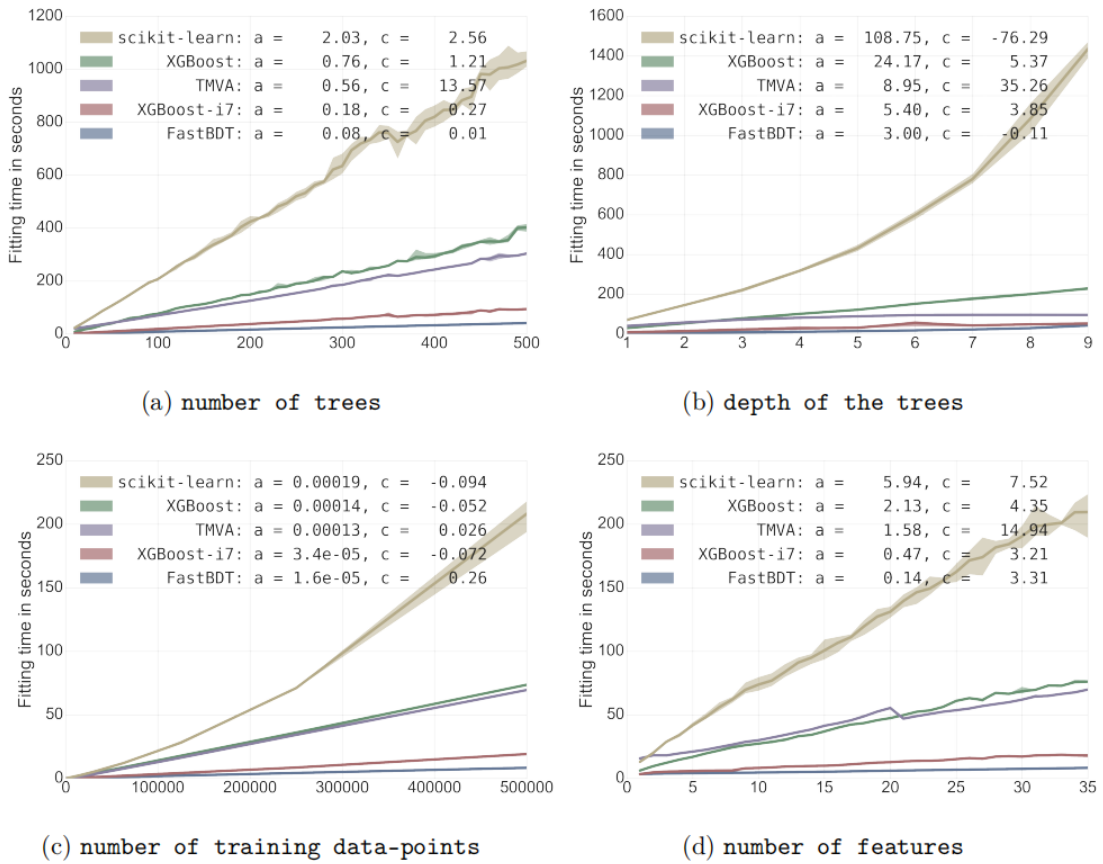


Figure 3-5: Runtime in fitting phase with different hyper-parameters comparison among FastBDT and XGBT, TMVA, scikit-learn.[25]

as the following:

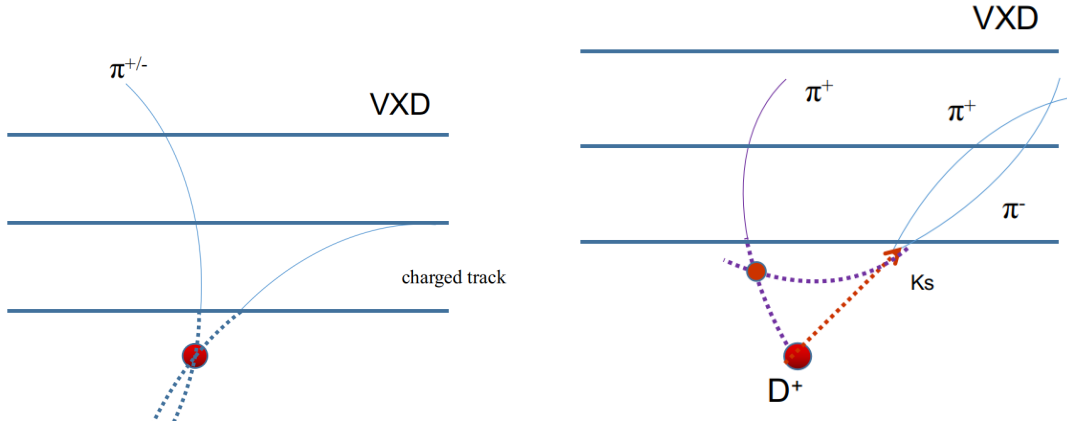


Figure 3-6: The left shows the case when a charged track (not a pion) combined with a true pion as a fake  $K_S^0$ , the right shows the case when two daughters are correctly reconstructed as pion but not from the correct mother.

The V0-like particles mainly refer to  $K_S^0$ ,  $\Lambda$  and  $\gamma$ .  $\gamma \rightarrow e^+e^-$  yield is significantly lower than the previous two types and the mass difference between pion and electron is very large, so the PID values can be used to well-distinguish them. As for the contribution of  $\Lambda \rightarrow p^+\pi^-$ , it's happens when the positive charged tracks (proton track) is wrongly identified as  $\pi^+$ , see Fig 3-6 left. The key observable to distinguish this background is the invariant mass of mother particle, which  $\Lambda$  is at 1.115 GeV, much larger than the  $K_S^0$ . The left-over  $\Lambda$  after the cut-based reconstruction is minimal and can be further reduced by checking the PID information of the positive charged daughter.

When a charged pion only carries a minimal of its mother's transverse momentum  $p_T$ , the curvature of its track may form a self-loop of which radius is comparable with the size of Belle II detector (mainly VXD and CDC) in  $r - \phi$  plane. In this case, one charge pion could leave two charged tracks candidates with the opposite charge and similar  $p_T$ , with a possibility to form a converged vertex. Thus it also gives a potential fake  $K_S^0$ , see Fig 3-6 right.

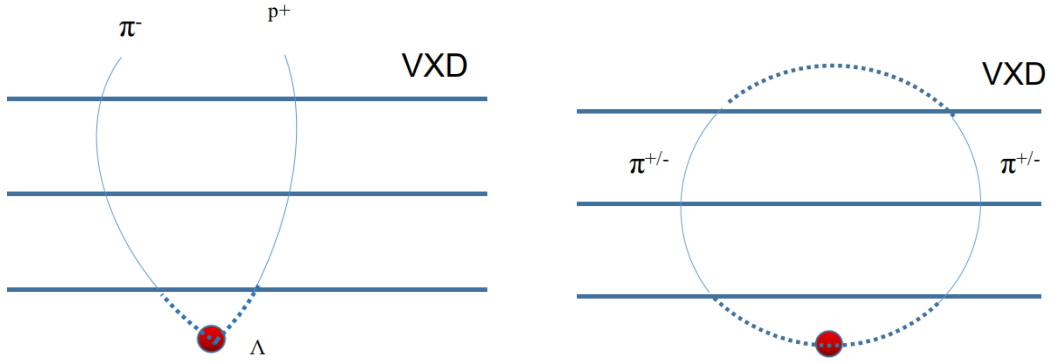


Figure 3-7: The left shows the  $\Lambda \rightarrow p^+\pi^-$  decay shape that can be treated as  $K_S^0$ , the right shows a self-loop formed by a low  $p_T$  charged pion reconstructed as two separated tracks with a vertex

### 3.2.4 Determination of training observables from $K_S^0$ decay

Given the characteristics of  $K_S^0 \rightarrow \pi^+\pi^-$  discussed in the previous section, a set of observables as training features of FastBDT classifier can be constructed. The set includes categories of observables: kinematics, decay shape parameters , particle identifications and detector hits information. Observables are listed below with a sketch showing the shape parameters of  $K_S^0$  decay in Fig 3-8.

- Kinematics
  - Invariant mass of  $K_S^0$  before and after fitting vertex
  - momentum of  $K_S^0$  and  $\pi^{+/-}$ , vectors and magnitudes.
- Decay shape parameters
  - cosine angle between  $K_S^0$  vertex and momentum.
  - helicity angle of two daughters in reference of  $K_S^0$  momentum.
  - decay angle of two daughters in the mother's frame.
  - flight distance projection on  $K_S^0$  momentum direction.
  - significance of flight distance, defined by ratio of flight length and its uncertainties.

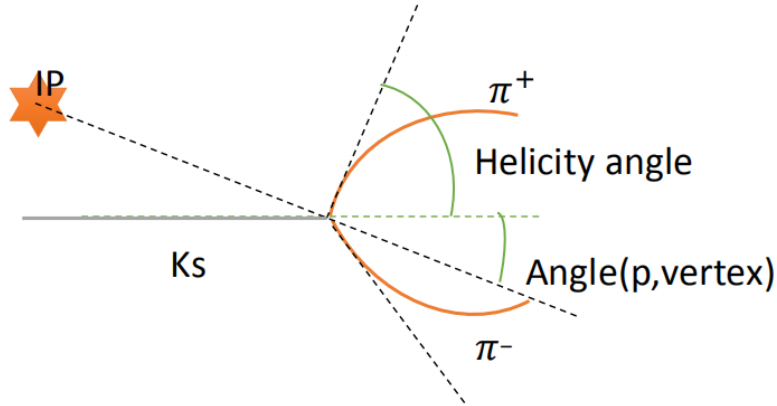


Figure 3-8: The decay shape parameters, vertex vector takes IP as origin.

- distance on z-axis of two daughters helix
- impact parameters on  $K_S^0$  vertex
- Particle identifications
  - pion-ID for  $K_S^0$  daughters.
  - muon-ID for  $K_S^0$  daughters.
  - proton-ID for  $K_S^0$  positive charged daughter.
- Hits information
  - the number of PXD hits for each  $K_S^0$  daughter, up to 2.
  - the number of SVD hits for each  $K_S^0$  daughter.

The decay shape category is of the most importance because it demonstrates the best separation power. For instance, if a false combination is made of two tracks, it's likely that the momentum direction of reconstructed fake  $K_S^0$  is not aligned with the vertex position. So the projection of flight length on the momentum could be negative value for background. While in case of a true  $K_S^0$ , such projection is almost always a positive value.

There are a few points to be checked for using FastBDT classification, given the nature of the algorithm. First, the distribution of the observables should be different

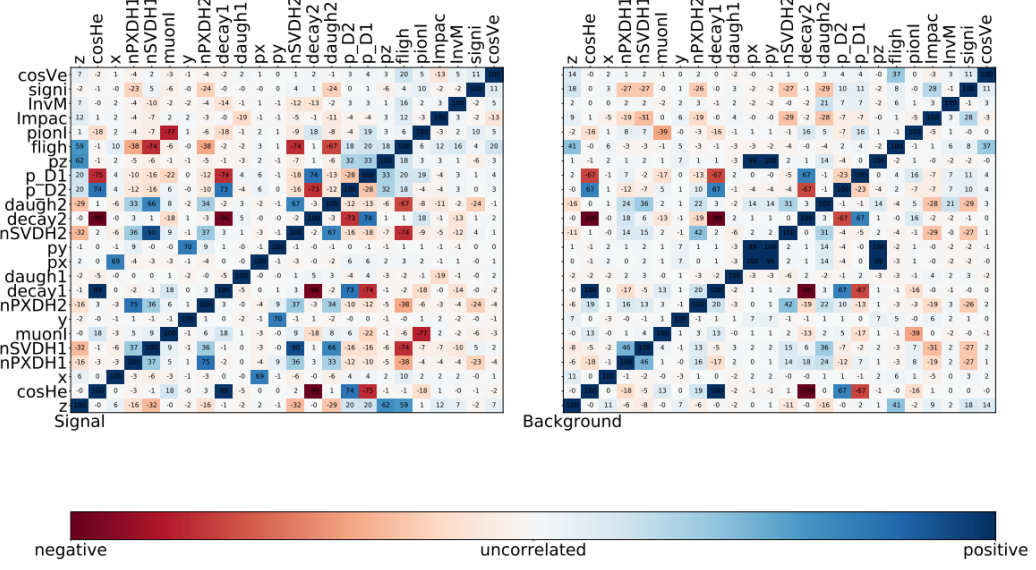


Figure 3-9: The correlation matrix of the chosen observables. It shows different correlation between observables in signal and background. And there's no single observable showing strong correlation with all other members.

in true  $K_S^0$  and background, so the FastBDT classifier can perform distinguish the true and the fake at each nodes to maximize the separation gain, just as Section 3.2.2 discussed. Secondly, there will a correlation among the training observables and they should also be different in signal and background. The boosting phase will create a sequence of shallow DTs whose structures are not same. Different correlations helps improve the performance of DTs in tuning of structure. For instance, a true  $K_S^0$  flights longer by larger momentum in general, so its daughters' detector hits number becomes fewer. Then these two observables have negative correlations in true  $K_S^0$ . In case a fake  $K_S^0$ , the flight length could be a deep outside of VXD but daughters may have full VXD hits, without clear correlation. At last, one should also avoid using many observables with too strong correlations since the classifier won't gain much improved separation power when put a cut on each of them. The correlation of the observables in signal and background samples are shown in Fig 3-9. The selected observables meets the requirements for classification.

### 3.2.5 Training, Testing and Application of KsFinder

Training samples of  $K_S^0$  are first extracted based on “stdKshort:merged” from generic  $B^0$  decay and  $B^0 \rightarrow K_S^0 K_S^0 K_S^0$  using MC13 samples, respectively. For the hyper-parameters of FastBDT method, the depth of each DT is 3 and the number of total trees (boosting steps) is 200, with a balance of computing time and performance. The training target variable is “isSignal” flag. The ratio between the true and fake  $K_S^0$  is 1:1 in both training and testing sample. The training sample and testing sample are separately prepared using different input file from MC13. The distribution of observables in true and fake samples (from  $B^0 \rightarrow K_S^0 K_S^0 K_S^0$ ) are shown in the Appendix A. The abbreviations of those variables and their importance rank are shown in Table 3.2 and 3.3.

### 3.2.6 The Performance and Over-fitting check

The performance of classifier is evaluated by applying it on a independent data sample. So in the accordance of training data used, the same amount of events are prepared. Since the training is performed on three different types samples, three classifiers are actually obtained. Signal efficiency and background rejection are calculated using the output of trained classifier that presents the likelihood of probability of being a true  $K_S^0$ , as defined in Eq (3.1) and Eq (3.2).

$$\text{signal efficiency} = \frac{\text{Number of true } K_S^0 \text{ with output} > \text{cut value}}{\text{Number of all true } K_S^0} \quad (3.1)$$

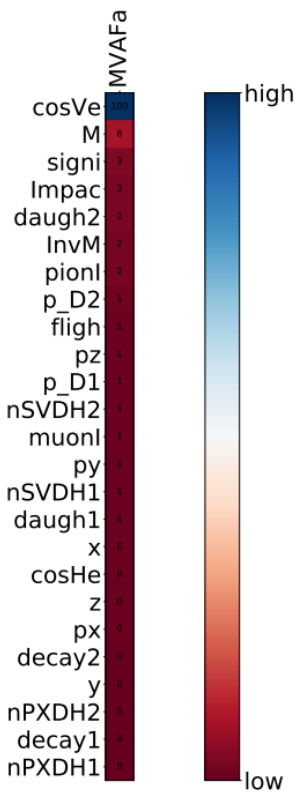
$$\text{background rejection} = \frac{\text{Number of fake } K_S^0 \text{ with output} < \text{cut value}}{\text{Number of fake true } K_S^0} \quad (3.2)$$

Using the weight file created by the training process, the output between 0 and 1 is assigned to every candidates as a quality index standing for the likelihood to be true  $K_S^0$  that can be used as a cut. In order to check the performance of the classification, the ROC (receiver operating characteristics) curve is plotted, which shows the dependence of rejection power regarding the signal purity. The larger

Table 3.2: The Abbreviations.

Observables	Abbreviations
nPXDHits_D1	nPXDH1
decayAngle_D1	decay1
nPXDHits_D2	nPXDH2
y	y
decayAngle_D2	decay2
px	px
z	z
cosHelicityAngleMomentum	cosHe
x	x
daughtersDeltaZ	daugh1
nSVDHits_D1	nSVDH1
py	py
muonID_pi	muonI
nSVDHits_D2	nSVDH2
p_D1	p_D1
p_D2	p_D2
pz	pz
flightDistance	fligh
pionID_pi	pioni
InvM	InvM
daughterAngle2body	daugh2
ImpactXY	Impac
significanceOfDistance	signi
M	M
cosVertexMomentum	cosVe

Table 3.3: Importance rank



area a ROC curve is covered, meaning that background rejection drops slower when increasing classifier cut, the better performance is achieved. Three classifiers are tested with generic  $B^0$  decay, and  $B^0 \rightarrow K_S^0 K_S^0 K_S^0$  to check the robustness of classifier. The ROC, signal efficiency and purity are shown:

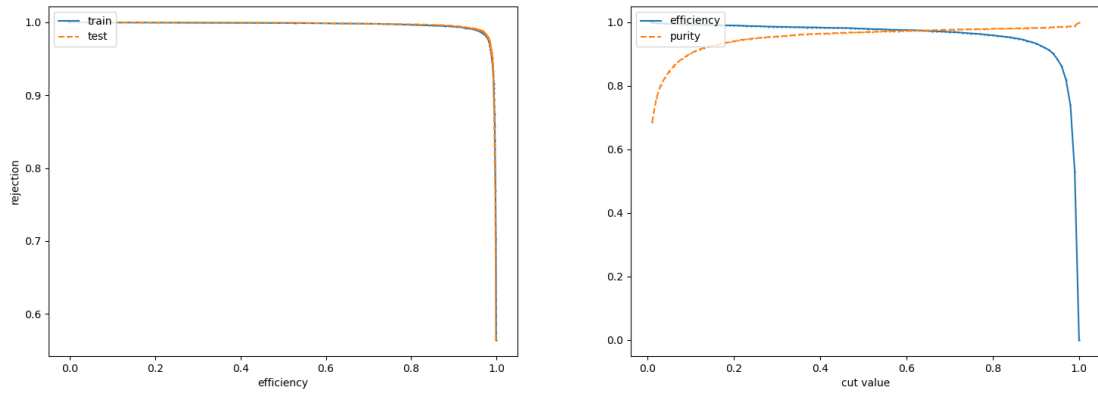


Figure 3-10: The left is ROC curve(blue for training and orange for testing) and the right is efficiency and purity (blue for efficiency and orange for purity) depending on cut of classifier output. Results are from  $B^0 \rightarrow K_S^0 K_S^0 K_S^0$  sample.

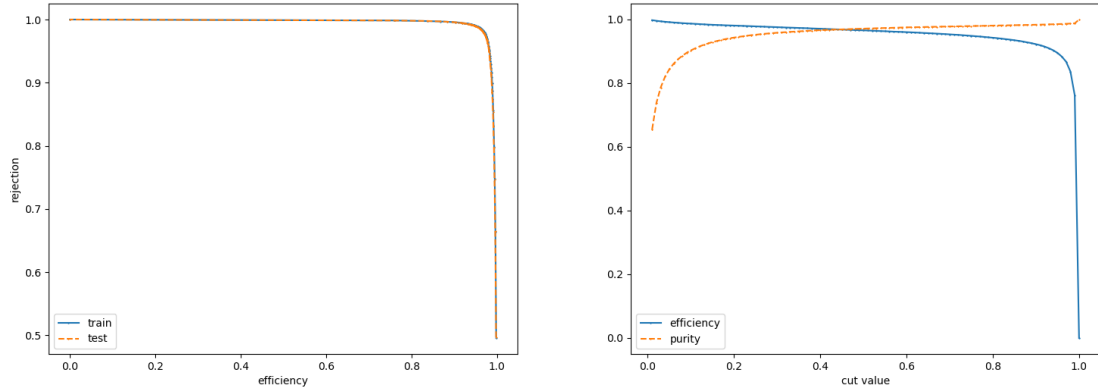
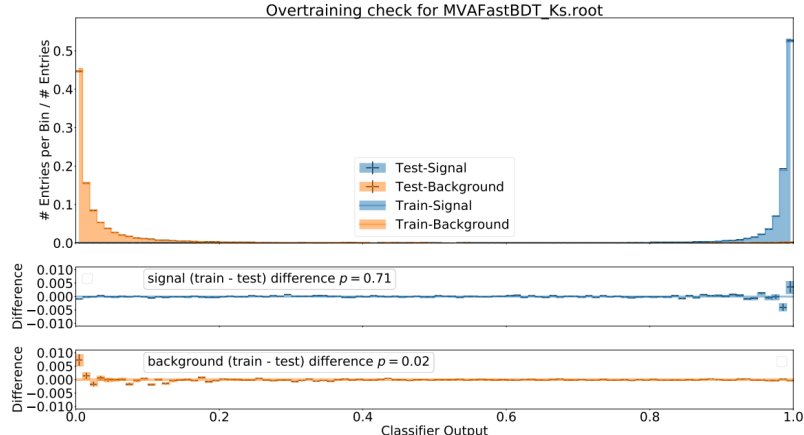


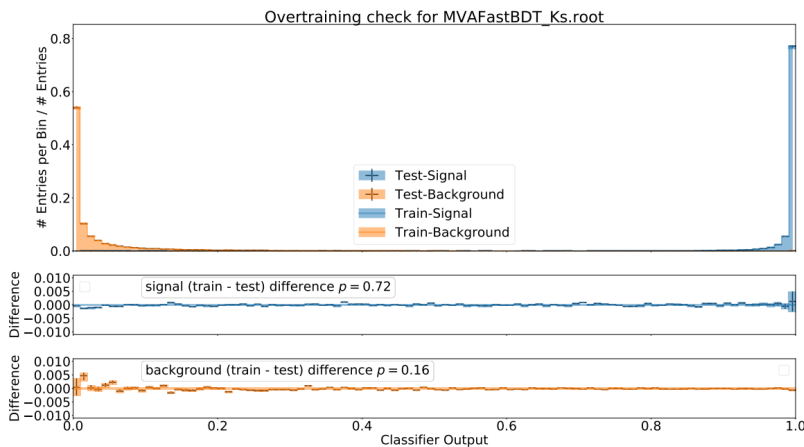
Figure 3-11: The left is ROC curve (blue for training and orange for testing) and the right is efficiency and purity (blue for efficiency and orange for purity) depending on cut of classifier output. Results are from  $B^0$  generic decay sample.

The ROC curves show a good rejection power on classifiers. To be noted, the curves are consistent in training and testing samples. While the ROC curve has shown the absence of noticeable over-fitting in classification, the detailed check can be made by comparing the distribution of classifier output on true and fake  $K_S^0$  respectively in training and testing. In the classifiers we obtained, results from training and testing

are very much close thus no over-fitting is spotted, as shown in Fig 3-13.



a) Over-fitting check for  $B^0 \rightarrow K_S^0 K_S^0 K_S^0$ .



b) Over-fitting check for  $B^0$  generic decay.

In order to use the output of KsFinder, a cut value must be chosen. The output of KsFinder is named “FBDT\_Ks”. Here we can define a “Figure of Merit” (FOM) to determine the cut value. S and B is the number of true and fake  $K_S^0$  after the cut, respectively. The value of 0.74 of “FBDT\_Ks” maximize the KsFinder output in  $B^0 \rightarrow K_S^0 K_S^0 K_S^0$ , so we will use this value as only  $K_S^0$  with larger “FBDT\_Ks” will be kept from cut-based selection.

$$\text{FOM} = \frac{S}{\sqrt{S + B}} \quad (3.3)$$

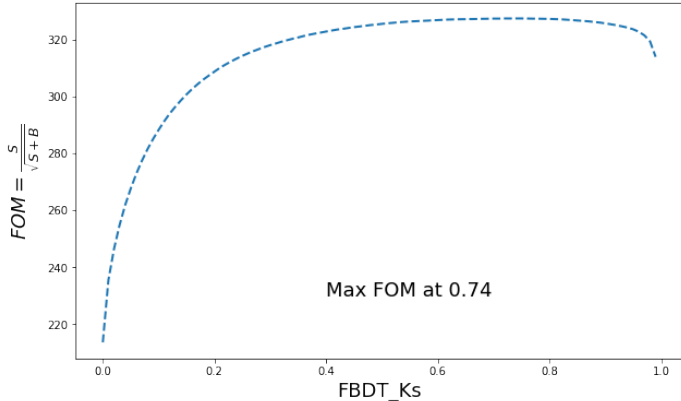


Figure 3-13: FOM of classifier output (FBDT\_Ks) in  $B^0 \rightarrow K_S^0 K_S^0 K_S^0$ , maximum value is obtained at 0.74 and curve is almost flat after 0.5.

By comparing the fitted invariant mass of  $K_S^0$  before and after the application of this cut, it's clear that the fraction of background has been largely reduced and most of the signal remains. The true  $K_S^0$  fraction in the pre-selected  $K_S^0$  before applying KsFinder cut is 39%, and 95.3% of them are remained after KsFinder applied. The fake  $K_S^0$  fraction before applying KsFinder cut is 61%, and 97.6% of them are rejected after KsFinder applied. A much cleaner  $K_S^0$  candidates is created as shown in Fig 3-15.

### 3.2.7 Data Validation for Classifier

The results from MC studies show an excellent performance of KsFinder. However, such classification is based on the observables reconstructed from MC samples, and FastBDT algorithm is depending on the training features apparently. As a result, the validation of such tool on the real experiment data is necessary. This would justify the usage of classifier on data and is also essentially helpful to check the potential discrepancy between MC and data.

The validation comes from the following aspects. First of all, since there's no “isSignal” truth in real data, there's no way to direct check performance on data. Since the FastBDT method is based on the distribution of training variables, if these variables shows close distribution among MC and data, then the classification performance is expected to be close.

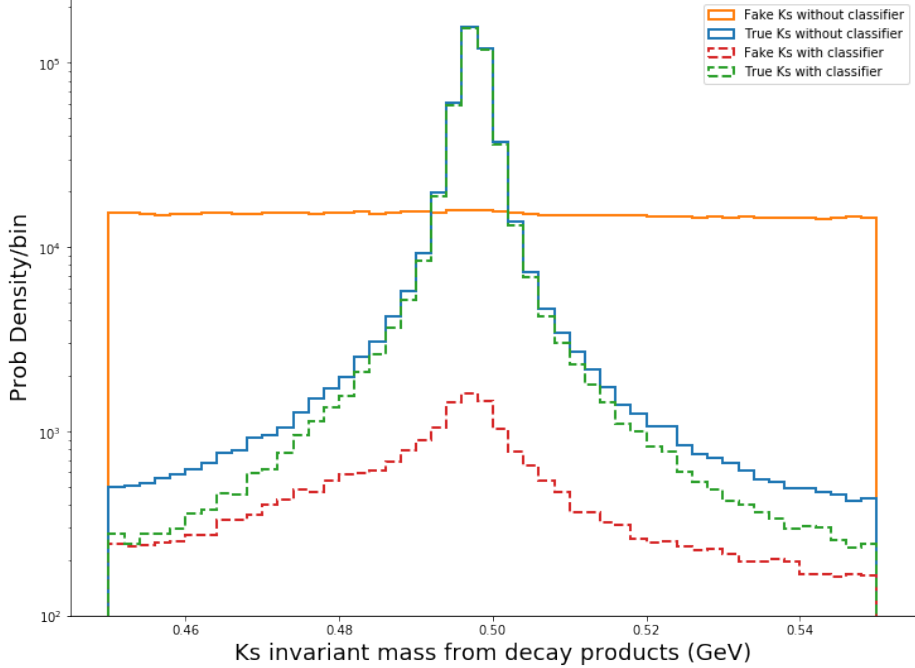


Figure 3-14:  $K_S^0$  purity improvement with cut value of FBDT\_Ks at 0.74 applied. Blue solid line is true  $K_S^0$  before KsFinder and green dashed line is the true  $K_S^0$  after. The orange solid line is fake  $K_S^0$  before KsFinder and red dashed line is fake  $K_S^0$  after. 95.3% of true  $K_S^0$  are kept while 97.6% the fake are rejected by the classification.

Thus, variables must be compared between data and MC to ensure the consistence. Then, the expected performance represented by the distribution of selected  $K_S^0$  should be similar between data and MC. Particularly, since  $K_S^0$  candidates will be used for further reconstruction of  $B^0$ , its kinematics such mass and momentum may change after the classifier application, so the validation that approves no clear bias on  $B^0$ 's  $M_{bc}$  and  $\Delta E$  which are used for  $B^0$  reconstruction is also needed.

We take the small data sample from Belle II early phase 3 operation experiment 7 and 8 in 2019 for comparison. The integral luminosity at  $\Upsilon(4S)$  resonance is about  $5.17 \text{ fb}^{-1}$ . MC13 sample is extracted from generic  $B^0$  decay with equivalent events number. There are two campaigns of MC included (MC12b and MC13, later one is the latest). Fig 3-16 shows the invariant mass and momentum distributions from data and MC samples, and full comparison of all training variables is included in Appendix B. Most of the distribution shows a good consistence before and after using KsFinder. It shows that kinematics of  $K_S^0$  in data and MC yield fairly close distributions and

no clear bias is seen by applying the KsFinder cut.

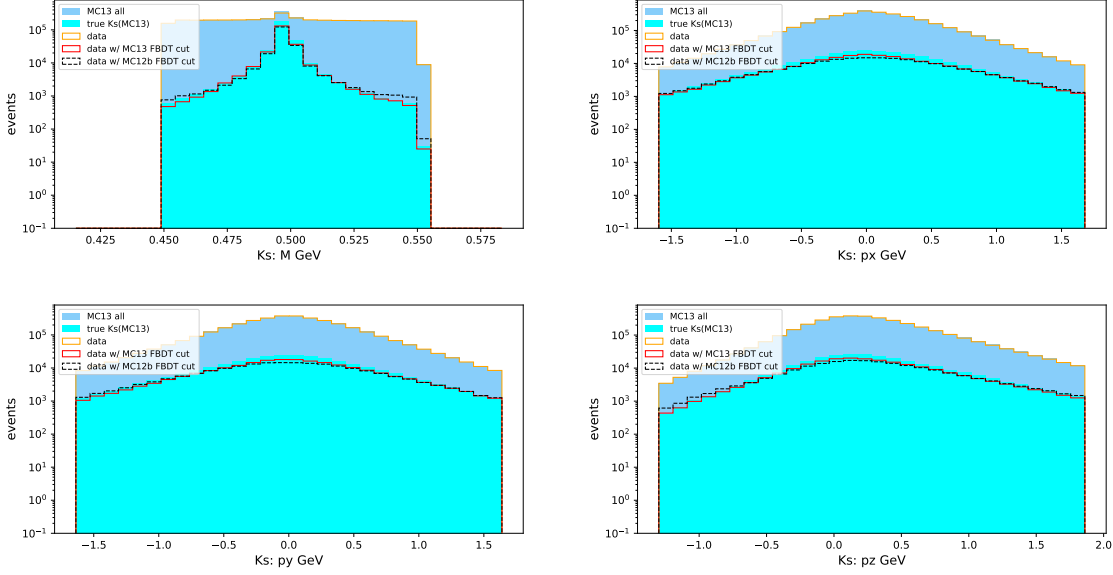


Figure 3-15: The distribution of invariant mass from daughters and the momentum of x,y,z direction. Blue bar is from all MC13, cyan bar is the true  $K_S^0$  in it. Yellow step histogram is data with no cut, solid red data with MC13 trained cut, and the dashed is with MC12b cut. Experimental data has a good agreement with MC before and after applying the KsFinder.

### 3.2.8 KsFinder Effects on Kinematics Evaluation

Implementing KsFinder for  $K_S^0$  may induce extra bias on the event numbers for  $K_S^0$ . It's not easy to directly evaluate the impact of each variables in training towards the final signal yield because the output is non-linear dependence on those variables. However, we can directly use the output of KsFinder and introduce the scale factor when checking the data and MC signal yields.

A fit on invariant mass  $M$  of  $K_S^0$  candidates after varied cut on KsFinder output is done by modeling signal shape as double-Gaussian and background as Chebyshev polynomial. Significance is defined as  $S_{data/MC} = N_{signal}/N_{total}$  in data and MC from fitting using RooFit. A list of intervals of cut value on KsFinder output is made and the significance is calculated within each interval. Fitting results are shown in Fig 3.17 using loose and tight cut respectively. The fit plots in all cut intervals are

included in Appendix C. Data/MC correction is defined as:

$$R = \frac{S_{MC}}{S_{data}} \quad (3.4)$$

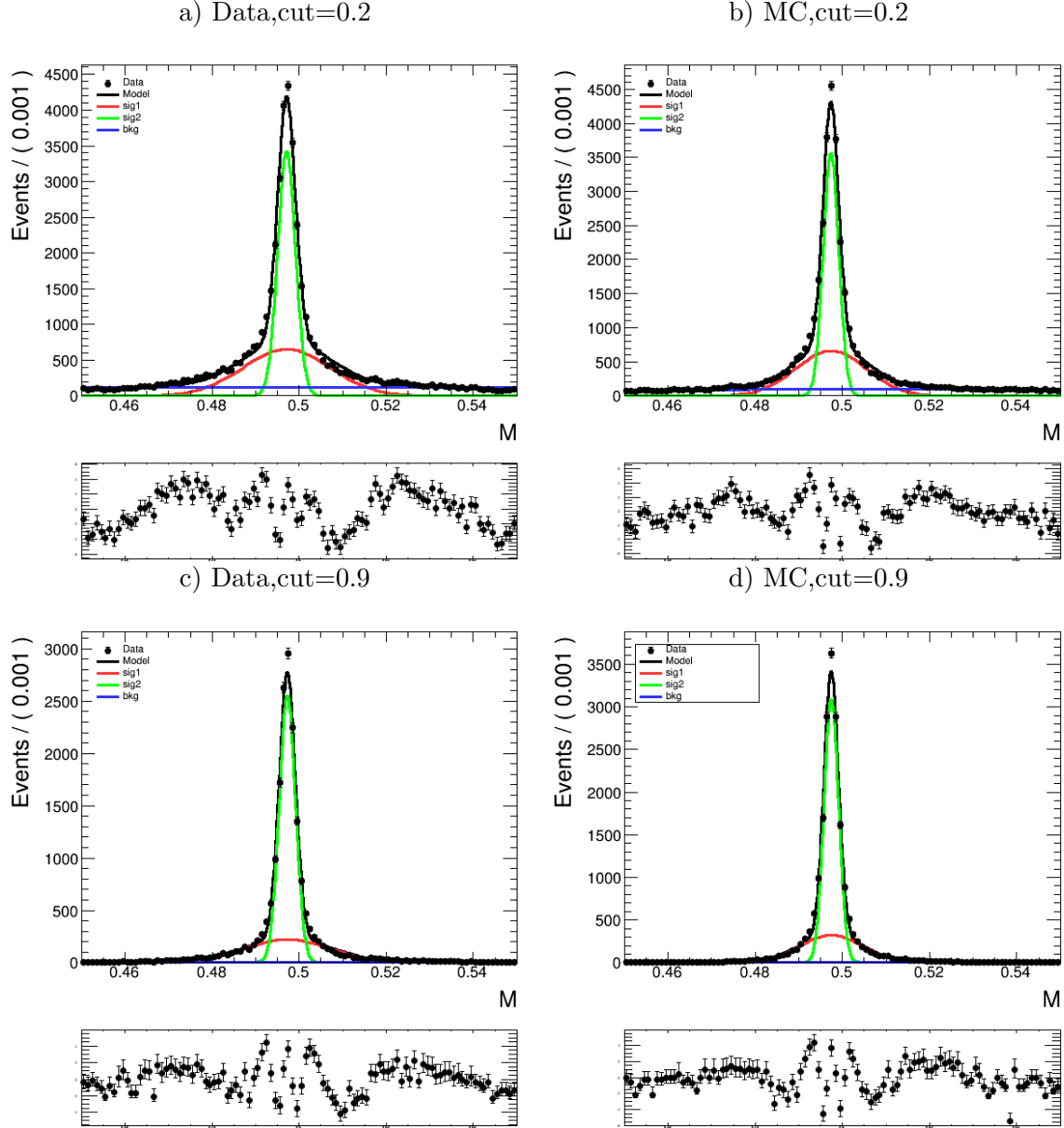


Figure 3-16: Invariant mass fit of  $K_S^0$  using cut at 0.2(loose) and 0.9(tight) to calculate  $S_{data/MC}$ .

The correction is defined by taking the R value within the chosen interval. Uncertainty of R is defined by the difference of maximum and minimum of R in all intervals. R is distributed as:

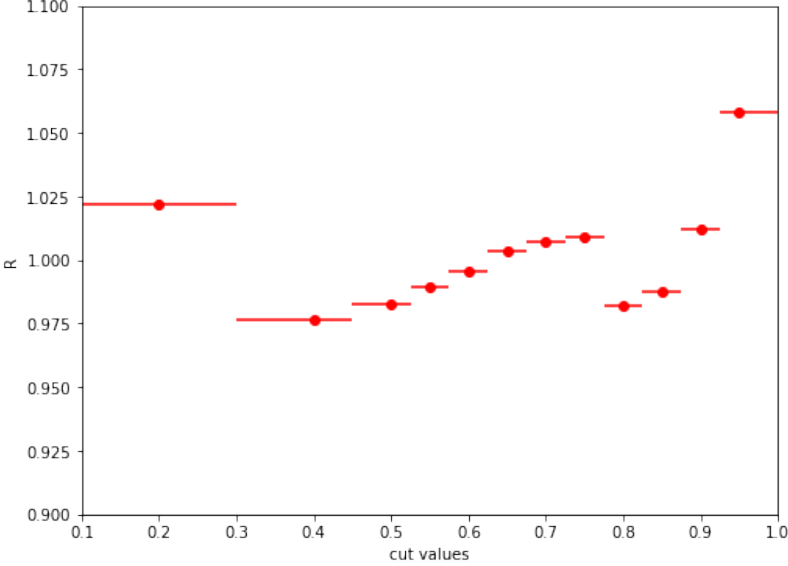


Figure 3-17: Data MC correction induced by  $K_S^0$  classifier.

The R, for example in cut value 0.74 of maximum FOM, is  $R = 1.009 \pm 0.081$ . In  $B^0 \rightarrow K_S^0 K_S^0 K_S^0$ , the correction of  $B^0$  events should be proportional to R to the three. Correction that is implemented for  $B^0$  is  $1.027^{+0.33}_{-0.18}$ . In most of the cut intervals, the R is within 2.5% so the bias on  $K_S^0$  numbers is very small.

### 3.2.9 Summary

The development of Belle II  $K_S^0$  classifier is enlightened by the experience from Belle. A comprehensive study of training observables from  $K_S^0$  decay characteristics has been exploited. It takes the advantage of FastBDT algorithm to achieve a high fake rejection power. As a result, classifier is able to give an output which can be used as a cut to select good  $K_S^0$  candidates with high purity. The classifier is validated with real experimental data as well. A primary data validation study of KsFinder is conducted with implementing correction on data and MC along with its contribution to  $B^0$ . The performance of KsFinder is in a good shape and no clear bias is found on the yield of the number of  $K_S^0$ . For the reconstruction of  $B^0 \rightarrow K_S^0 K_S^0 K_S^0$ , the development of KsFinder is critical to suppress large fraction of combination background from fake  $K_S^0$ .

# Chapter 4

## Analysis Strategies

### 4.1 Data Sample and Event Selection

The simulation data (MC) is taken from Belle II official MC campaign 13, named MC13. Both signal MC and generic MC are produced. In signal MC, one of the  $B^0$  from  $\Upsilon(4S)$  decays into final states  $3K_S^0$  then into 6 charged pions, while the other  $B^0$  decays generically using all possible channels. In generic MC,  $B^0$  from  $\Upsilon(4S)$  all decay generically using all possible channels.

The signal MC sample is produced by EvtGen package with provided “decay.dec” file that describes the required decay mode and branching fraction. As  $K_S^0 \rightarrow \pi^0\pi^0$  leads to large background with poor vertex quality, only the final states to 6 charged pions is used. The corresponding branching fraction used is  $\mathcal{B}(B^0 \rightarrow K_S^0 K_S^0 K_S^0) = 6.0 \times 10^{-6}$ . The simulation takes the  $\Upsilon(4S)$  as the mother particle and uses decay mode “VSSBMIX” to generate its decay process to two scalar  $B^0$  mesons with mixing. Then the  $B^0 \rightarrow K_S^0 K_S^0 K_S^0$  is simulated based on only the possible phase-space of kinematics that final states could have, which no  $CP$  violation parameters is used, so the generated sample in both generic and signal MC13 has zero input for  $\sin 2\phi_1$  and  $\mathcal{A}$ . In this analysis of  $B^0 \rightarrow K_S^0 K_S^0 K_S^0$ , 1 million signal MC events with and without overlay of beam background are generated separately independent from physics runs, and  $1\text{ab}^{-1}$  generic MC is also generated.

### 4.1.1 $K_S^0$ Selection

Benefiting from the KsFinder,  $K_S^0$  reconstruction is first based on the cut-based selection, then candidates are purified largely by cutting on the KsFinder output. Here two major additional selections are used in addition to the cut-based method in section 3.1. Firstly, in order to reduce the impact from slow pions from  $D^*$  decays,  $K_S^0$  momentum is set to larger than 0.05 GeV/c, see Fig 4-1. Secondly, regarding the different tracking quality of daughter  $\pi^{+/-}$ , the distribution of fitted invariant mass named “InvM” of  $K_S^0$  are varied. So based on the SVD hits number pions from  $K_S^0$  have, different cuts of fitted invariant mass “InvM” are used on the  $K_S^0$  to further improve the reconstruction purity, see the discussion in detail as Fig 4-5 shows.

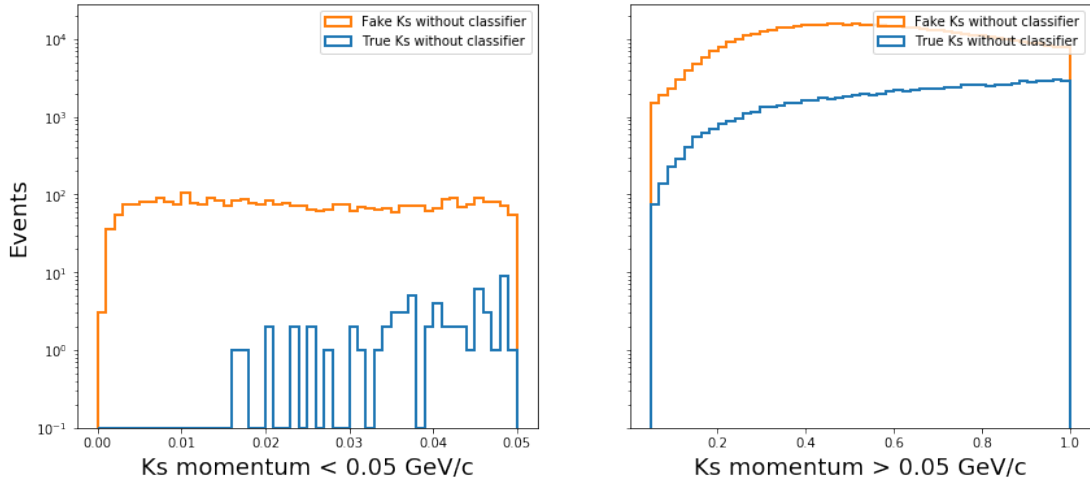


Figure 4-1: The distribution of  $K_S^0$  momentum. Candidates smaller than  $0.05\text{GeV}/c$  are rejected.

The reconstruction quality of  $K_S^0$  highly depends on the flight distance.  $K_S^0$  that decay in the inner region of VXD yields more hits on the SVD layers from its charged daughters, which is critical in performing a proper tracking. An essential difference between Belle and Belle II is the level of beam background which Belle II is around  $10 \sim 20$  times higher regarding the luminosity. So the CDC of Belle II becomes much more sensitive to this effect when doing track finding. Track finding is performed on VXD and CDC separately. The track candidates from different sub-detectors then merged into a same track by extrapolating the trajectory and pattern matching.

However, for certain fraction of  $K_S^0$ , they decay outside of layer 5 of SVD, and if these tracks are not passing the windmill structure of SVD, there will be no SVD information recorded. This is due to the feature of SVD track finding, where a track candidate needs either at least 3 SVD hits to form a SVD-only track, or 2 hits to form a hit double-lets, to be used for combining tracks with other track candidates. Single hit case is filtered out to suppress the large fraction of beam background induced by fake hits on a single layer. This effect is shown in Fig 4-2. Similar to Fig 3-1,  $K_S^0$  are categorized based on how many SVD hits their daughters have. SVD10 and SVD01 stands for  $K_S^0$  that only  $\pi^+$  and  $\pi^-$  has non-zero SVD hits number. SVD11 and SVD00 stands for  $K_S^0$  that both or neither charged pions have SVD hit non-zero SVD hits number. This is related to the track quality of  $K_S^0$  such that SVD11  $K_S^0$  has the best quality and SVD00 has the worst. It's clear that SVD00  $K_S^0$  show up at about 10 cm where SVD layer 5 is placed at  $r = 10.5$  cm. And most of SVD10(SVD01)  $K_S^0$  also show at same range because one of the pions is passing the overlapping area. The structure of SVD is shown in Fig 4-3 and the fraction for each types of  $K_S^0$  in  $B^0 \rightarrow K_S^0 K_S^0 K_S^0$  is listed in Table 4.1.

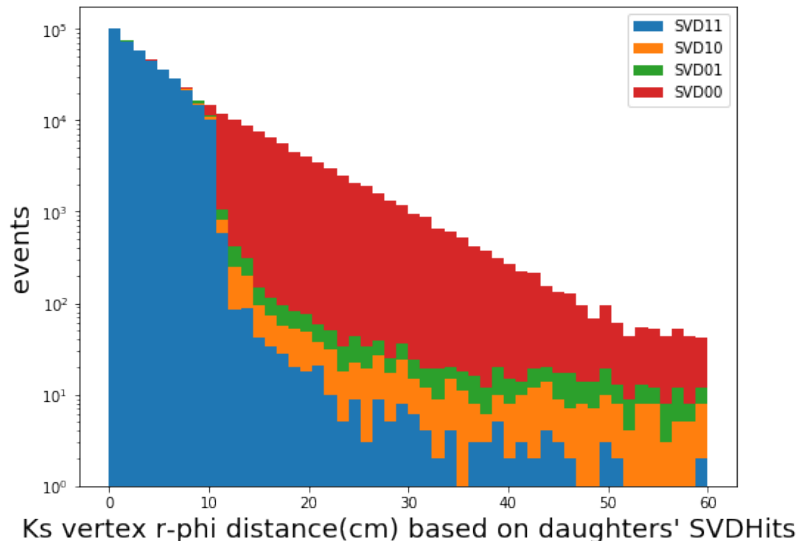


Figure 4-2:  $K_S^0$  flight length on  $r-\phi$  plane based on pions SVD hits, SVD11: both pions have SVD hits, SVD10(SVD01), positive(negative) pions have SVD hits, and SVD00: no SVD hits from pions. The result is from MC13 signal of  $B^0 \rightarrow K_S^0 K_S^0 K_S^0$ .

$K_S^0$ type	SVD11	SVD00	SVD10	SVD01
% in Belle II	52%	39%	5%	5%

Table 4.1: The fraction of each types  $K_S^0$  based on pions SVD hits in  $B^0 \rightarrow K_S^0 K_S^0 K_S^0$  MC in Belle I & II.

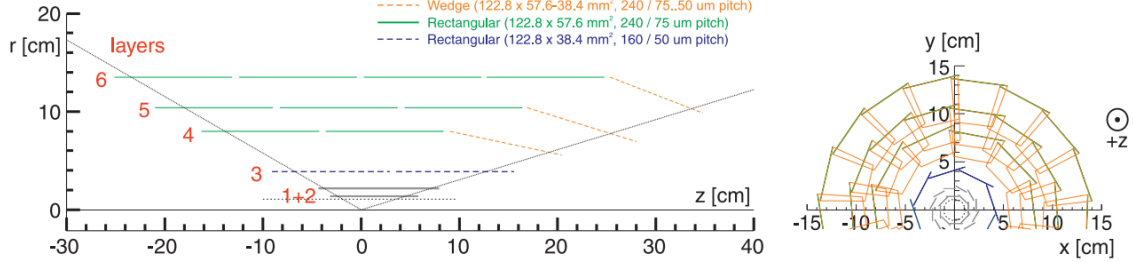


Figure 4-3: Layer 5 is at  $r = 11\text{cm}$  and  $K_S^0$  that decay outside are very likely to lose SVD hits information. Right figure shows the windmill structure with overlapping area at edges.

The vertex fit of  $K_S^0$  is performed using TreeFit package. [29] Using fitted  $K_S^0$  momentum and energy as four-vector, fitted invariant mass (called InvM) is different from the one obtained directly using daughters' four-momentum (calle M). This quantity often receive impact of the measurement uncertainties. If we check out the distribution of fitted invariant mass based on daughters' SVD hits. The dispersion is much severe in  $B^0 \rightarrow K_S^0 K_S^0 K_S^0$  than it is in generic sample due to the larger fraction of long flight length  $K_S^0$ , see Fig 4-4.

Using the fitted invariant mass (the bottom left in Fig 4-4), a slight tuned mass window can be set on each  $K_S^0$  type and improve the purity. We apply the cut on InvM based on  $K_S^0$  types to reduce background in mass sideband. Details of the InvM window are in Table 4.2.

In summary, we first select  $K_S^0$  using “stdKshort:merged” from BASF2 library, which the internal cut on M is 0.45 to 0.55 GeV/c and all converged vertex fit candidates are kept using TreeFit. Then we reject  $K_S^0$  candidates with momentum smaller than 0.05 GeV/c. After this, InvM cut on each  $K_S^0$  types are applied and finally the candidates are selected by KsFinder cut at 0.74.

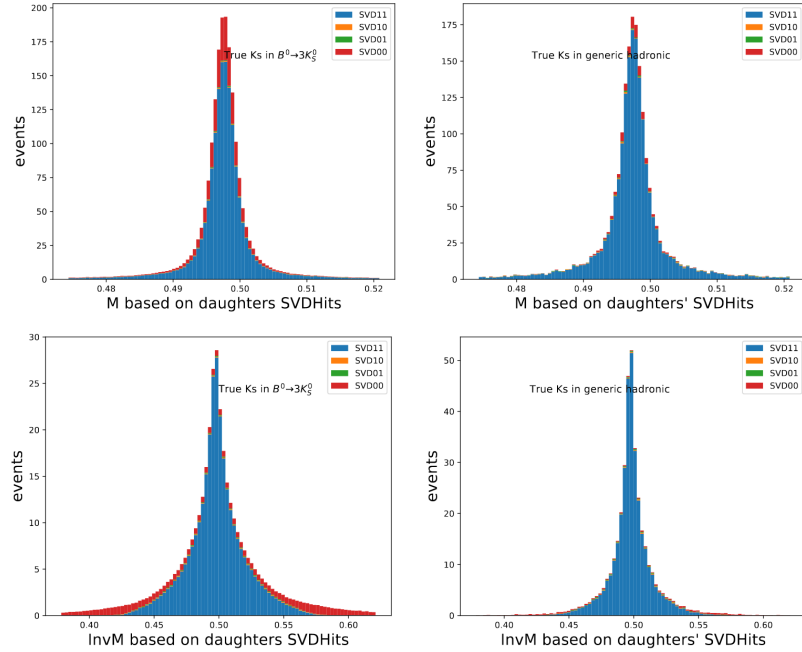


Figure 4-4: (Top two plots)The invariant mass from daughters' 4-vector named M, the left is  $B^0 \rightarrow K_S^0 K_S^0 K_S^0$  and the right is generic MC; (bottom two plots)The invariant mass from fitted 4-vector named InvM, the left is  $B^0 \rightarrow K_S^0 K_S^0 K_S^0$  and the right is generic MC; In both cases, the red shows the clear dispersion on SVD00 type  $K_S^0$ .

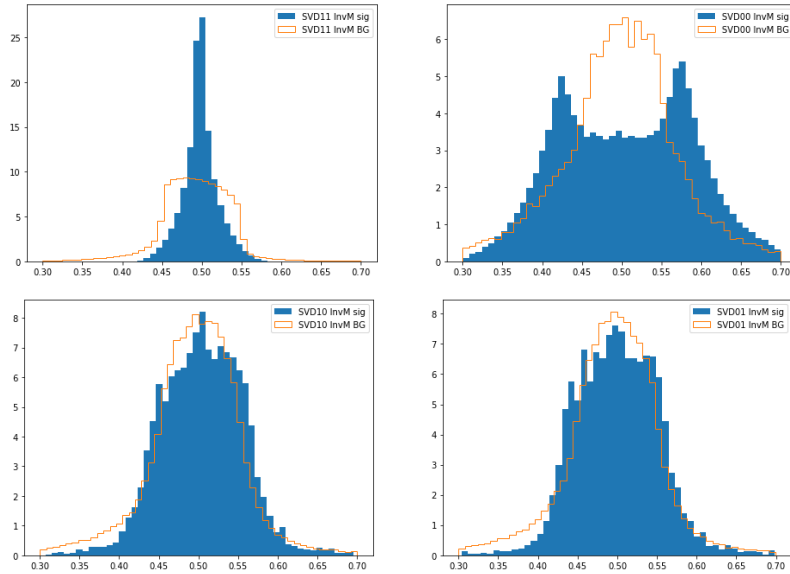


Figure 4-5: Fitted invariant mass on  $K_S^0$  types, sideband is excluded in each distribution to further reject fake  $K_S^0$

$K_S^0$ type	SVD11	SVD10	SVD01	SVD00
InvM window (GeV)	(0.45,0.55)	(0.38,0.7)	(0.38,0.7)	(0.3,0.7)

Table 4.2: fitted invariant mass window used for  $K_S^0$  based on Fig 4-6.

### 4.1.2 $B^0$ Signal Reconstruction

By combining three  $K_S^0$  particles from selected dataset, we can reconstruct  $B^0$ . The beam-constraint mass  $M_{bc}$  and energy difference  $\Delta E$  are used to extract signal. The  $B^0$  candidates with  $M_{bc} > 5.2$  GeV and  $|\Delta E| < 0.2$  GeV are accepted. Then the vertex fit using TreeFit is performed on each  $B^0$  candidate and we keep ones with chiProb  $> 0.001$ . When multiple  $B^0$  candidates show up in a single event, a rank by their vertexing quality is performed using  $\chi^2$  of the vertex fit, where the smallest have the highest rank. The best candidates are selected by the highest rank. Since the BCS is based on the vertexing quality that might introduce bias in the vertex positions for  $CP$  fit, we check the distribution of the vertex  $\chi_2$  from TreeFit before the BCS is used, as shown in Fig 4-6 top right. The distribution of candidates number per event without BCS is shown in top left of Fig 4-6 as well, showing small difference between data and generic MC. The distribution of candidates per event is consistent with the one from signal MC (bottom left of Fig 4-6). The 2D distribution of  $M_{bc}$  and  $\Delta E$  from  $B^0 \rightarrow K_S^0 K_S^0 K_S^0$  signal MC13 is shown in Fig 4-6 bottom right.

The summary of  $B^0$  selections for is:

$B^0$	$M_{bc}$ /GeV	$\Delta E$ /GeV	chiProb	Rank	FBDT_CS	FBDT_Ks
Selection	$> 5.20 \& < 5.29$	$ \Delta E  < 0.2$	$> 0.001$	= 1	$> 0.66$	$> 0.74$

Table 4.3:  $B^0$  selection criteria

where FBDT\_CS is for continuum suppression which is covered in the next section.

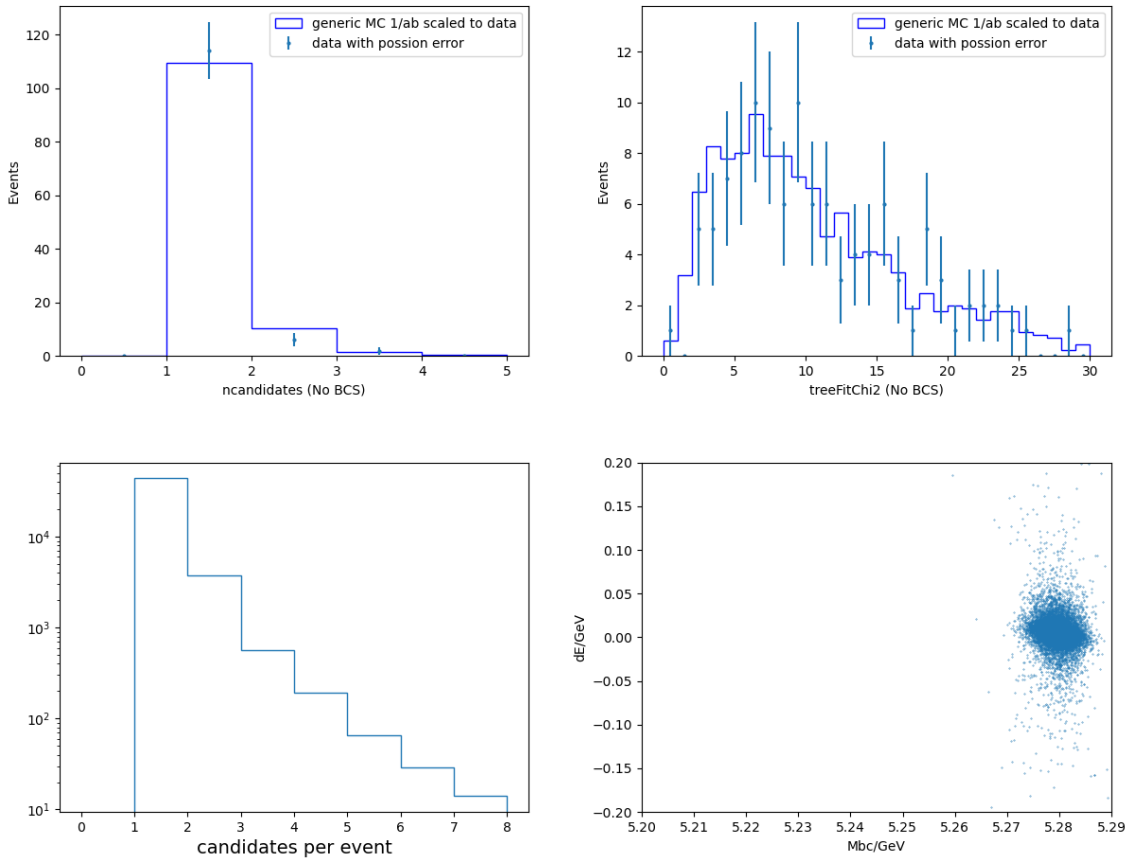


Figure 4-6: Top left is the candidates per event in data and generic MC before the BCS. Top Right is the  $\chi_2$  for data and generic MC before BCS. Bottom left is the number of candidates  $B^0$  per event from signal MC. Bottom right is the 2D  $M_{bc}$  and  $\Delta E$  distribution from signal MC.

The Table 4.4 shows that, given the newly developed  $K_S^0$  selection, efficiency of  $B^0$  reconstruction as well as purity is slight improved in Belle II compared to Belle.

event selection	efficiency	purity	$f_{MB}$	BCS
Belle Standard	35%(33%)	96%(99%)	6%(6%)	83%(96%)
Belle II (BG1)	36%(34%)	96%(98%)	(4%)(4%)	95%(96%)
Belle II (BG0)	40%(36%)	96%(99%)	(3%)(3%)	97%(97%)

Table 4.4: The efficiency is defined by the fraction of best candidates among the MC input number. Purity is the fraction of true  $B^0$  in best candidates.  $f_{MB}$  stands for multiple  $B^0$  events fraction in signal. BCS is the fraction of best candidates being a true signal. All values in the parenthesis are calculated in  $|M_{bc}| - 5.28 < 0.1$  and  $|\Delta E| < 0.1$ , or called “signal region” where efficiency is lower but purity is higher.

#### 4.1.3 Continuum Suppression

The production cross-section of  $B\bar{B}$  from  $\Upsilon(4S)$  receives a sizable contribution from other flavor of quarks other than b quark. This calls a demand to distinguish a specific  $B\bar{B}$  decay events from combinatorial background from  $e^+e^- \rightarrow q\bar{q}$ , so called continuum suppression. The background shape projection on spectrum of  $M_{bc}$  is a continuum shape. The rejection of this background is essential since they are the dominated background. In the case of  $b \rightarrow s$  charmless decay like  $B^0 \rightarrow K_S^0 K_S^0 K_S^0$ , the number of continuum background can exceed the signals by a few orders of magnitudes. They can be reduced by taking advantage of the difference on kinematics of their decay products. It’s also useful to perform a decay products angular distribution study to further reduce the continuum background. In a  $B\bar{B}$  event, two mesons are produced almost at rest in the CMS frame since the resonance state  $\Upsilon(4S)$  is just slightly lighter than beam energy. As a result, decay products fly out more isotropically, compared to other lighter flavor decay which flying-out particles trajectories are more back-to-back distributed. Thanks to experience from ARGUS and CLEO collaboration[30], a set of practically useful variables has been implemented into BASF2 framework that can be used in continuum suppression. CLEO cones momentum can be presented as Eq (4.1), where  $p_i$  is momentum of particle i in Rest Of Event (particles in a event except for the ones used to reconstructed  $CP$ -side  $B^0$ ),  $\theta_i$  is angle against thrust of reconstructed  $CP$ -side B meson.

$$L_n = \sum_{i \in ROE} p_i \times |\cos\theta_i| \quad (4.1)$$

Not only the variables defined by CLEO cones of momentum are used, in fact, the modified Super Fox-wolfram momentum named KSFW momentum are calculated based on event-shape based variables from every event in Belle II case as well. KSFW momentum are defined as:

$$KSFW = \sum_{l=0}^4 (R_l^{so} + R_l^{oo}) + \gamma \sum_{n=1}^{N_t} |P(t)_n| \quad (4.2)$$

The first term is:

$$R_l^{so} = \frac{\alpha_{cl} H_{cl}^{so} + \alpha_{nl} H_{nl}^{so} + \alpha_{ml} H_{ml}^{so}}{E_{beam}^* - \Delta E} \quad (4.3)$$

when l is odd:

$$H_{nl}^{so} = H_{ml}^{so} = 0 \quad (4.4)$$

and in the meanwhile:

$$H_{cl}^{so} = \sum_i \sum_{jx} Q_i Q_{jx} |p_{jx}| P_l(\cos\theta_{i,jx}) \quad (4.5)$$

i runs over B daughters particles and jx for other particles in ROE. Q is charge and p is momentum for each particle.  $P_l(\cos\theta_{i,jx})$  is the l-th order Legendre polynomial of cosine of i and jx-th particles. On the other hand, for l is even,

$$H_{xl}^{so} = \sum_i \sum_{jx} |p_{jx}| P_l(\cos\theta_{i,jx}) \quad (4.6)$$

The second term in Eq (4.2), when l is odd:

$$R_l^{oo} = \sum_j \sum_k \beta_l Q_j Q_k |p_j| |p_k| P_l(\cos\theta_j, k) \quad (4.7)$$

$j$  and  $k$  runs over ROE particles and others are same as Eq(4.8). For even  $l$ :

$$R_l^{oo} = \sum_j \sum_k \beta_l |p_j| |p_k| P_l(\cos\theta_j, k) \quad (4.8)$$

$\beta$  is five Fisher coefficient to determine in training. Using above definitions, we can form the possibility density functions for KSFW, cosine angle against B meson thrust and  $\Delta Z$  of two side vertex. Then based on each event's variables' value, we can calculate a ratio as Eq(4.9), where the Likelihood  $L$  of signal and background are obtained from the possibility density functions, see Eq(4.10). The  $\mathcal{R}$  is:

$$\mathcal{R} = \frac{L_S}{L_S + L_B} \quad (4.9)$$

$$L_{S/B} = P(KSFW)_{S/B} \times P(\cos\theta_B)_{S/B} \times P(\Delta Z)_{S/B} \quad (4.10)$$

where  $P$  is probability density function for signal and continuum, regarding the discriminating variables in the parentheses. For example, the distribution of a variable called  $R_2$  that is the most important one shown in Fig(4-7) which possibility density function is varied in signal and background.

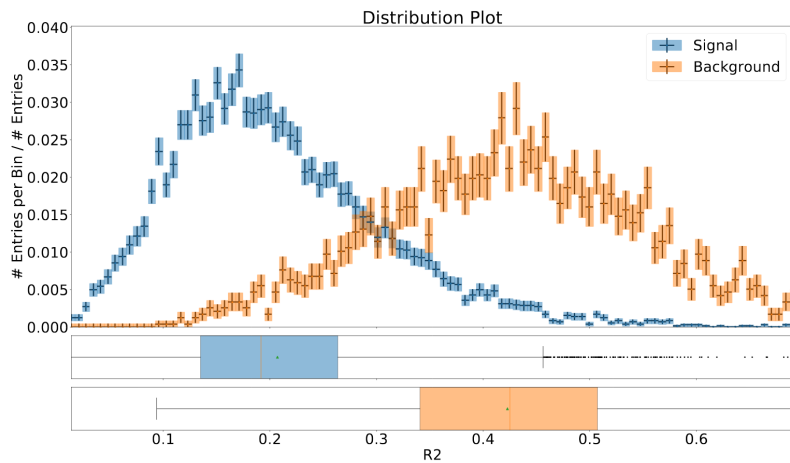


Figure 4-7:  $R_2$  serves as the highest weight as a variable in discriminating the continuum events, having a drastically different distribution between signal and background.  $R_2$  is the ratio of the second to the zeroth KSFW momentum in Eq(4.2)

In order to maximize the performance for this analysis, these categories of variables

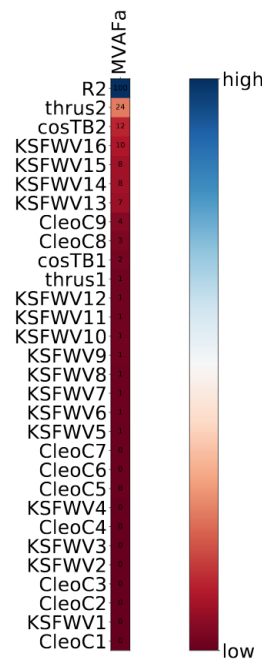
(KSFW, CLEO cone momentum and angular distributions) are combined as a training input for FastBDT classifier, and targeted variables is the continuum event flag. The working principles of this framework is much similar to KsFinder. The MC samples using signal  $B\bar{B}$  events and off-resonance in each of the flavor ( $q\bar{q}$ ) are prepared in a scaled ratio of their cross-section in  $\Upsilon(4S)$  energy. The same events reconstruction procedures for  $B^0$  is applied as well. Then the events passing the reconstruction for  $B^0$  are used for training the continuum suppression. The fraction of signal and background is set to 1:1 during the training. Noted that the ratio does affect the choice of cut value when applying the suppression. The 1:1 ratio is chosen to make classifier learns about signal and background equally. Then we determine the cut based on the curve of FOM like KsFinder. The variables used in training are listed in Table 4.5 with their abbreviations and importance rank is in Table 4.6.

The correlation between these training variables are shown in Figure 4-8. The correlation among the variables are varied in signal and background. Also, no strong correlation for one variable over the others is found, which shows a good selection of using these variables. The output of continuum suppression classifier is called “FBDT\_CS”.

Table 4.5: The Abbreviations.

Observables	Abbreviations
CleoConeCS(9,)	CleoC1
KSFVVariables(hoo1,)	KSFVW1
CleoConeCS(7,)	CleoC2
CleoConeCS(5,)	CleoC3
KSFVVariables(hso22,)	KSFVW2
KSFVVariables(hoo3,)	KSFVW3
CleoConeCS(4,)	CleoC4
KSFVVariables(hoo4,)	KSFVW4
CleoConeCS(3,)	CleoC5
CleoConeCS(6,)	CleoC6
CleoConeCS(8,)	CleoC7
KSFVVariables(hso14,)	KSFVW5
KSFVVariables(hso00,)	KSFVW6
KSFVVariables(et,)	KSFVW7
KSFVVariables(hso24,)	KSFVW8
KSFVVariables(hso04,)	KSFVW9
KSFVVariables(hso20,)	KSFVW10
KSFVVariables(mm2,)	KSFVW11
KSFVVariables(hoo2,)	KSFVW12
thrustOm	thrus1
cosTBz	cosTB1
CleoConeCS(1,)	CleoC8
CleoConeCS(2,)	CleoC9
KSFVVariables(hso02,)	KSFVW13
KSFVVariables(hoo0,)	KSFVW14
KSFVVariables(hso12,)	KSFVW15
KSFVVariables(hso10,)	KSFVW16
cosTBTO	cosTB2
thrustBm	thrus2
R2	R2

Table 4.6: Importance rank



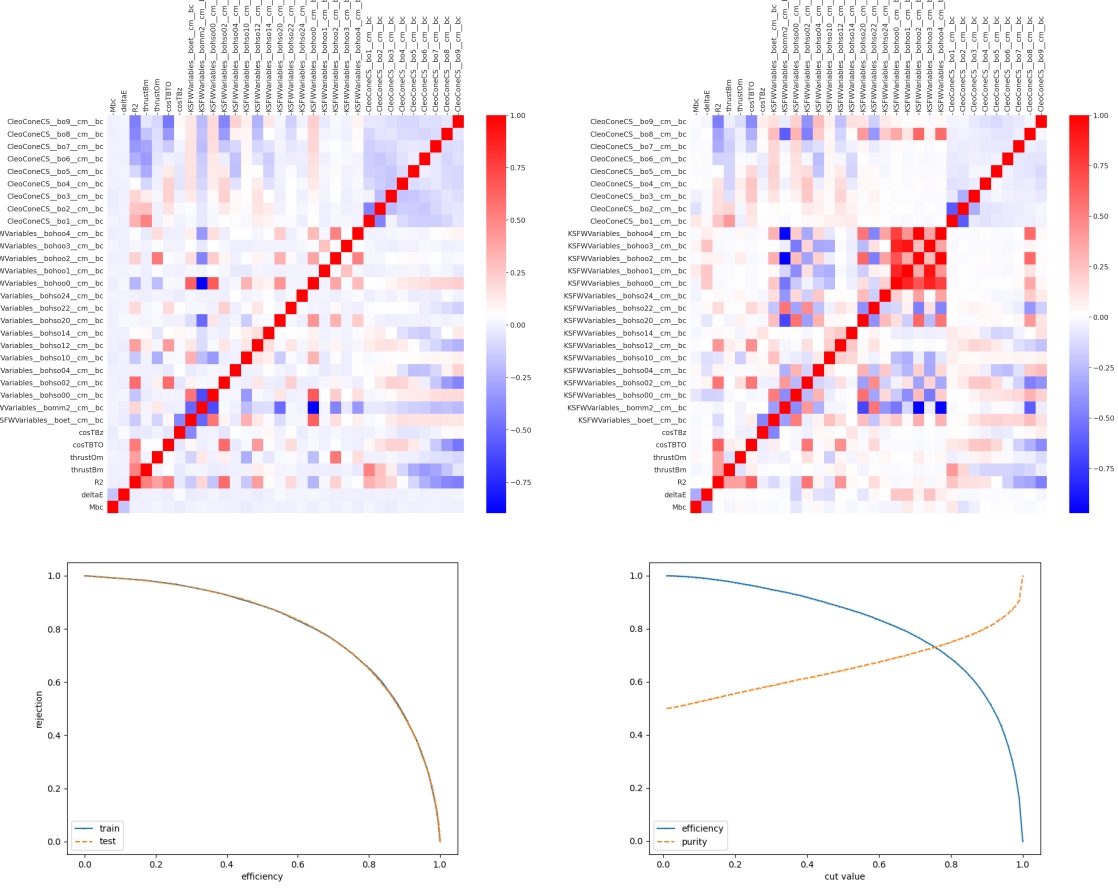


Figure 4-8: The top is correlation in variables for continuum suppression. Top left is for signal and top right is for background. The bottom left is the ROC curve (blue for training and orange for testing, in good consistence) The bottom right is the efficiency(blue) and purity(orange) regarding the cut value “FBDT\_CS”

Overtraining check is made by comparing the distribution of signal and background regarding the classifier output in both training and testing samples, which no clear difference is found thus no evidence of over-training found.

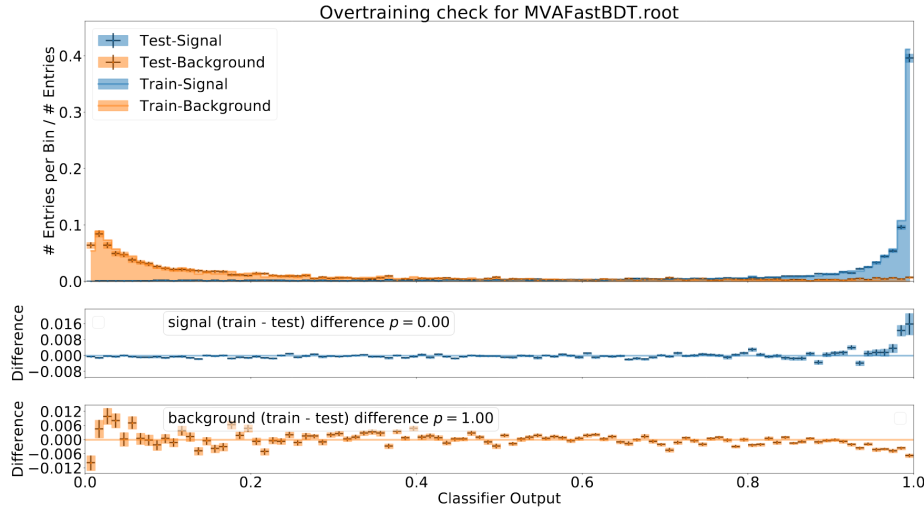


Figure 4-9: Over-training check of continuum classifier, where a very small difference in training and testing (1%) is found.

We implemented the continuum suppression by defining the cut at maximum of FOM using classifier output like Fig(4-10) shows.

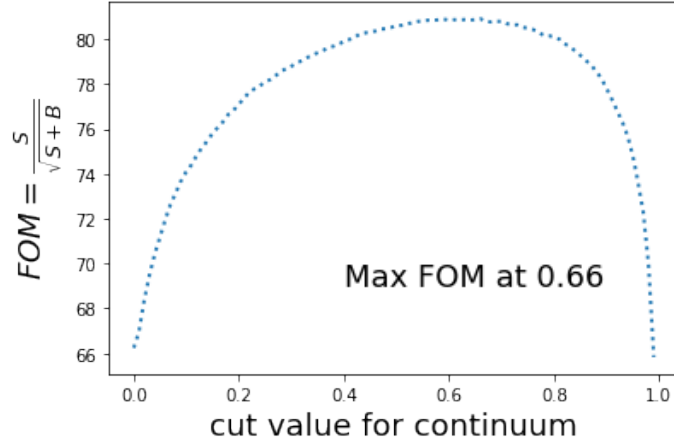


Figure 4-10: FOM depending on the cut value of continuum classifier output, cut value at 0.66 is used for continuum suppression.

#### 4.1.4 Resonance Background

Besides the major contribution from continuum background, charmonium resonance that mediates through  $b \rightarrow c$  transition brings odd  $CP$  eigenvalue in the final states as same as  $B^0 \rightarrow K_S^0 K_S^0 K_S^0$ . Monitoring their contribution is also important. Basically,

one needs to check the resonance states formed by two  $K_S^0$  with corresponding invariant mass. In  $B^0 \rightarrow X(K_S^0 K_S^0) K_S^0$ , there are two types of resonant events that give out same final states, one is resonant signal and the other is resonant background. For  $b \rightarrow s$  transitions as resonance signal because of the  $CP$ -even final states, X could be  $f_2(1270), f_0(1500), f'_2(1525), f_0(980), f_0(1710)$  and  $f_2(2010)$ . And for  $b \rightarrow c$  transition as resonance background because of  $CP$ -odd final states, X could be  $D^0, J/\psi, \psi(2S), \chi_{c0}, \chi_{c1}$ , and  $\chi_{c2}$ .

The number of these background in signal reconstruction could be further reduced by implementing veto on invariant mass of  $2K_S^0$ . However, such veto should be carefully validated with data. The distribution of invariant mass of X should agree well in MC and data. Some of these resonance have not been implemented inside generic MC production for Belle II. Given the very limited statistics of data accumulation we used in this analysis, we only present the expected number of these resonances in  $400\text{fb}^{-1}$  luminosity from generic  $\Upsilon(4S)$  events. These numbers should be re-checked in the future when data accumulation increases, and veto must be based on the structure of  $2K_S^0$  invariant mass from data as well. Details about the expected yields can be found in Table 4.6. Currently there is no veto used for rejecting the resonant background, which should be fine given the estimated background number is about 1 event.

#### 4.1.5 $B\bar{B}$ background and self-cross feed

Another possible contribution of backgrounds are the background from  $B\bar{B}$  events including the charged and the neutral ones. The estimated contributions of these types can be checked with charged  $B\bar{B}$  samples and the mixed samples. For this channel, the number of events from  $B\bar{B}$  is very limited. Self-cross feed backgrounds stands for the events from the signal-like events but the tag-side particles help form a fake signal. The combined contributions from  $B\bar{B}$  background and self-cross feed is about 3% in the channel and we don't perform special treatment on them at current luminosity.

Table 4.7: Expected yield for signal and background resonances  $2.14 \times 10^8 B\bar{B}$  in generic MC. The branching fraction of  $B \rightarrow XK_S$  and  $X \rightarrow 2K_S$  are listed for both PDG value and value in Belle II DEC. file. The number expected from  $CP$ -odd contamination is very low at current luminosity.

Resonances	$\text{Br}(B \rightarrow XK_S)\text{PDG}$	$\text{Br}(X \rightarrow 2K_S)$	$\text{Br}(B \rightarrow XK_S)\text{Dec.}$	$\text{Br}(X \rightarrow 2K_S)\text{Dec.}$	$B\bar{B}$ pairs	Expected yields
$D^0 K_S$	$2.6 \times 10^{-5}$	$1.7 \times 10^{-4}$	$2.6 \times 10^{-5}$	$1.8 \times 10^{-4}$	$2.14 \times 10^8$	0.134
$\eta K_S$	$3.45 \times 10^{-4}$	$< 3.1 \times 10^{-4}$	$4 \times 10^{-4}$	No Value	$2.14 \times 10^8$	No Value
$J/\psi K_S$	$4.35 \times 10^{-4}$	$< 1.4 \times 10^{-8}$	$4.35 \times 10^{-4}$	0	$2.14 \times 10^8$	0
$\psi(2S) K_S$	$2.9 \times 10^{-4}$	$< 4.6 \times 10^{-6}$	$2.9 \times 10^{-4}$	0	$2.14 \times 10^8$	0
$\chi_{c0} K_S$	$7.3 \times 10^{-5}$	$3.16 \times 10^{-3}$	$7.35 \times 10^{-5}$	$3.1 \times 10^{-3}$	$2.14 \times 10^8$	6.21
$\chi_{c1} K_S$	$1.96 \times 10^{-4}$	$6 \times 10^{-5}$	$1.96 \times 10^{-4}$	$1 \times 10^{-5}$	$2.14 \times 10^8$	0.05
$\chi_{c2} K_S$	$7.5 \times 10^{-6}$	$2.6 \times 10^{-4}$	$7.5 \times 10^{-6}$	$5.5 \times 10^{-4}$	$2.14 \times 10^8$	0.11
$f_2(1270) K_S$	$1.35 \times 10^{-6}$	$1.15 \times 10^{-2}$	$1.35 \times 10^{-6}$	$1.15 \times 10^{-2}$	$2.14 \times 10^8$	0.42
$f_2'(1525) K_S$	$1.5 \times 10^{-7}$	$2.22 \times 10^{-2}$	No value	0.22	$2.14 \times 10^8$	No Value
$f_2(2010) K_S$	$5 \times 10^{-7}$	No Value	No Value	No Value	$2.14 \times 10^8$	No Value
$f_0(980) K_S$	$2.7 \times 10^{-6}$	No Value	$2.75 \times 10^{-6}$	No Value	$2.14 \times 10^8$	43.3
$f_0(1710) K_S$	$5 \times 10^{-7}$	No Value	No Value	No Value	$2.14 \times 10^8$	No Value
$f_0(1500) K_S$	$6.5 \times 10^{-5}$	0.022	No Value	0.022	$2.14 \times 10^8$	No Value
Total	-	-	-	-	-	$\simeq 50$

#### 4.1.6 Signal Extraction

After determining the contribution of all kinds of background, the event selections defined in Table 4.3 is applied to signal MC, generic MC and also the data. The integral luminosity from generic MC is  $1\text{ab}^{-1}$  and the data used in this analysis is the full data set from 2019 and 2020 spring and summer. The official processing of data used is proc11 and bucket 9,10,11,13,14,15 and the integral luminosity is about  $62.8\text{fb}^{-1}$ . To be noticed, the good runs from data has slightly lower luminosity.

The unbinned maximum likelihood fit using RooFit package is performed to extract the signal. 2D fit using both  $M_{bc}$  and  $\Delta E$  are done by taking the probability density function as follows:

$$\mathcal{P}(M_{bc}, \Delta E) = f_{signal} \times \mathcal{P}_{sig}^{M_{bc}} \times \mathcal{P}_{sig}^{\Delta E} + (1 - f_{signal}) \mathcal{P}_{bkg}^{M_{bc}} \times \mathcal{P}_{bkg}^{\Delta E} \quad (4.11)$$

where  $\mathcal{P}_{sig}^{M_{bc}}$  and  $\mathcal{P}_{sig}^{\Delta E}$  are Gaussian and three Gaussians function.  $f_{signal}$  is fraction of signal events.  $\mathcal{P}_{bkg}^{M_{bc}}$  is primarily continuum events, and presented as Argus distribution like Eq(4.12) shows, with a preset mass threshold at  $c = 5.29 \text{ GeV}$ .

$$f(x; \chi, c) = \frac{\chi^3}{\sqrt{2\pi}\Psi(\chi)} \cdot \frac{x}{c^2} \sqrt{1 - \frac{x^2}{c^2}} \cdot \exp\left\{-\frac{1}{2}\chi^2(1 - \frac{x^2}{c^2})\right\} \quad (4.12)$$

$x$  is defined in  $0 < x < c$ .  $\chi$  and  $c$  are parameters of the distribution,  $\Psi(\chi) = \Phi(\chi) - \chi\phi(\chi) - \frac{1}{2}$  where  $\Phi(\chi)$  and  $\phi(\chi)$  cumulative distribution and probability density functions of the standard normal distribution, respectively.  $\mathcal{P}_{bkg}^{\Delta E}$  is modeled by first order Chebyshev polynomials. The shape parameters of signal events are determined by fitting to signal MC, and then fixed as constants in fitting of 2D on  $M_{bc}$  and  $\Delta E$  for generic sample and data. Fitting results on signal MC are show in Fig 4-11.

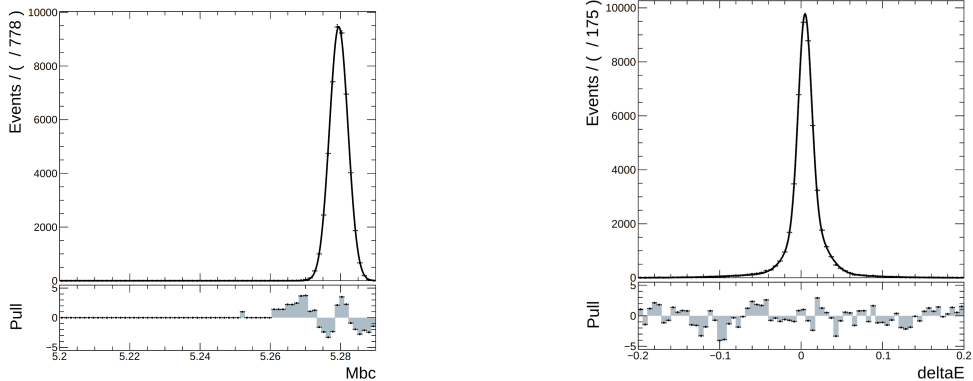


Figure 4-11: The distribution of  $M_{bc}$  and  $\Delta E$  of signal MC13 of  $B^0 \rightarrow K_S^0 K_S^0 K_S^0$  fitted with single and triple gaussian respectively.

The continuum background is fitted also first on off-resonance generic samples to determine the shapes then fix them as constants for 2D fit, shown as follows:

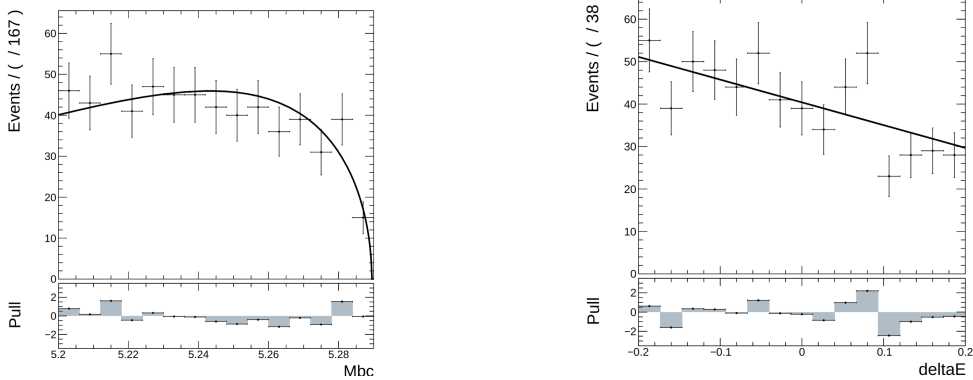


Figure 4-12: The distribution of  $M_{bc}$  and  $\Delta E$  of continuum events fitted with Argus and Chebyshev polynomial respectively.

Then we set the events number for signal and background as the only parameter in float, to use Eq(4.11) as 2D fit functions on  $1\text{ab}^{-1}$  generic sample and data, which the fit is also done using unbinned maximum likelihood fit. For  $B^0$  in generic MC sample, the 2D fit result projected on  $M_{bc}$  and  $\Delta E$  is:

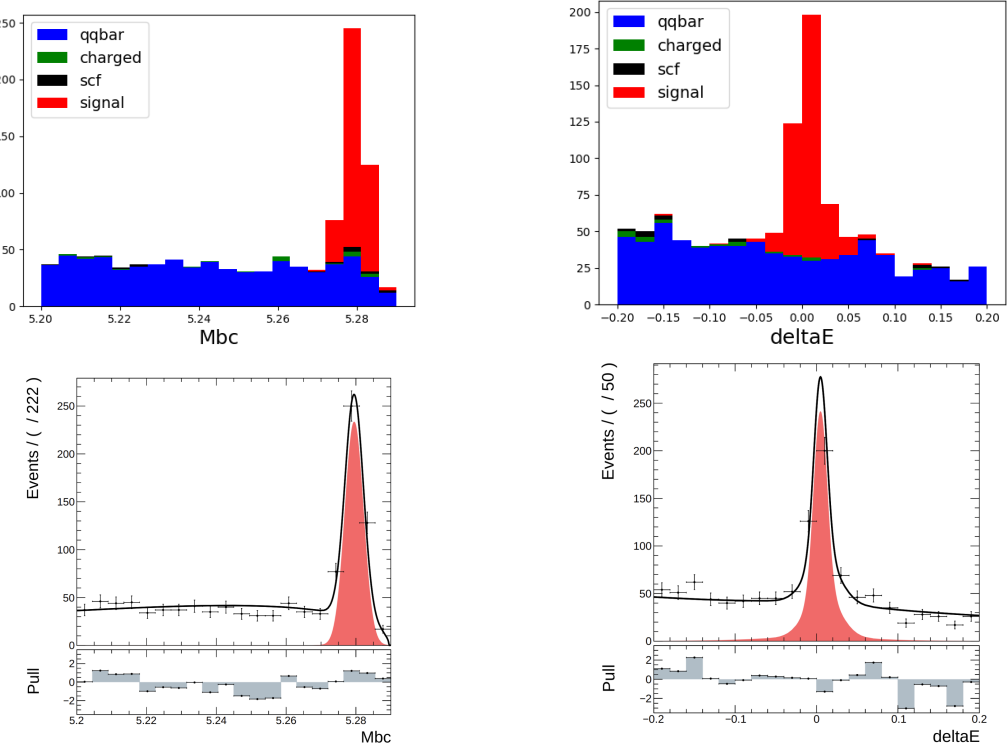


Figure 4-13: Top is the stacked plots for generic MC of  $M_{bc}$  and  $\Delta E$ , where each background components are stacked with signal. The bottom is the 2D fit on generic MC13, the red is signal PDF. The integral luminosity is  $1 \text{ ab}^{-1}$

For the invariant mass of  $K_S^0$  from  $B^0$ , we compared the distribution of “InvM” and “M” for all  $K_S^0$  that have been used for  $B^0$  reconstruction in data and generic MC. The distributions are shown in Fig 4-14 bottom, which the generic MC is scaled to the luminosity of data and agreed well. For data, the 2D fit result projected on  $M_{bc}$  and  $\Delta E$  is in Fig 4-14 top.

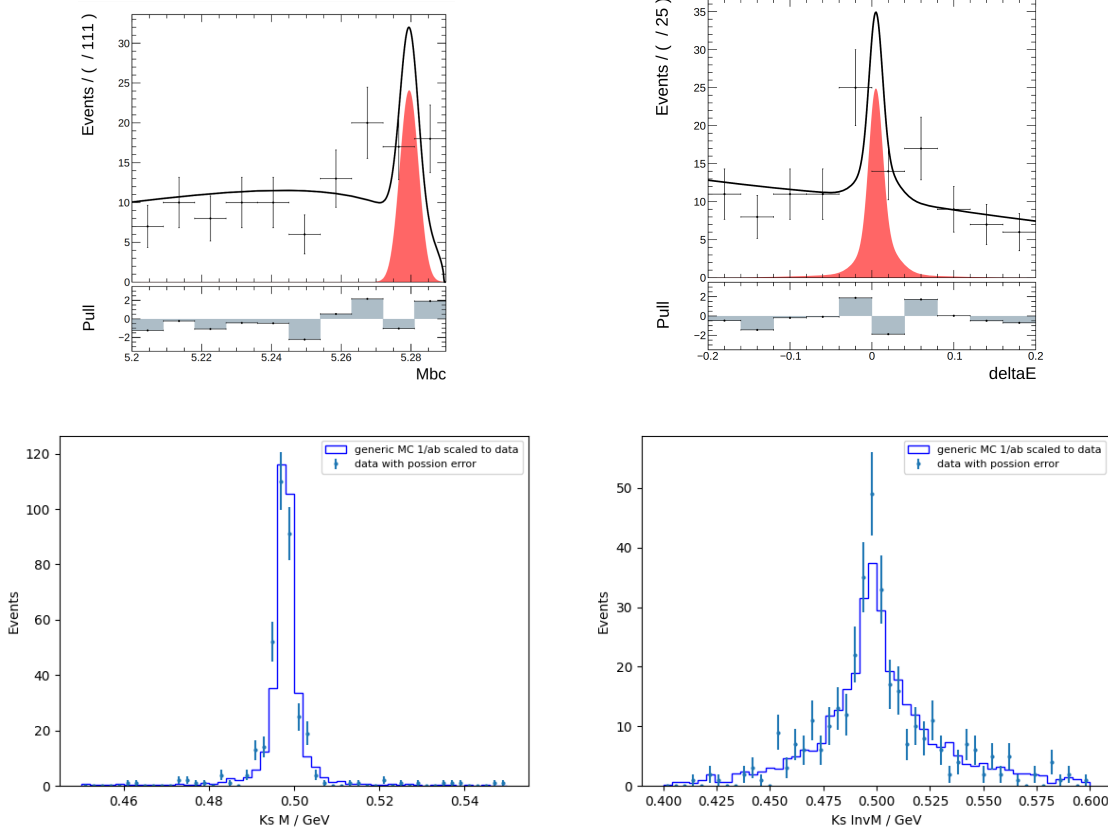


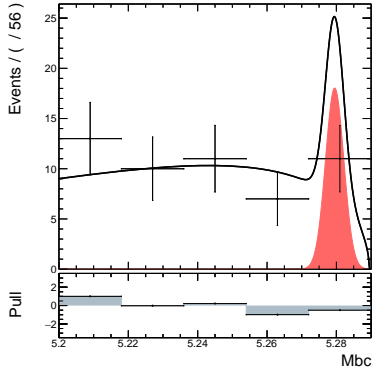
Figure 4-14: Top:  $M_{bc}$  and  $\Delta E$  2D fit using  $62.8 \text{ fb}^{-1}$  data, the red is signal PDF. Bottom: “M” and “InvM” from data and generic MC which is scaled to data luminosity. The distributions is in a reasonable consistency.

The number of signal events is extracted by integral of fit function over the signal region which is defined as  $5.27 < M_{bc} < 5.29 \text{ GeV}$  and  $-0.1 < \Delta E < 0.1 \text{ GeV}$ . The expected signal events with 35% efficiency in this analysis is calculated as:

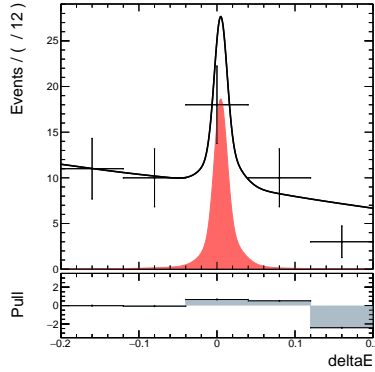
$$\mathcal{B}(B^0 \rightarrow K_S^0 K_S^0 K_S^0) = \frac{N_{sig}}{\mathcal{B}(K_S^0 \rightarrow \pi^+ \pi^-)^3 \times \epsilon_{rec} \times N_{B\bar{B}}} \quad (4.13)$$

In  $1 \text{ ab}^{-1}$  generic MC13,  $7.7 \times 10^8 \times 6 \times 10^{-6} (BR : B^0 \rightarrow 3K_S^0) \times 21\% (BR : K_S^0 \rightarrow \pi^+ \pi^-) \times 35\% \simeq 339$ . The fit result from  $M_{bc}/\Delta E$  yields  $341 \pm 20$  events which agrees with expectation. The event number in sideband  $M_{bc} < 5.26 \text{ GeV}$  in generic MC is 507. Compared to Belle result with  $772 \times 10^6 B\bar{B}$  pairs used, signal from data yields  $327 \pm 19$ , which is also consistent. In  $62.8 \text{ fb}^{-1}$  data from Belle II, we extract  $N_{sig} = 17.4 \pm 4.2$  in this region. Considering the good runs luminosity will be slightly

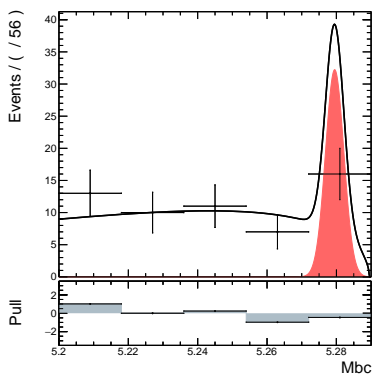
lower than the recorded, the number of signal is in a good agreement with expectation. The sideband region  $M_{bc} < 5.26$  GeV contains 60 events in data. Both the results of expected event number for signals are consistent in generic MC and data. To check linearity of the event number fitted from the  $M_{bc}$  and  $\Delta E$  in this low statistics case, we extract the fraction of continuum backgrounds from generic MC13 sample rescaled to the experimental data luminosity, which yields about 46.5 background events in  $62.8\text{fb}^{-1}$ . Then the series of (5,10,15,20,25,30) signal MC13 events is injected into the background, to perform the  $M_{bc}/\Delta E$  fit to check the output signal events number. The fitted yield from  $M_{bc}/\Delta E$  shows a good agreement on both signal and background events number in data equivalent luminosity.  $M_{bc}$  and  $\Delta E$  distribution in each injection test are shown as well. Details about the linearity of signal events are in Fig 4-16.



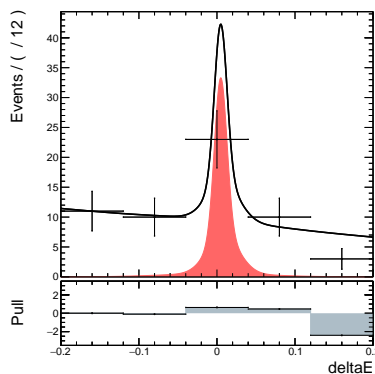
a) signal injected: 5



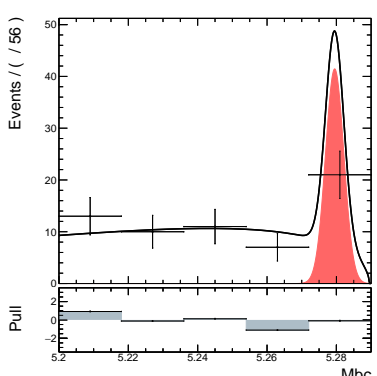
b) signal injected: 5



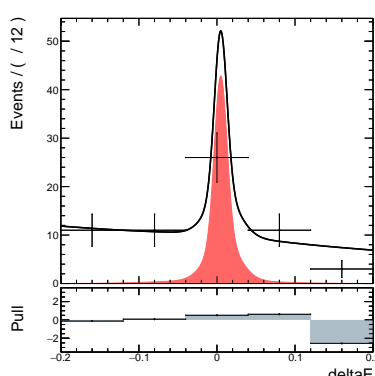
c) signal injected: 10



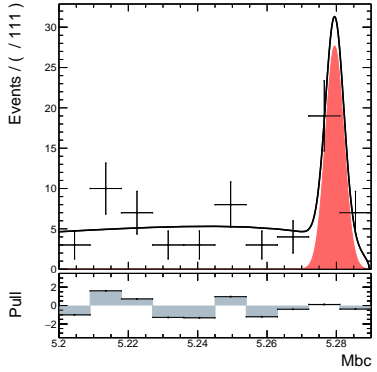
d) signal injected: 10



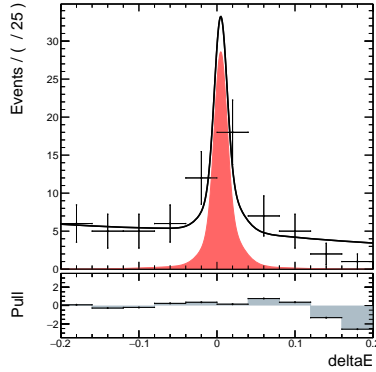
e) signal injected: 15



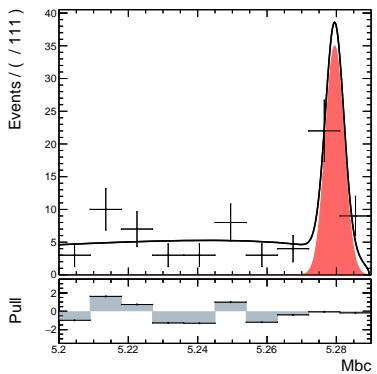
f) signal injected: 15



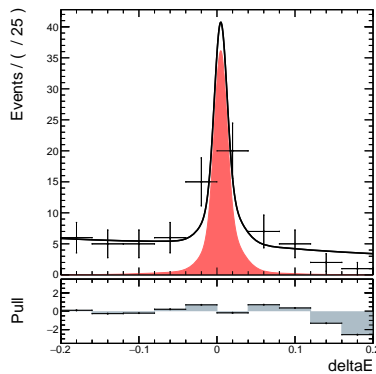
g) signal injected: 20



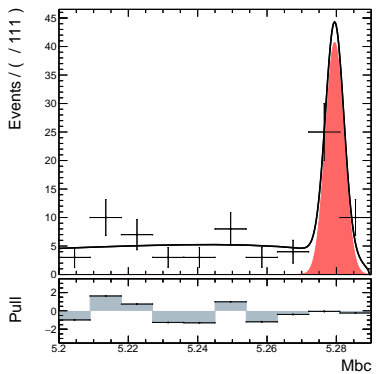
h) signal injected: 20



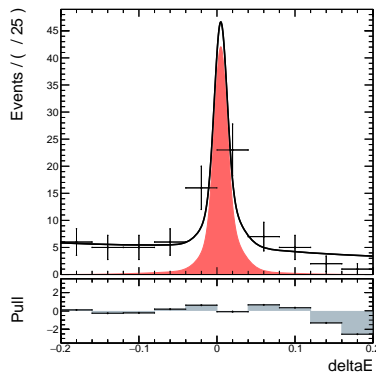
i) signal injected: 25



j) signal injected: 25



k) signal injected: 30



l) signal injected: 30

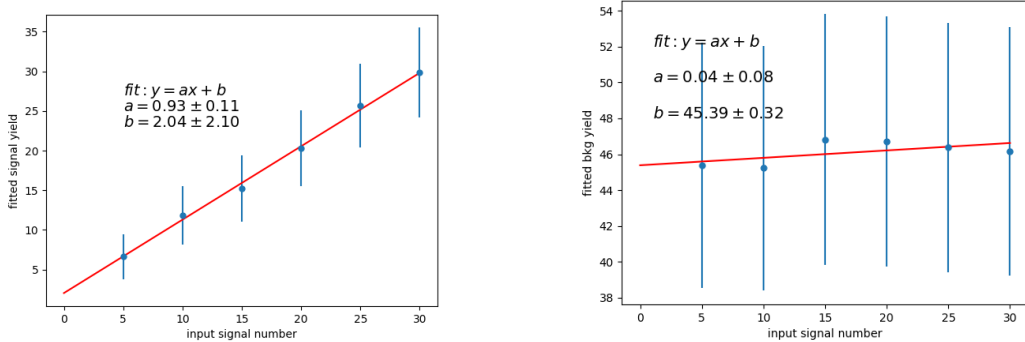


Figure 4-16: Injection test for signal extraction. The linearity is clear between input and output signal events number.

#### 4.1.7 Kinematics and Vertexing Dependence on KsFinder

KsFinder largely reduce the combinatorial background of  $B^0$ . The previous section shows a good reconstruction performance at low statistics in early phase 3 data. Without the power of rejection provided by  $K_S^0$  finder, rediscovery of  $B^0 \rightarrow K_S^0 K_S^0 K_S^0$  in early phase 3 of Belle II won't be feasible.

However, it's essential to check the potential impact on kinematics and vertexing of  $K_S^0$  regarding the implementation of KsFinder. The  $K_S^0$  classification uses information such as invariant mass and decay vertex which may propagate bias into  $B^0$  vertexing, eventually may affect  $CP$  parameters. Besides, kinematics bias might tune the shape of fit function and contribute bias in defining signal fraction used in  $CP$  fit. At last, since we have different types of  $K_S^0$  based on their SVD hit numbers, a check with  $B^0$  based on different  $K_S^0$  types are also worthy of doing.

Given each type of  $B^0$  based on how many CDC-only tracks it has in final states, the check on  $M_{bc}$  and  $\Delta E$  with or without KsFinder is done by fitting the distribution in signal.  $M_{bc}$  and  $\Delta E$  are modeled by double-Gaussian. Compared corresponding fit results, no clear bias on  $M_{bc}$  and  $\Delta E$  are found by using KsFinder or not. Results are plotted in Fig 4-17 and 4-18. The main distribution of  $M_{bc}$  and  $\Delta E$  show very trivial difference.

Similar to the comparison of  $M_{bc}$  and  $\Delta E$ , Z direction vertex position along with

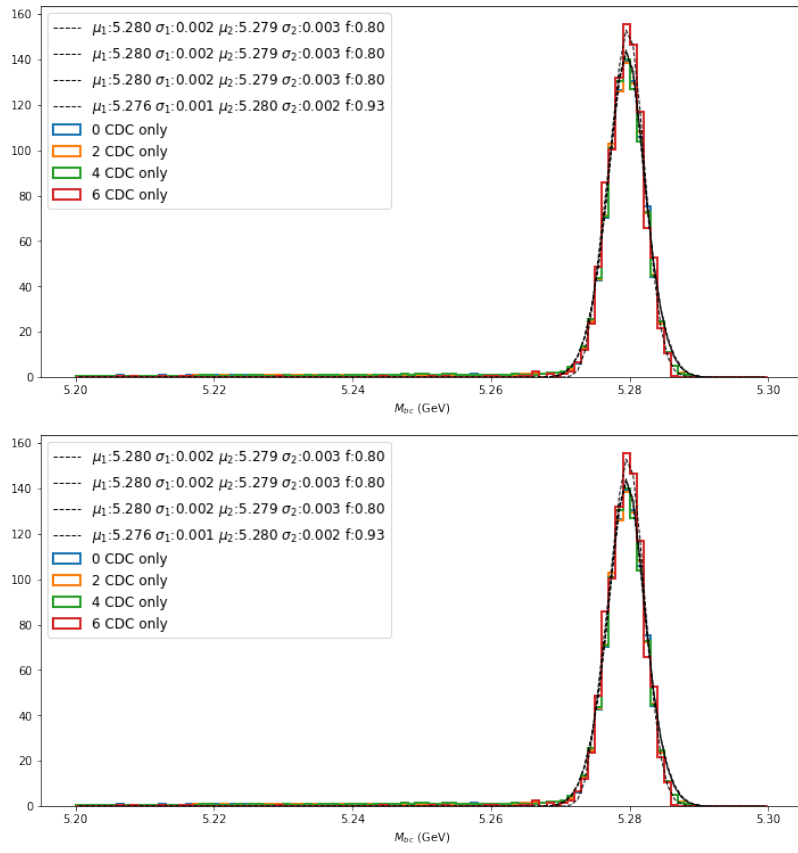


Figure 4-17:  $M_{bc}$  distribution based number of CDC-only tracks in final states. Up: no  $K_S^0$  finder; Down:  $K_S^0$  finder used. f is the fraction for the first Gaussian

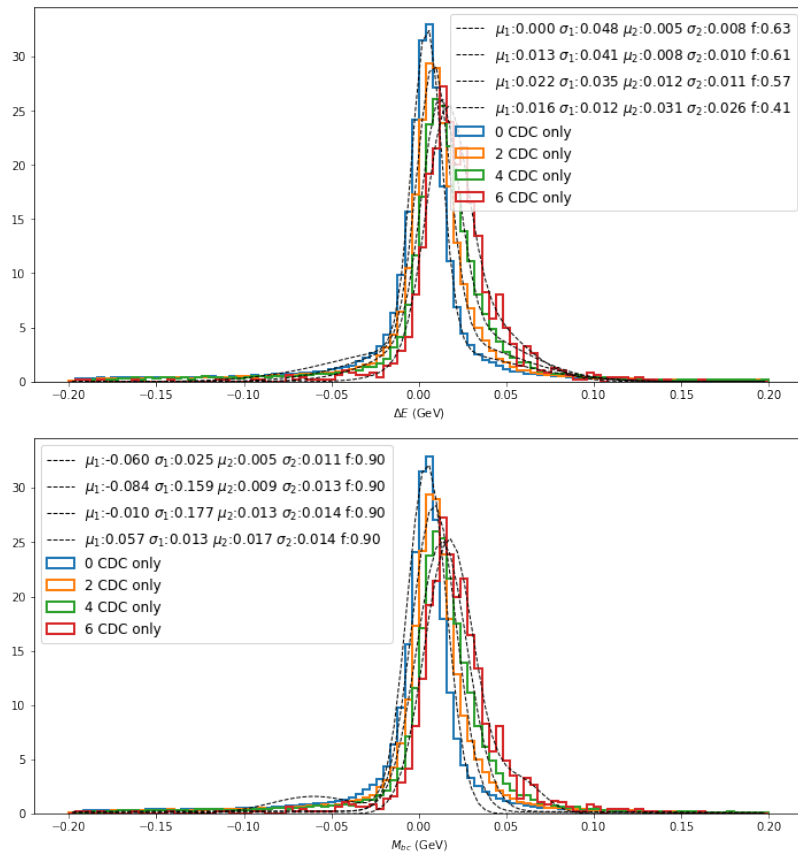


Figure 4-18:  $\Delta E$  distribution based number of CDC-only tracks in final states. Up: no  $K_S^0$  finder; Down:  $K_S^0$  finder used. f is the fraction for the first Gaussian

its uncertainties are also checked. No clear bias on vertex position and uncertainties are spotted either. Results are plotted in Fig 4.19 and 4.20. And it obvious that the resolution of vertex on z-axis is much worse when the final states of  $B^0$  only have CDC tracks.

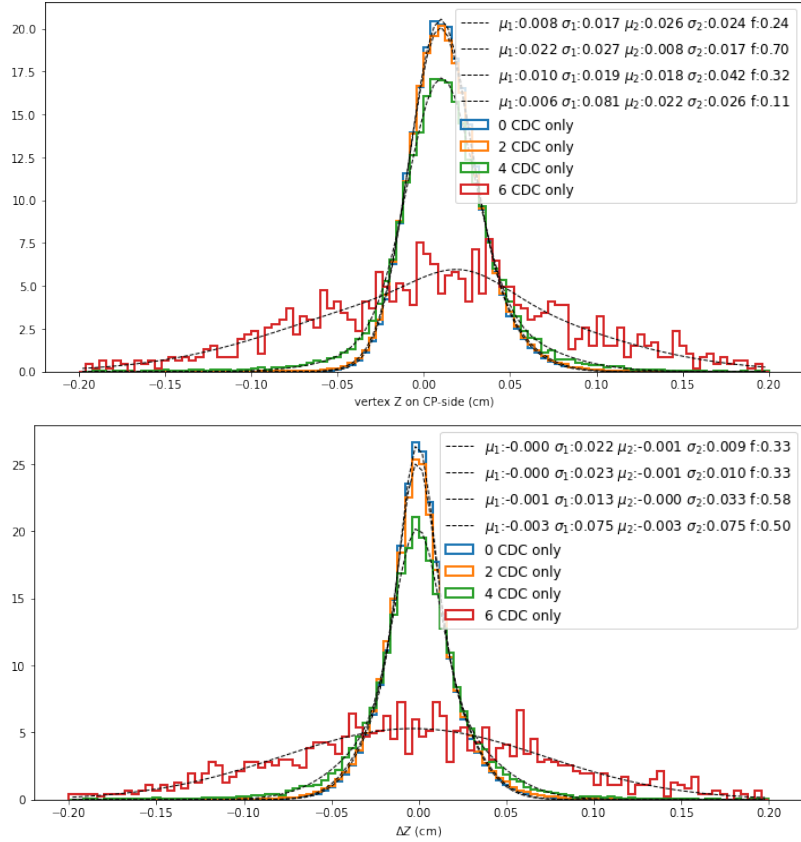


Figure 4-19:  $\Delta z$  distribution based number of CDC-only tracks in final states. Up: no  $K_S^0$  finder; Down:  $K_S^0$  finder used. f is the fraction for the first Gaussian

Above all, no clear sign of bias on both kinematics and vertex position from using  $K_S^0$  finder has been found, KsFinder implements a small shift on the vertex positions which is trivial compared to the large statistical uncertainty. For the moment, there's no correction on these variables are considered based on the neglect able difference from using KsFinder. And further effects will be watched in future improvement of KsFinder.

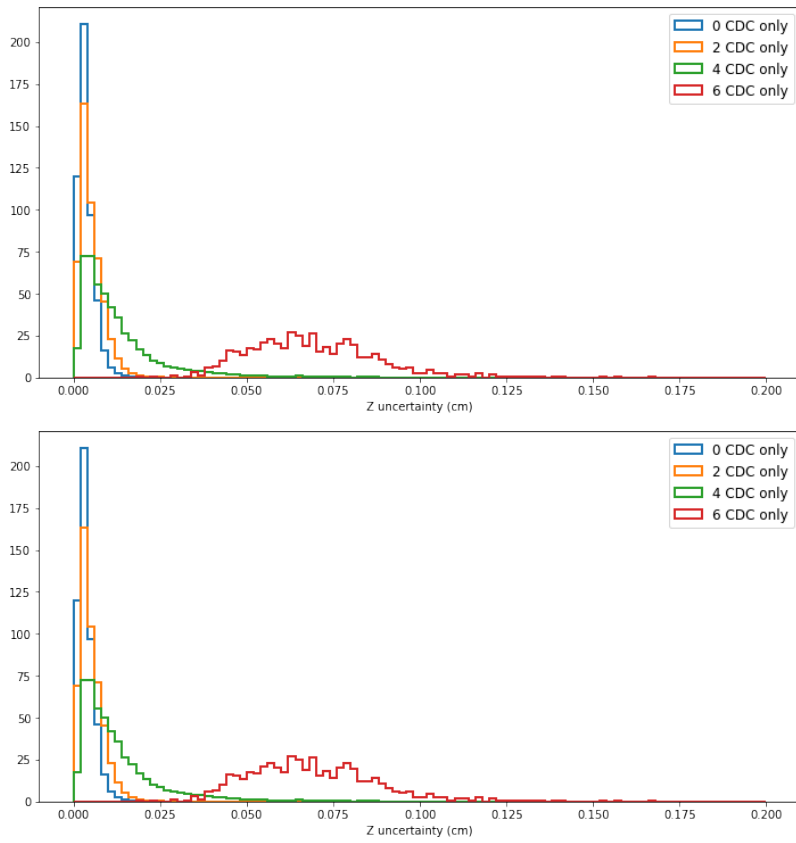


Figure 4-20:  $\delta\Delta z$  distribution based number of CDC-only tracks in final states. Up: no  $K_S^0$  finder; Down:  $K_S^0$  finder used.

#### 4.1.8 Summary

To properly reconstruct  $B^0$ , a typical cut-based loose selection of  $K_S^0$  is first done and then developed KsFinder using FastBDT classification is applied. Due to the tracking issue regarding the  $K_S^0$  daughters missing SVD hits, fit mass with varied cuts are used in addition. Combining  $K_S^0$  candidates and implementing continuum suppression from event-shape analysis yield signal  $B^0$  with relatively low background in full range. 2D fit on  $M_{bc}$  and  $\Delta E$  are performed to extract signal and background number inside defined signal box. The results are in a good agreement in data and MC, as well as Belle result. Potential data MC correction of using KsFinder has been studied. The potential bias on kinematics and vertexing are also studied, which are in a trivial level under the current luminosity.



# Chapter 5

## *CP* Parameters measurement

The measurement of *CP* parameters requires the fit to the time-dependent distribution of events based on the decay time difference, flavor, and *CP* parameters, in which  $\Delta t$  is decay time difference and  $q$  is flavor of tag-side meson.  $q = \pm 1$  when tag-side is  $B^0$  or  $\bar{B}^0$ . The physical distribution of events satisfies the function in Eq(5.1), where we use the notations that is slightly different than Chapter 1. The  $S_f$  and  $A_f$  which stand for mixing induced and direct *CP* violation that are noted as  $\mathcal{S}$  and  $\mathcal{A}$ .

$$\mathcal{P}_{sig}(\Delta t, q) = \frac{e^{-|\Delta t|/\tau_{B^0}}}{4\tau_{B^0}} \left\{ 1 + q \cdot \left[ \mathcal{S} \sin(\Delta M_d \Delta t) + \mathcal{A} \cos(\Delta M_d \Delta t) \right] \right\} \quad (5.1)$$

In above function, it's parameterized by  $\mathcal{S}$  and  $\mathcal{A}$ . A complete model that includes the overlay of background components and outlier bands can be defined as :

$$\begin{aligned} \mathcal{P}(\Delta t_i, q_i, f_i^{sig}, \mathcal{S}, \mathcal{A}) &= (1 - f_{ol}) \left[ f_{sig} \mathcal{P}_{sig}(\Delta t_i, q_i, \mathcal{S}, \mathcal{A}) + (1 - f_{sig}) \mathcal{P}_{bkg}(\Delta t_i) \right] \\ &\quad + f_{ol} \mathcal{P}_{ol}(\Delta t_i) \end{aligned} \quad (5.2)$$

where  $\mathcal{P}_{bkg}$  and  $\mathcal{P}_{ol}$  are defined by:

$$\mathcal{P}_{bkg}(\Delta t_i) = f_{bkg}^\delta \delta(\Delta t_i - \mu_{bkg}^\delta) + (1 - f_{bkg}^\delta) \frac{1}{2\tau_{bkg}} e^{-|\Delta t_i - \mu_{bkg}^{bkg}|/\tau_{bkg}} \quad (5.3)$$

$$\mathcal{P}_{ol}(\Delta t_i) = G(\Delta t_i, \sigma_{ol}) \quad (5.4)$$

$\delta(\Delta t_i - \mu_{bkg}^\delta)$  is Dirac type  $\delta$  function. Eq(5.2) is using  $\Delta t_i$  as i-th event's decay time difference  $\Delta t_i = \Delta z / \beta \gamma c$  in data set, where  $\Delta z = z_{cp} - z_{tag}$ .

## 5.1 Vertex Resolution Model

### 5.1.1 *CP*-side resolution function

Eq(5.2) presents an ideal distribution of  $\Delta t_i$  without considering the difference between measured vertex position and the physical ones. The difference can be described by introducing resolution functions. If considering resolution function, Eq(5.2) turns into:

$$\begin{aligned} \mathcal{P}(\Delta t_i, q_i, f_i^{sig}, \mathcal{S}, \mathcal{A}) = & (1 - f_{ol})[f_{sig} \mathcal{P}_{sig}(\Delta t_i) \otimes R_{sig}(\Delta t_i) \\ & + (1 - f_{sig}) \mathcal{P}_{bkg}(\Delta t_i) \otimes R_{bkg}(\Delta t_i)] \\ & + f_{ol} \mathcal{P}_{ol}(\Delta t_i) \otimes R_{ol}(\Delta t_i) \end{aligned} \quad (5.5)$$

$R_{sig}$  stands as resolution function for signal component, which receives smearing effect from *CP* and tag side, namely  $R_{cp}$  and  $R_{tag}$ . The treatment of *CP* side and tag side is different because of vertexing strategies. For *CP* side, vertex of  $B^0$  is reconstructed by fully fitting all the daughter particles. Instead, in tag side, there's no reconstruction of  $B^0$  so vertex fit is performed by geometric fitting with selected charged tracks. The background events has its own resolution model which is independent from any *CP* violation parameters. The outlier is used to compensate and smooth the long tails when  $\Delta t$  becomes very large. In this analysis, we don't include the outlier to have a more realistic model under very low statistics.

Considered only the detector effect on vertex difference along z-axis  $\Delta z$ .

$$\Delta z = \Delta z' + (z_{cp} - z'_{cp}) - (z_{tag} - z'_{tag}) \quad (5.6)$$

where the primed ones stands for physical truth of position and the non-primed is measured. Footnotes are from either  $CP$  side or tag side position. The resolution function clearly comes from  $CP$  and tag-side, so for signal events, we determine the resolution models from  $CP$  and tag-side separately. The resolutions on both sides also depends on the fitting method and the applied constraint, so to generalize the options used, there's no IP constraint from both side when the vertex is fitted, which avoids potential bias from IP profile under this low statistical situation.

$CP$ -side vertex is fitted with TreeFit as mentioned in the previous section where all tracks from a reconstructed event is used, thus the resolution models only depends on detectors' performance. For the  $CP$ -side vertex from TreeFit, the vertex resolution has relation towards the reconstruction quality, or to be more specific, the  $\chi_2/N$  value, which  $\chi_2$  represents the goodness of fit and  $N$  is the fitting's degree of freedom. The distribution of  $\chi_2/N$  (called as reduced  $\chi_2$ ) in selected events are shown below:

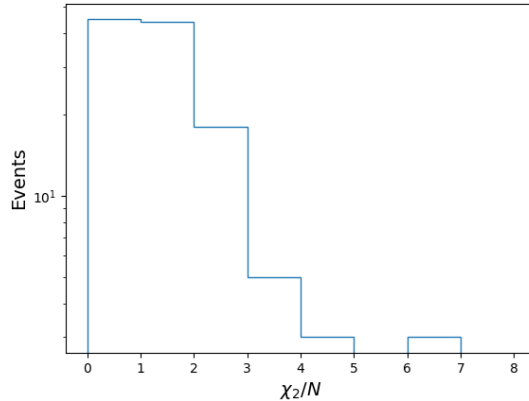


Figure 5-1:  $\chi_2/N$  of selected events from data.

Based on this, we model the resolution functions on  $CP$ -side vertexing using a double-gaussian function, whose mean is set to zero and the standard deviation is scaled by  $\chi_2/N$  and the error of vertexing.

$$R_{cp}(\delta z_{cp}) = (1 - f_{cp}^{tail})G(0, s_{cp}^{main}) + f_{cp}^{tail}G(0, s_{cp}^{tail}) \quad (5.7)$$

where:

$$\begin{aligned}s_{cp}^{main} &= (s_0^{main} + s_1^{main} \cdot \chi_{cp}^2 / NDF) \cdot \sigma_{z_{cp}} \\ s_{cp}^{tail} &= (s_0^{tail} + s_1^{tail} \cdot \chi_{cp}^2 / NDF) \cdot \sigma_{z_{cp}}\end{aligned}\tag{5.8}$$

The dependence of resolution models on  $\chi_2/N$  is shown as follows. Restrictively speaking, the  $CP$ -side resolution for  $B^0 \rightarrow K_S^0 K_S^0 K_S^0$  is slight different from other channels such as  $B^0 \rightarrow J/\psi K_S^0$ , due to the lack of the direct charged tracks from the  $B^0$  vertex. The way of scaling the resolution will be further studied along with more data available. Given the current low statistics, the above model works well as an approximation. By fitting the resolution functions from signal MC on  $CP$ -side, we could determine the parameters in Eq(5.7), and it's listed in Table 5.1.

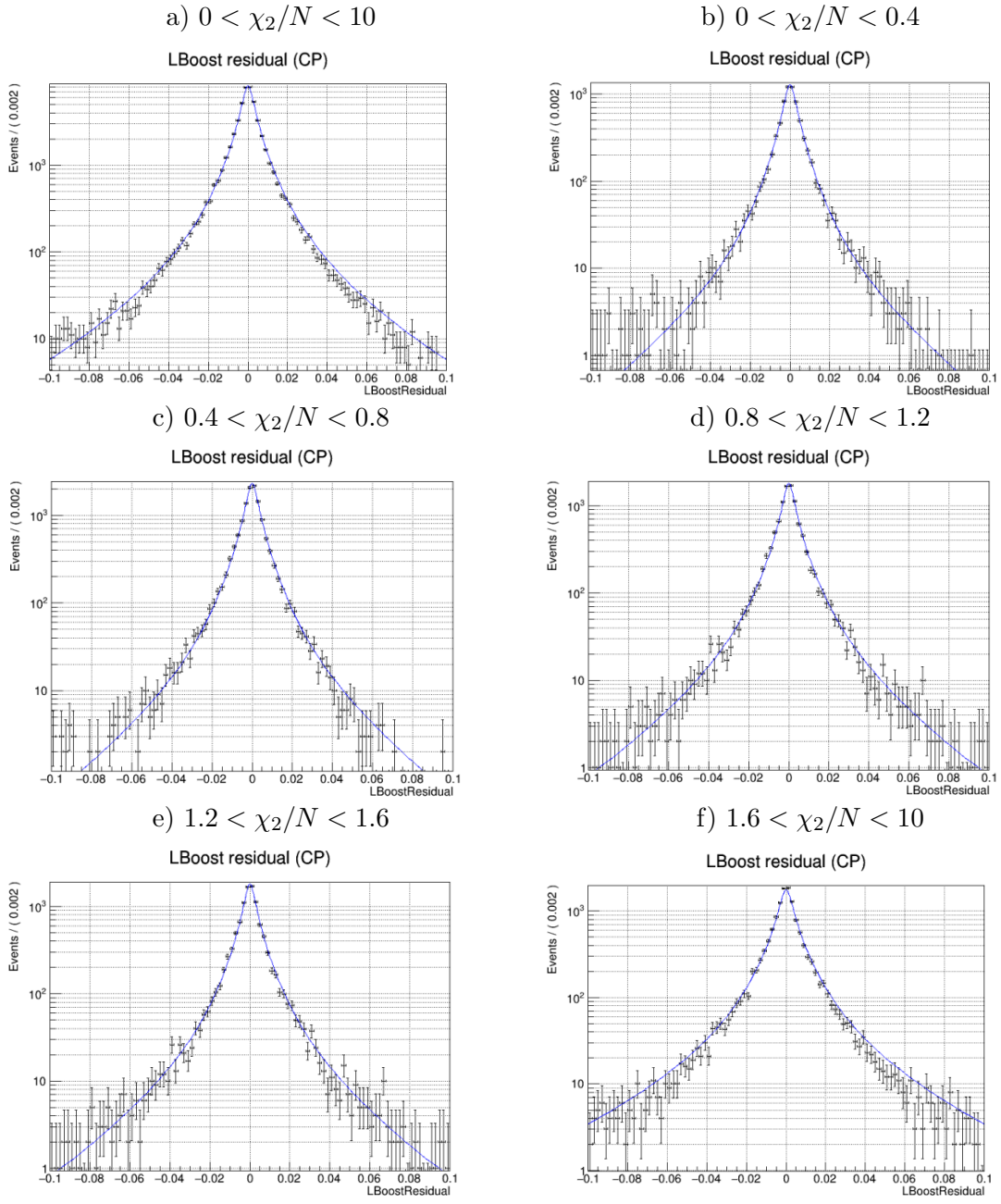


Figure 5-2: Resolution functions on *CP*-side, which shows dependence on the  $\chi_2/N$

Table 5.1: Parameters in  $R_{cp}$ .

$f_{cp}^{tail}$	$0.07424 \pm 0.0008$
$s_0^{main}$	$0.9151 \pm 0.0077$
$s_1^{main}$	$0.2142 \pm 0.0064$
$s_0^{tail}$	$2.0477 \pm 0.0779$
$s_1^{tail}$	$1.3470 \pm 0.0720$

### 5.1.2 Tag-side resolution function

For the tag-side, the vertexing is done by using KFit and No IP constraint. Since we don't reconstruct certain decay channel like  $CP$ -side, there's no guarantee that tracks used by KFit are all from the primary vertex. This leads to the resolution degradation on tag side vertexing called  $R_{np}$ . To the contrary, if all tracks that are used for tag vertexing are from primary vertex, then resolution will only be affected by the detector, and this is called  $R_{det}$ , similarly to  $R_{cp}$ . The model is demonstrated as below:

$$\begin{aligned} z_{tag} - z'_{tag} &= z'_{tag} + \delta z_{tag}^{det} + \delta z_{tag}^{np} - z'_{tag} \\ &= \delta z_{tag}^{det} + \delta z_{tag}^{np} \end{aligned} \quad (5.9)$$

$$R_{tag}(z_{tag} - z'_{tag}) = R_{det}^{tag}(\delta z_{tag}^{det}) \otimes R_{np}^{tag}(\delta z_{tag}^{np}) \quad (5.10)$$

$$R_{det}^{tag}(\delta z_{tag}^{det}) = (1 - f_{tag}^{tail})G(0, s_{tag}^{main} \cdot \sigma_{z_{tag}}) + f_{tag}^{tail}G(0, s_{tag}^{tail} \cdot \sigma_{z_{tag}}) \quad (5.11)$$

where main and tail parts share same main value at zero, but deviation is defined by using uncertainties in each event  $\chi^2_{tag}/N$ :

$$s_{tag}^{main/tail} = s_0^{main/tail} + s_1^{main/tail} \cdot \chi^2_{tag}/NDF \quad (5.12)$$

where  $\chi^2_{tag}/N$  is returned by tag side vertexing tool on event-by-event basis. Technically  $R_{det}^{tag}$  can be fitted with MC of which tag side tracks are all from primary vertex. Then after fixing the fitted parameters of  $R_{det}^{tag}$ ,  $R^{tag}$  will only be dependent on  $R_{np}^{tag}$ .

As for the fit of  $R_{np}$ , similar event-by-event fit is also implemented. The fit model of  $R_{np}$  is inherited Belle experience. It consists of three functions, including one Dirac type  $\delta$  function and two single side exponential.

$$R_{tag}^{np}(\delta z_{tag}^{np}) = f_\delta \delta(\delta z_{tag}^{np}) + (1 - f_\delta)[f_p E_p(\delta z_{tag}^{np}, \tau_p \cdot \sigma_{z_{tag}}) + (1 - f_p) E_n(\delta z_{tag}^{np}, \tau_n \cdot \sigma_{z_{tag}})] \quad (5.13)$$

where  $E_p(x, \tau_p) = (1/\tau_p) \exp(-x/\tau_p)$  when  $x > 0$  and  $E_n(x, \tau_n) = (1/\tau_n) \exp(x/\tau_n)$  when  $x < 0$ .

Also, since tag-side has no dependence of how  $CP$ -side decays, its resolution is almost mode-independent. We use the parameters that is obtained by fitting to the control sample data. The details about control sample study are here[31]. The fit results for tag-side resolution is shown in Fig 5-3 and 5-4 and Table 5.3 and Table 5.4.

Table 5.2: Parameters in  $R_{cp}$ .

$f_{cp}^{tail}$	$0.07424 \pm 0.0008$
$s_0^{main}$	$0.9151 \pm 0.0077$
$s_1^{main}$	$0.2142 \pm 0.0064$
$s_0^{tail}$	$2.0477 \pm 0.0779$
$s_1^{tail}$	$1.3470 \pm 0.0720$

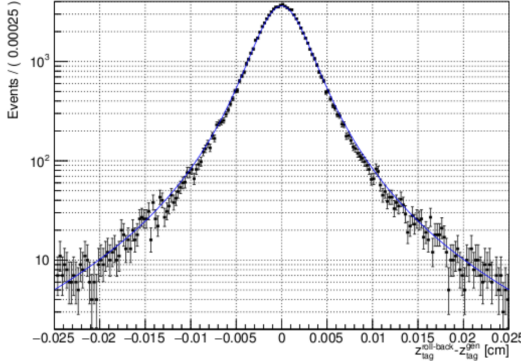


Figure 5-3:  $R_{det}^{tag}$  fit

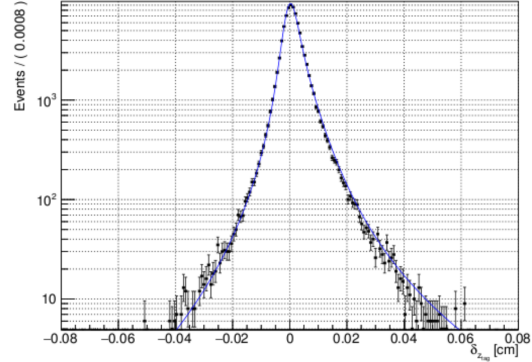


Figure 5-4:  $R_{np}^{tag}$  fit

Table 5.3: Parameters in  $R_{det}^{tag}$

$f_{tag}^{tail}$	$0.0523 \pm 0.0025$
$s_0^{main}$	$1.1446 \pm 0.0061$
$s_1^{main}$	$0.0443 \pm 0.0022$
$s_0^{tail}$	$3.4480 \pm 0.0897$
$s_1^{tail}$	$0.2666 \pm 0.0276$

Table 5.4: Parameters in  $R_{np}^{tag}$

$f_\delta$	$0.6256 \pm 0.0049$
$f_p$	$0.8316 \pm 0.0051$
$\tau_n$	$2.9141 \pm 0.0758$
$\tau_p$	$2.4846 \pm 0.0269$

Last but not least, the boost direction of each event is not constant event-by-event, so the z-axis position of vertex may not be optimized by calculating  $\Delta t_i = \Delta z / \beta \gamma c$ . This effect can be reduced by replacing z position with the relative distance along the boosting direction, or introducing another resolution function called  $R_k$ . In the current modeling of Belle II tag side resolution, distance along the boost direction is available so  $R_k$  is not yet implemented. So we use the  $\Delta Z$  projection on the boosted direction of each event to account for this effect when we define the parameters of resolution and also for the final fit to Eq(5.5).

### 5.1.3 Background events distribution

Instead,  $R_{bkg}$  is in a simpler shape and it's uncorrelated to vertexing method approximately. Because the source of background mainly comes from continuum events passing the selection, it's reasonable to model its resolution by Gaussian-like func-

tion. We define a double-Gaussian with its standard deviation scaled by the measured uncertainties from both sides as Eq(5.14) shows.

$$R_{bkg} = (1 - f_{tail}^{bkg})G(\Delta t_i, \sigma_{main}^{bkg}\sqrt{\sigma_{cp}^2 + \sigma_{tag}^2}) + f_{tail}^{bkg}G(\Delta t_i, \sigma_{tail}^{bkg}\sqrt{\sigma_{cp}^2 + \sigma_{tag}^2}) \quad (5.14)$$

It convolution integrals with  $\mathcal{P}_{bkg}$ :

$$\mathcal{P}_{bkg} = f_\delta^{bkg}\delta(\Delta t - \mu_\delta^{bkg}) + (1 - f_\delta^{bkg})\frac{1}{2\tau_{bkg}}e^{-|\Delta t - \mu_\delta^{bkg}|/\tau_{bkg}} \quad (5.15)$$

With this definition, one can make background component  $\mathcal{P}_{bkg} \circledast R_{bkg}$  and fit to side-band data to obtained the parameters. There are total seven parameters in float to determine which are listed down below with primary fit results on sideband data, which according to the previous section, is totally 60 events in  $M_{bc} < 5.26$  GeV.

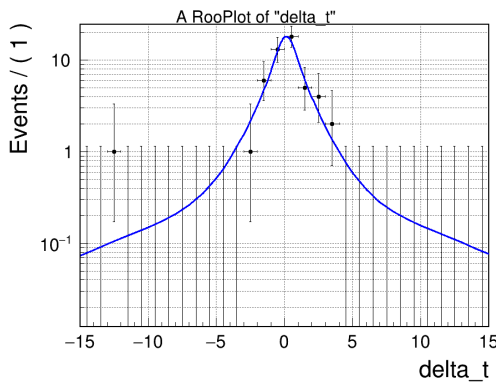


Figure 5-5: Background fit on data sideband with  $M_{bc} < 5.26$  GeV

$\mu_{\delta}^{bkg}$	$0.1310 \pm 0.1902$
$\mu_l^{bkg}$	$0.1638 \pm 0.5030$
$\tau_{bkg}$	$1.0541 \pm 0.4370$
$f_{\delta}^{bkg}$	$0.5861 \pm 0.2570$
$f_{tail}^{bkg}$	$0.0417 \pm 0.0408$
$\sigma_{main}^{bkg}$	$1.4348 \pm 0.3940$
$\sigma_{tail}^{bkg}$	$28.0930 \pm 8.8221$

Table 5.5: Parameters in Background  $\Delta t$  distribution.

## 5.2 Flavor Tagging

In order to determine the flavor of tag side  $B^0$ , flavor tagging algorithm is being developed. The tagger uses information from  $\mu^\pm, \pi^\pm, K^\pm$  and  $\Lambda$  and categorized them into 13 different types as illustrated below.

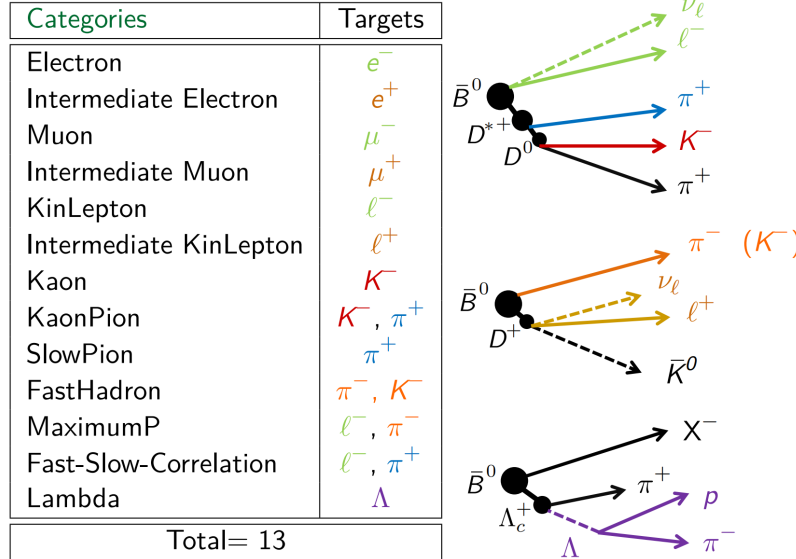


Figure 5-6: Particles and their categories used in flavor tagging algorithm.

For each particle that has been used from above categories, PID and kinematics (such as  $p_t, \cos\theta, d_0$ , etc) information are extracted and feed to the combiner as training variables, to form a output corresponding each category. Then for all outputs from

these categories, a total classifier is trained to present the likelihood of flavor  $q$ . This algorithm is called category-based algorithm which is used in our analysis. Similar tagger based on deep neural-network algorithm is also available but will not be further discussed here. After the reconstruction on the  $CP$  side is done, ROE objects that contains the tracks from tag side is formed, and tracks that will be used to fill the above particle lists are selected. Just like  $K_S^0$  finder and continuum suppression, we choose FastBDT as classifier back-end algorithm. Targeted variable is  $q$  of tag side in MC truth. The ROE selection is affected by the cleanliness of  $CP$  reconstruction, but flavor tagging should be almost mode-independent. To minimize impact of the reconstruction performance, MC sample of  $B^0 \rightarrow \nu\nu$  is used for training the tagger where  $CP$  side is completely invisible. Then the trained classifier can be applied to signal sample.

The statistical uncertainty of  $\mathcal{S}$  now receives contribution from  $\epsilon$  and  $w$ :  $\delta(\mathcal{S}) \propto \frac{1}{\epsilon(1-2w)N_{rec}}$ , which make it crucial to correctly measure tagging efficiency and wrong tag fraction.  $w$  can be estimate using MC sample which the bias on individual events could propagate to the fit of  $\mathcal{S}$ . By measuring  $w$  from flavor specific decay using real data, bias from MC can be avoid. The validation of flavor tagger using flavor specific control sample is summarized here: [32]. For flavor specific decay, the Eq(5.17) and Eq(5.18) could be used to fit the wrong tagging fraction and efficiency.

$$\mathcal{P}_{SF/OF}^{obs}(\Delta t, q_{cp}, q_{tag}, \epsilon, w) = \frac{e^{-|\Delta t|/\tau_{B^0}}}{4\tau_{B^0}} \epsilon \left[ 1 + q_{cp} \cdot q_{tag} (1 - 2w) \cdot \cos(\Delta M_d \Delta t) \right] \quad (5.16)$$

so wrong tag fraction can be measured by:

$$\frac{\mathcal{P}_{OF}^{obs} - \mathcal{P}_{SF}^{obs}}{\mathcal{P}_{OF}^{obs} + \mathcal{P}_{SF}^{obs}} = (1 - 2w) \cos(\Delta M_d \Delta t) \quad (5.17)$$

If  $w$  is extracted from MC, which is what we implemented in this analysis, bias could be reduced by using binned values of tagger output. To be more specific, saying the output of tagging classifier is  $\alpha$  in range  $[0, 1]$ , wrong tag probability of being  $q = +1$  is defined as  $\beta = 1 - \alpha$ , and flavor tagger will eventually gives tagged

flavor as  $\mathcal{F} = 1 - 2\beta = 2\alpha - 1$ . It's obvious that  $\mathcal{F} < 0$  means the tagged flavor is  $q = -1$  instead of  $+1$ . The distribution of  $\mathcal{F}$  is shown in Fig 5-7 (up) from signal MC. The average efficiency of among all tag-able event is measured to be  $99.92 \pm 0.01\%$ , and effective efficiency (percentage of correctly tagged events) is  $31.31 \pm 0.52\%$  for  $B^0$  and  $31.13 \pm 0.51\%$  for  $\overline{B^0}$ . No clear bias on effective tagging efficiency is found considering the MC fraction of  $B^0$  and  $\overline{B^0}$  are 50.11% and 48.89% respectively.

The r-bins are intervals that splits the absolute value of  $\mathcal{F}$ , namely  $r_{FBDT} = |\mathcal{F}|$ , where the true flavor  $q$  is irrelevant to r-bins. Belle experience on defining the r-bins is inherited where bins are set as  $[0, 0.1, 0.25, 0.5, 0.625, 0.75, 0.875, 1]$ . For all MC events that have been successful tagged, they are projected into histogram of  $|\mathcal{F}|$ ,  $w$  can be calculated in each bin in the way dividing the number of events that its  $\mathcal{F}$  is opposite to its MC flavor to all the events in the same bin. The binned tagging efficiency is calculated through dividing the number of successfully tagged events by all events in the same bin.

Besides,  $w$  can be different between  $B^0$  and  $\overline{B^0}$ . Considering  $w = (w_{B^0} + w_{\overline{B^0}})/2$  and  $\Delta w = w_{B^0} - w_{\overline{B^0}}$ , so for each event of flavor  $q$ , it may from a correct or incorrect tagged event when we look at the distribution of Eq(5.1).

From Eq(5.1), it's obvious that the distribution of  $\Delta t$  is independent from the flavor  $q$ , while this is not true considering the limit power of flavor tagging as we discussed. Only certain fraction of events can be flavor tagged and also only part of events are correctly tagged. Considering the effect from flavor tagging, the observed distribution of  $\Delta t$  is turning into:

$$\mathcal{P}_{sig}^{obs}(\Delta t, q, \epsilon, w) = \frac{e^{-|\Delta t|/\tau_{B^0}}}{4\tau_{B^0}} \epsilon \left\{ 1 - q \cdot \Delta w + q(1 - 2w) \cdot [\mathcal{S} \sin(\Delta M_d \Delta t) + \mathcal{A} \cos(\Delta M_d \Delta t)] \right\} \quad (5.18)$$

compared to the original, the fluctuation is reduced by factor  $r \equiv |1 - 2w|$ , called as dilution factor.

As for efficiency  $\epsilon$ , the difference  $\mu = \epsilon_{B^0} - \epsilon_{\overline{B^0}}$  is about 1% to 2% in each bin, thus treated as zero. The average  $r$  is also calculated in r-bins. Fig 5-7 (down) shows

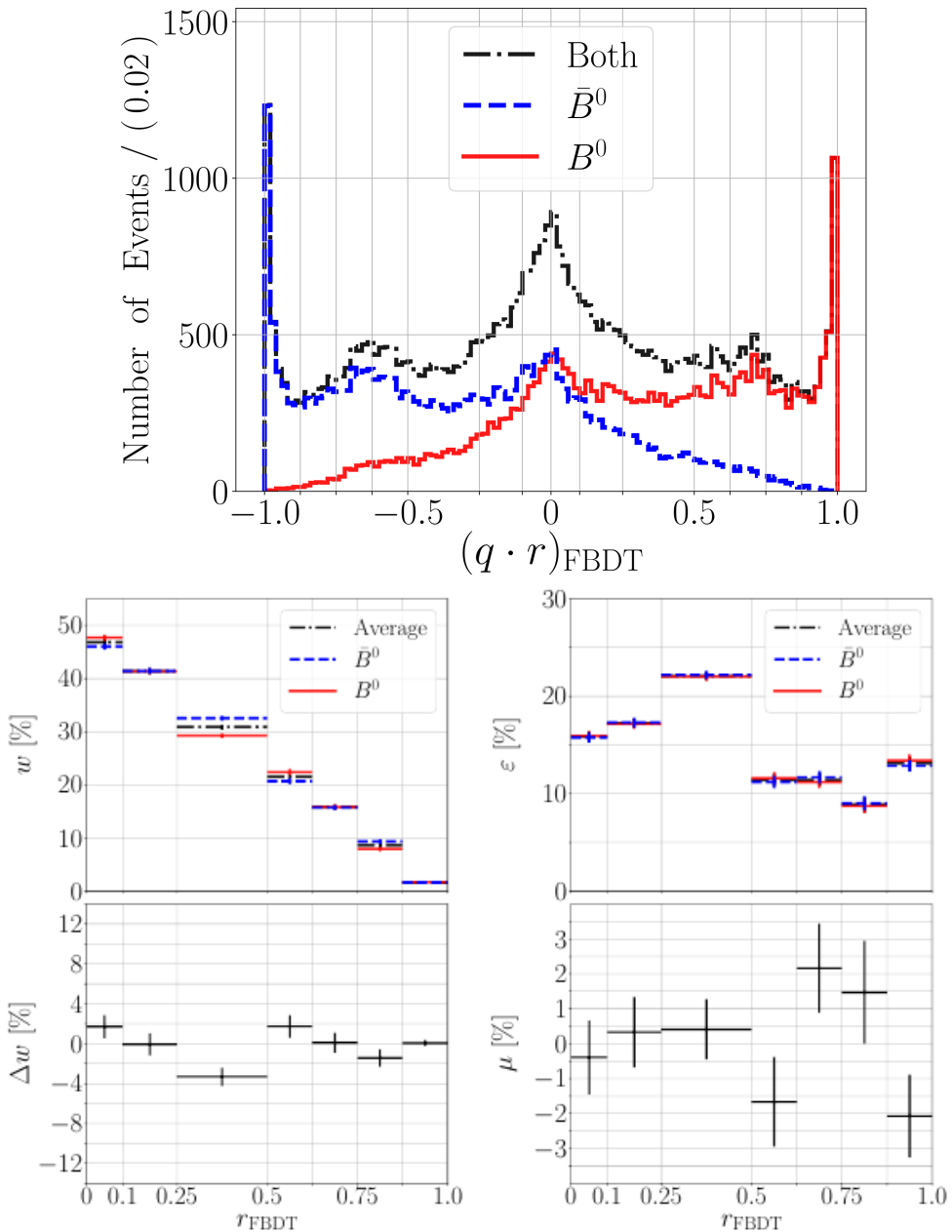


Figure 5-7: Top:the distribution of flavor tagger output  $\mathcal{F} = (q \cdot r)_{FBDT}$  for both tag side of  $B^0$  and  $\bar{B}^0$ . Bottom: flavor tagging efficiency, wrong tagging fraction, tagging difference in regard to rbin.

the flavor tagging results on  $w, \Delta w, \epsilon$  and  $\mu$  in each of the r-bin.

### 5.3 $CP$ Fitter

The parameters that are needed for  $CP$  fit is basically all studied and obtainable for extracting  $\mathcal{S}$  and  $\mathcal{A}$  from Eq(5.2) with using observed  $\Delta t$  distribution. The fit is taking the  $\Delta t$ , signal fraction  $f_{sig}$ , the flavor charge  $q$  as observables, and in the meantime the vertexing error and  $\chi_2/N$  are used as event-by-event conditional variables. RooFit is configured based on this setup and unbinned maximum likelihood fit is used as the fitting strategy. To actually perform the fit, the computation work load is an important factor to consider when the event number goes high in future. Especially, the multiple convolution integrals of resolution model and probability density functions are a set of computing intensive works. Belle legacy fitter utilize a highly customized library called “Tatami” to perform the convolution integrals. For Belle II, a new  $CP$  fitter is developed based on Python (version 3.7) and RooFit, which is naturally easy to use and maintain with BASF2 due to BASF2’s analysis controls are mostly done by Python. The code management shows a modern, good consistency and readability, which will be aimed for providing a universal fitting tool to TDCPV analysis in Belle II. The fitter requires a configuration files which contains all the observables and parameters definition including their range, value, floating state. Data that is fed to the fitter will be converted into the RooDataSet object associated with each variables from configuration file. The models of fit such as each resolution functions, signal and background P.D.F is formed with the data set in the same workspace. The convolution of each components are handled by a customized shared object written in C++ from “SignalPdf.cxx”. Combined these tools, the unbinned maximum likelihood fit is performed that can either be used to determine  $\mathcal{S}$  and  $\mathcal{A}$  or other parameters when they are floating. The result of the fit then restore as ROOT files as well as corresponding plots.

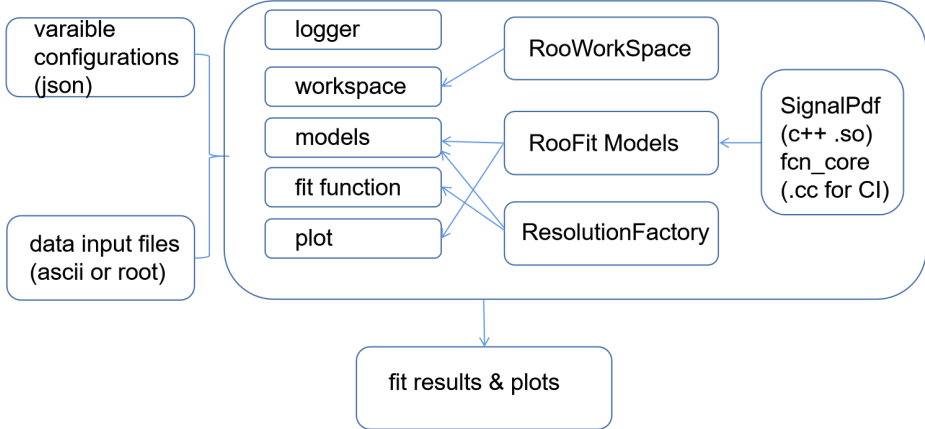


Figure 5-8: The structure of *CP* fitter for Belle II. Users provide configuration file containing the definitions of all parameters and observables in the *CP* fit. Data input files are used to create dataset for fitting. External library called “SignalPdf.cxx” are generated in runtime to calculate the integral of resolutions and physics distribution event by event, which the fit is performed by maximizing the “fcn\_core” function, presenting the likelihood of the dataset to the fit model.

## 5.4 Blind Fit

As a required procedure to make sure the *CP* parameters are measured without bias due to the preconceived results, a blind analysis procedure is conducted before the fit is actually performed using the experimental data. The blind fit procedure includes the *CP* fit on signal MC and generic MC, with different number of events used. To check the reliability of fit result from *CP* fitter, a linearity test and toy MC study is also performed.

### 5.4.1 *CP* fit on MC samples

Using *CP* fitter, we perform the *CP* fit on events in signal MC and generic MC. The signal and generic MC are generated with phase-space model which contains zero *CP* violation ( $\mathcal{S} = \mathcal{A} = 0$ ) in  $B^0 \rightarrow K_S^0 K_S^0 K_S^0$  channel. The event with following cuts are selected for *CP* fit.

- $-70 < \Delta t < 70$  ps

- $0 < (\chi_2/N)_{cp} < 8$
- $0 < (\chi_2/N)_{tag} < 50$
- error on tag-side vertex  $< 0.1$  cm
- $5.27 < M_{bc} < 5.29$  GeV and  $|\Delta E| < 0.1$  GeV

We have 10000 (8873 passing selection) events from signal sample and 415 (373 passing selection) events from  $1\text{ab}^{-1}$  generic sample to fit  $CP$  parameters. To mimic the events number expected in data sample, we randomly take 30 events from generic sample and perform the fit as well. The fit results are shown in Fig 5-9 to Fig 5-11.

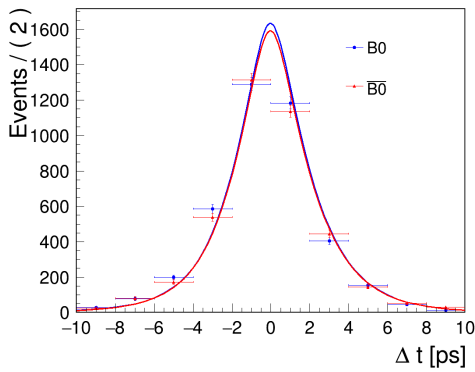


Figure 5-9:  $CP$  fit on 8873 signal MC.

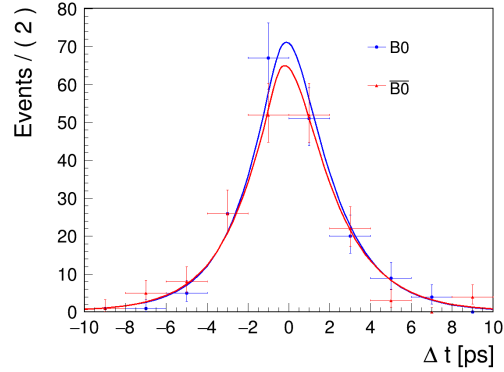


Figure 5-10:  $CP$  fit on 373 generic MC.

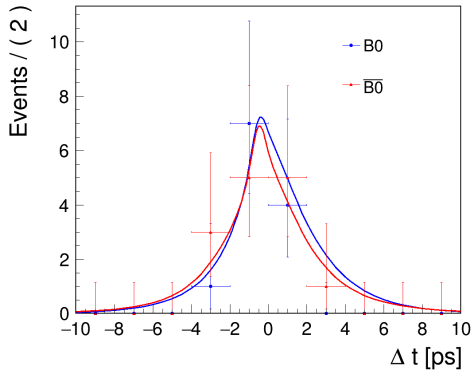


Figure 5-11:  $CP$  fit on 30 generic MC.

The fit result for 8873 signal MC is:

$$\begin{aligned} \sin(2\phi_1) &= 0.00 \pm 0.04 \\ \mathcal{A} &= -0.01 \pm 0.02 \end{aligned} \tag{5.19}$$

the fit result for 373 generic MC is:

$$\begin{aligned} \sin(2\phi_1) &= 0.00 \pm 0.21 \\ \mathcal{A} &= -0.05 \pm 0.07 \end{aligned} \tag{5.20}$$

the fit result for 30 events generic MC is:

$$\begin{aligned} \sin(2\phi_1) &= 0.20 \pm 0.85 \\ \mathcal{A} &= -0.06 \pm 0.30 \end{aligned} \tag{5.21}$$

The fit results are consistent with expectation in non- $CP$  violation from MC input, and the statistical uncertainties has the tendency  $\delta \propto 1/\sqrt{N}$  as poission distribution. To test fit on non-zero  $CP$  violating MC, the fit on  $B^0 \rightarrow J/\psi K_S^0$  signal MC is also done, the details of events selection as well as fit model determination can be found[31]. The fit result over 10000 events is shown in FIG.30, which results in  $\sin(2\phi_1) = 0.70 \pm 0.05$  and  $\mathcal{A} = -0.01 \pm 0.02$ . The results agree with the input.

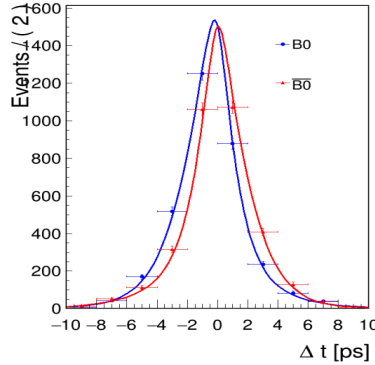


Figure 5-12:  $CP$  fit over 10000  $B^0 \rightarrow J/\psi K_S^0$  signal MC.

#### 5.4.2 Linearity Test

To validate the  $CP$  fit linearity, we generate a series of toy MC sample, which the  $\chi_2$ ,  $N$  and vertex errors on  $CP$  and tag-side are sampled from distribution of signal MC. The resolution functions parameters are kept same as MC fit as previous section. The input  $\mathcal{A}$  is set to zero while the input value of  $\sin(2\phi_1)$  is running from 0.1 to 0.9.

Each dataset contains 10000 events. The dependence between input and output are shown below. The linearity fit shows a good agreement between input and output.

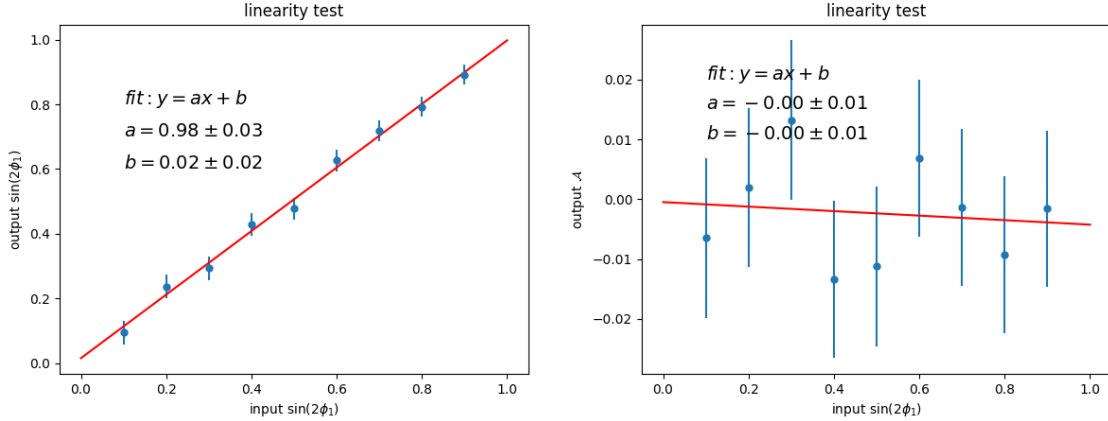


Figure 5-13: Linearity test of  $CP$  fit.

Also, we fix  $\sin(2\phi_1)$  at zero while floating  $\mathcal{A}$  from 0.1 to 0.9, the dependence between input and output are as Fig 5-14 shows. The linearity fit shows a good agreement as well.

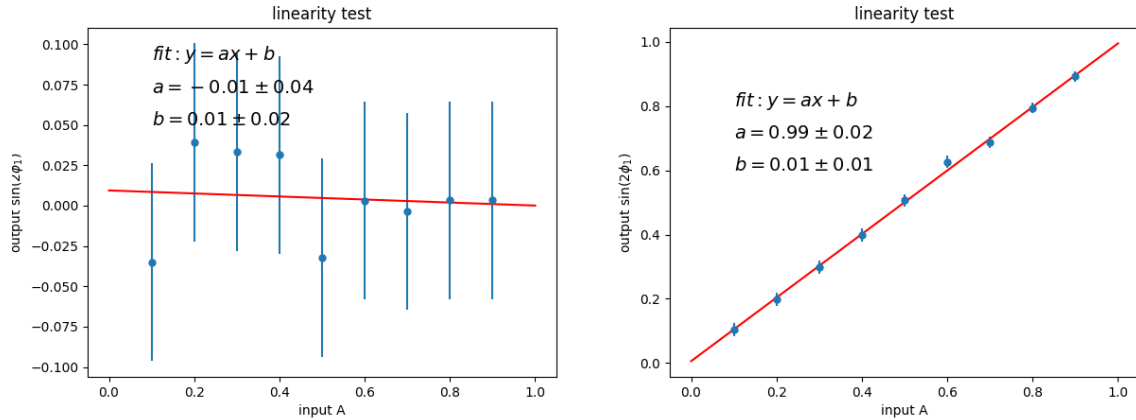


Figure 5-14: Linearity test of  $CP$  fit.

### 5.4.3 Toy MC Fit Pull

In order to check the fit bias with input-output method, a series of 1000 dataset of toy MC has been created containing about 26 events in each. The event number is set based on the expected number from signal region in data after the selection.  $\chi_2$ ,

$N$  and vertex errors on  $CP$  and tag-side are sampled from distribution of data. The fit to dataset has only  $\sin(2\phi_1)$  and  $\mathcal{A}$  as floating parameters, which input are both zero. We expect to use normal distribution to describe the pull of  $\sin(2\phi_1)$  and  $\mathcal{A}$ .

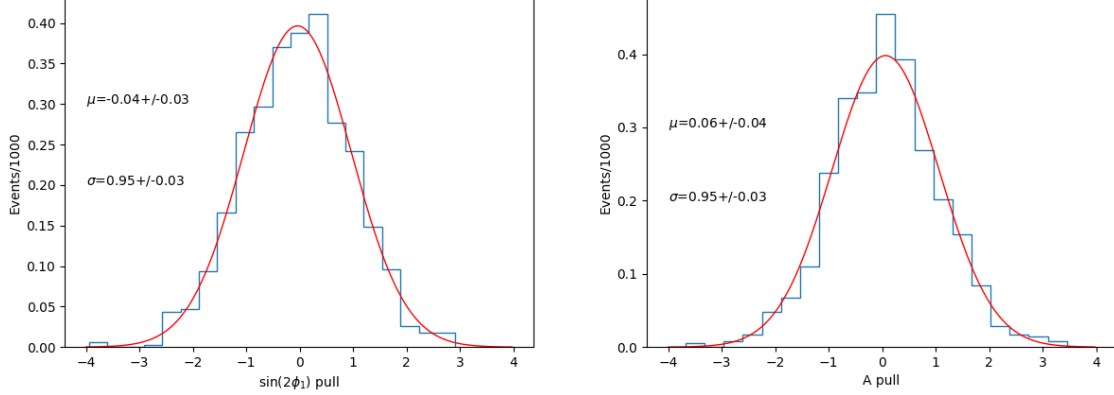


Figure 5-15: Pull of  $\sin(2\phi_1)$  and  $\mathcal{A}$  fitted.

The fit results shows a good recovery of input  $\sin(2\phi_1)$  and  $\mathcal{A}$  with no clear bias is spotted.

#### 5.4.4 Lifetime and $\Delta m_d$ Fit

Before looking at  $CP$  parameters in data, we need to check if the physics parameters are consistent when setting the  $CP$  fitter to fit them in float. To test lifetime fit, first we use 10000 signal MC events which is generated by  $\tau_{B^0} = 1.520$  from PDG value. The  $\sin(2\phi_1)$  and  $\mathcal{A}$  are fixed at zero during the fit, for which the generator level  $CP$  violation is zero. This is equivalent fit to:

$$\mathcal{P}(\Delta t, \tau_{B^0}) = \frac{e^{-|\Delta t|/\tau_{B^0}}}{4\tau_{B^0}} \quad (5.22)$$

The fit result is  $1.537 \pm 0.024$  ps which is consistent with the input. We perform the lifetime fit on data in signal region, the  $CP$  parameters are fixed based on PDG values to:  $\sin(2\phi_1) = 0.69$  and  $\mathcal{A} = 0$ . The fitted lifetime from  $B^0 \rightarrow K_S^0 K_S^0 K_S^0$  is  $1.431 \pm 0.382$  ps. The result is consistent with PDG value. The distribution of  $\Delta t$  in lifetime fit is shown as Fig 5-16. The  $B^0$  and  $B^+$  lifetime fit using control sample

is also performed and summarized in here[31]. The results are consistent with PDG values.

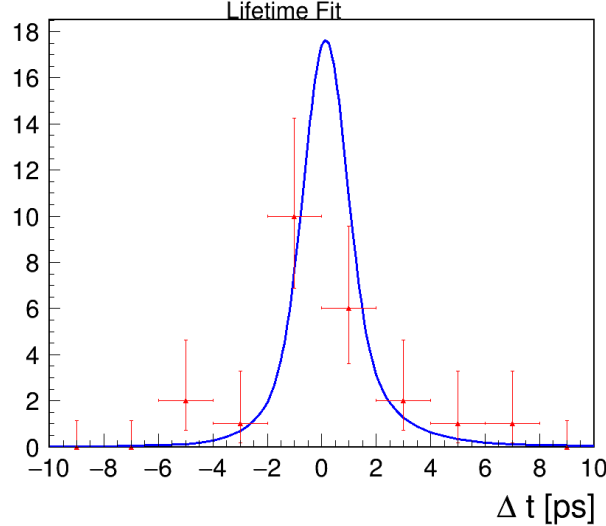


Figure 5-16: Lifetime fit on data

To test the fit on physics parameter  $\Delta m_d$ , we generate 200 toy MC sets of  $B^0 \rightarrow K_S^0 K_S^0 K_S^0$  with input  $\Delta m_d = 0.507 \text{ GeV}/c^2$  where each set contains 26 events as same as data. The fit result is close to normal distribution and the pull of  $\Delta m_d$  is shown in Fig 5-17.

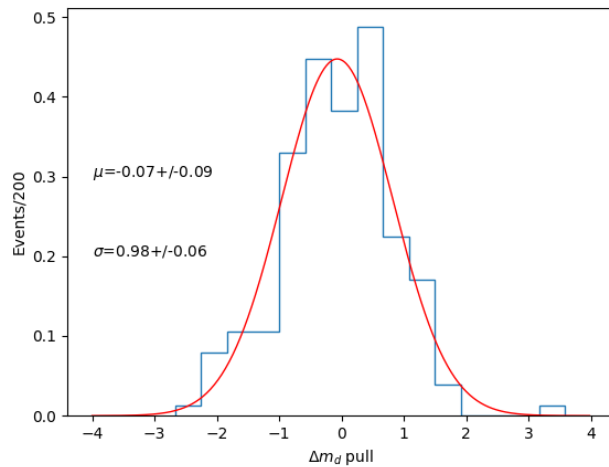


Figure 5-17: Pull of  $\Delta m_d$

## 5.5 $CP$ fit on data

After the  $CP$  fit procedures from the previous sections 5.1 to 5.5 is reviewed by Belle II collaboration, the permission of measuring  $CP$  parameters using Belle II 2019 and 2020 Spring/Summer data is granted by the review committee. The event number used for the  $CP$  fit is 26, and the fit result is shown as:

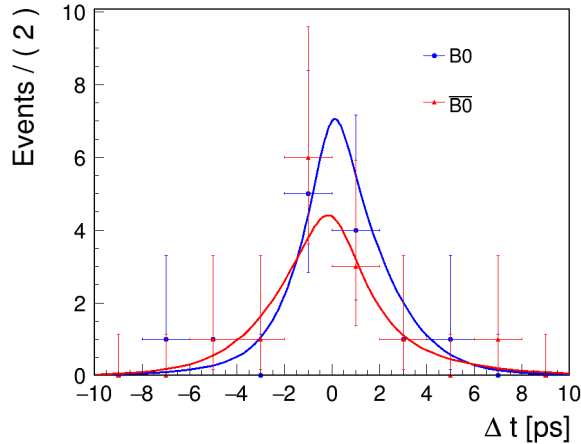


Figure 5-18: The  $CP$  fit from data.

The results of  $CP$  parameters are:

$$\begin{aligned} \sin(2\phi_1) &= 0.82 \pm 0.85(stat) \\ \mathcal{A} &= -0.21 \pm 0.28(stat) \end{aligned} \tag{5.23}$$

## 5.6 Systematic Uncertainty

The systematic uncertainty that affects the fit results may come from many aspects of the measurement setup. In this measurement considering the options we used for signal extraction, vertexing and fit strategy, the major systematic uncertainty receives contribution from following points:

- resolution functions parameters
- signal fraction

- flavor tagging
- background  $\Delta t$  shapes
- fit bias
- physics parameters

For the above sources of systematic uncertainty, if the parameters are defined with MC study, we float the value by  $\pm 2\sigma$  of their uncertainty, and if the parameters are defined by data, we float the value by  $\pm 1\sigma$ , to have a more robust estimation of impact on fit results. The impact of  $CP$  parameters are separately estimated from each sources with positive and negative differentials. With sum of the quadrature of each term, the overall systematic uncertainty is obtained.

The signal resolution functions' parameters are determined from MC study for signal component. The impact on fit results is summarized as follows:

Table 5.6: systematic uncertainty from resolution models

source	$+\delta\mathcal{S}$	$+\delta\mathcal{A}$	$-\delta\mathcal{S}$	$-\delta\mathcal{A}$
$f_{cp}^{tail}$	-0.000096	-0.000057	0.000014	0.000056
$s_0^{main}$	0.005443	0.001299	-0.005675	-0.001404
$s_1^{main}$	0.019934	-0.000903	-0.020204	0.000633
$s_0^{tail}$	-0.003233	-0.001623	0.00327	0.001596
$f_{tag}^{tail}$	0.00314	-0.001257	-0.003117	0.001266
$s_0^{main}$	0.002011	-0.001395	-0.001956	0.001398
$s_1^{main}$	0.005059	-0.00084	-0.004969	0.000825
$s_0^{tail}$	-0.000135	-0.000393	0.00010	0.000435
$s_1^{tail}$	0.000101	0.000027	-0.000472	0.000129
$f_\delta$	-0.007248	-0.000552	0.007231	0.000591
$f_p$	0.003037	0.004347	-0.003069	-0.004314
$\tau_n$	-0.00101	-0.002841	0.000937	0.00294
$\tau_p$	0.004497	0.002502	-0.004648	-0.002478

The background  $\Delta t$  shapes' parameters are determined from data sideband  $M_{bc} < 5.26$  GeV. The impact on fit results is summarized as follows:

Table 5.7: systematic uncertainty from background  $\Delta t$  shapes

source	$+\delta\mathcal{S}$	$+\delta\mathcal{A}$	$-\delta\mathcal{S}$	$-\delta\mathcal{A}$
$\mu_\delta^{bkg}$	-0.014294	-0.016581	0.006758	0.006537
$\mu_l^{bkg}$	-0.002798	-0.012567	0.003789	0.012783
$\tau_{bkg}$	0.001377	0.001689	-0.004159	0.000085
$f_\delta^{bkg}$	-0.011315	0.001365	0.011187	-0.001395
$f_{tail}^{bkg}$	-0.002661	0.00153	0.00248	-0.001368
$\sigma_{main}^{bkg}$	0.0207015	0.022041	-0.0236175	-0.01569
$\sigma_{tail}^{bkg}$	-0.000275	-0.000159	0.000179	0.000141

The flavor tagging parameters wrong tagging fraction  $w$  in each rbin is determined from signal MC. The impact in each rbin on fit results is summarized as follows:

Table 5.8: systematic uncertainty from wrong tagging fraction

source	$+\delta\mathcal{S}$	$+\delta\mathcal{A}$	$-\delta\mathcal{S}$	$-\delta\mathcal{A}$
$w_1$	-0.0018919	0.001911	0.0018549	-0.002004
$w_2$	-0.0016448	0.001104	0.0016085	-0.001155
$w_3$	-0.0004899	0.001344	0.0004726	-0.001341
$w_4$	0.0006556	0.000264	-0.0006542	-0.000255
$w_5$	-0.0001228	0.000204	0.0001225	-0.000195
$w_6$	0.0000948	0.000054	0.0000957	-0.000045
$w_7$	0.0001911	-0.000396	-0.0001907	0.000402

The physics parameters  $\Delta m_d$  and  $\tau_{B^0}$  uncertainties are included using the PDG average value. The impact on fit results is summarized as follows:

Table 5.9: systematic uncertainty from physics parameters

source	$+\delta\mathcal{S}$	$+\delta\mathcal{A}$	$-\delta\mathcal{S}$	$-\delta\mathcal{A}$
$\Delta m_d$	-0.001767	-0.000687	0.001778	0.000696
$\tau_{B^0}$	-0.004561	-0.000546	0.004565	0.000555

The signal fraction is determined using 2D fit results of  $M_{bc}$  and  $\Delta E$  from data. The impact on fit results is summarized as follows:

Table 5.10: systematic uncertainty from signal fraction

source	$+\delta\mathcal{S}$	$+\delta\mathcal{A}$	$-\delta\mathcal{S}$	$-\delta\mathcal{A}$
mu1_mbc	0.000822	-0.003888	-0.0007965	0.003849
sigma1_mbc	0.0004755	0.008442	-0.000628	-0.008733
m0_argus	-0.000707	0.00414	0.001448	-0.005781
c_argus	-0.005544	0.001449	0.000922	-0.000078
f1_de	0.0278255	0.020589	-0.0192365	-0.008409
f2_de	0.020809	0.017649	-0.0161285	-0.007005
mu1_de	-0.000443	-0.000153	0.0004955	0.000088
mu2_de	-0.000563	0.001446	0.0005905	-0.001446
mu3_de	-0.0031635	-0.000834	0.003354	0.000981
sigma1_de	-0.0001715	-0.000966	0.000206	0.000906
sigma2_de	-0.0031495	0.002958	0.0026345	-0.002475
sigma3_de	-0.001926	-0.00255	0.0024695	0.002985
a0_cheb	0.0009515	0.000057	-0.0008925	-0.000102
N_sig_f	-0.0046395	0.003987	0.004922	-0.003504

The fit bias uncertainties is determined by the fit error of 100k signal MC events, which is  $\delta\mathcal{S} = 0.0098$  and  $\delta\mathcal{A} = 0.0057$ .

## 5.7 Summary

The  $CP$  parameters measurement study targeting the extraction of asymmetry parameters  $\mathcal{S}$  and  $\mathcal{A}$  has been conducted. Based on physical  $\Delta t$  distribution, the model for  $CP$  fit have been properly built. Importantly, corresponding resolution functions for  $\mathcal{P}_{sig}$  and  $\mathcal{P}_{bkg}$  are built by separating smearing effects from  $CP$  and tag side. All the fits takes advantage of event-by-event conditional fit so the model has a good robustness in different measurement quality cases. As for flavor tagging, an algorithm based on FBDT classification is developed and implemented to give the estimated dilution factor  $r$ . To take a good use of these information, a Belle II  $CP$  fitter is developed to perform the fit on desired parameters. The linearity test and fit pull test shows a reliable performance of the fitter using toy MC study. The actual fit on lifetime using data is also consistent with the PDG value with a relatively large uncertainty due to very small amount of data.

After the blind fit and test for the  $CP$  parameters measurement is conducted, with the permission from Belle II collaboration, we unblind the data in signal box and perform the  $CP$  fit to extract  $\mathcal{S}$  and  $\mathcal{A}$ . Also, the major sources of systematic uncertainty is estimated. The primary result of  $CP$  parameters in this low luminosity stage are:

$$\begin{aligned}\mathcal{S} &= -\sin(2\phi_1) = -0.82 \pm 0.85(stat) \pm 0.07(syst) \\ \mathcal{A} &= -0.21 \pm 0.28(stat) \pm 0.06(syst)\end{aligned}\tag{5.24}$$

The results are dominated by the statistical uncertainty due to the very limited data sample in early stage of Belle II. Under such large uncertainty, the results is in an agreement with the Standard Model.



# Chapter 6

## Conclusion and Prospective

The Belle II experiment is built upon the success of its predecessor Belle and many other great efforts of exploring the mysteries of flavor physics, which have expand our knowledge and understanding of elementary particle physics. One of the most outstanding outcome of these efforts is the Standard Model, which it's capable of well describing a variety of experimental results in a large energy scale and fine precision for the past few decades. And yet open questions that still draws attention from particle physicists remain, wait to be discovered as New Physics. One of the most important question is that why the universe is mass-dominated while anti-matter seems to be vanished.

Belle II is aimed to search for New Physics through the precise measurements of related topics in heavy flavor physics at the world-record luminosity frontier. SuperKEKB accelerator is designed with asymmetric beam energies to provide a boost to the center-of-mass system and thereby allow for time-dependent  $CP$  symmetry violation measurements. The products of collision is in a very clean environment, with 40 times higher luminosity of peak at Belle. This create excellent opportunities for physicists to look for the undiscovered source of  $CP$  violation, for which the existing explanation from the complex phase of CKM matrix can't described the observed level of asymmetry in our universe.

$b \rightarrow s$  transition is an important flavor coupling process to be examined in search for New Physics. The  $CP$  violation in such process was first observed after the

precise measurement in  $b \rightarrow c$  with a small tension. So far the precision of the measurement of  $CP$  parameter  $\mathcal{S}$  in  $b \rightarrow s$  is still in an arguable difference with tree-level process considering the existing uncertainty, which allows a decent margin for New Physics. The representative processes of  $b \rightarrow s$  are resonant decay such as  $B^0 \rightarrow \eta' K_S^0$ ,  $B^0 \rightarrow \phi K_S^0$  and decay like  $B^0 \rightarrow K_S^0 K_S^0 K_S^0$ , on which Belle II experiment will have an excellent prospective sensitivity.

This thesis presents the first attempt to study the time-dependent  $CP$  violation in  $B^0 \rightarrow K_S^0 K_S^0 K_S^0$  using early phase 3 data of Belle II and latest MC sample. In order to reconstruct clean signal sample of  $B^0$ ,  $K_S^0$  reconstruction performance is critical because of the unique characteristics of this decay. A KsFinder based on FastBDT classification algorithm is developed to offer a goodness indicator of traditional cut-based reconstruction of  $K_S^0$ . The performance of this new KsFinder is validated to have a great background rejection power at with small signal loss in the maximum FOM case.  $B^0$  are reconstructed with a good significance even with very low statistics with a good agreement with MC prediction and Belle experience. The overall efficiency of  $B^0$  is slightly improved than Belle with slightly higher beam background condition in current Belle II. The measurement of the  $CP$  fit is conducted based on the reconstruction. The  $CP$  fit using artificial model containing resolution functions from different sources are built with precise study of MC signal samples and the data sideband . As for flavor tagging information, wrong fraction as mandatory parameters in signal  $\Delta t$  distribution, are implemented too. The coefficient of signal and background in the  $CP$  fit model is determined by the signal extraction 2D fit over  $M_{bc}$  and  $\Delta E$ . For each event, the signal fraction is calculated based on the  $M_{bc}$  and  $\Delta E$  using the 2D fit model, which is used as a discrete observable in  $CP$  fit model.

Before performing  $CP$  fit on data, blind fit study and fit pull/linearity test are conducted to validate the fit model and procedures. In MC fit test, fit results for  $CP$  parameters are consistent with the generation level input. The linearity and fit pull test shows the reasonably good performance of extracting  $\mathcal{S}$  and  $\mathcal{A}$ . The validation of data using  $CP$  fitter to fit  $B^0$  lifetime and mass width are also in a good agreement with PDG value in this low statistics case.

After the  $CP$  fit procedures are validated and the permission from Belle II collaboration of fitting on data is given, the  $CP$  parameters  $\mathcal{S}$  and  $\mathcal{A}$  measurement using Belle II early phase 3 data (2019 and 2020 Spring/Summer) is performed with the result as below:

$$\begin{aligned}\mathcal{S} &= -\sin(2\phi_1) = -0.82 \pm 0.85(stat) \pm 0.07(syst) \\ \mathcal{A} &= -0.21 \pm 0.28(stat) \pm 0.06(syst)\end{aligned}\tag{6.1}$$

The result is in a consistent with the PDG value and the prediction of the Standard Model, and also with the previous results from Belle and Babar as Chapter 1 described. The systematics study is also performed considered on the majority of contributing sources at this moment. The result is primary limited in precision due to the large statistical uncertainties from very low data collection.

What is worth of noticing is, many analysis tools that are required by performing the  $CP$  measurement on this channel is in a good stage of development. The decay mode being successfully re-discovered under very low data collection mostly thank to the newly developed  $K_S^0$  classification software, KsFinder, which will also be an essential asset in neutral particles dominated channels like  $B^0 \rightarrow K_S^0 K_S^0 K_S^0$ . The Belle II experiment is crucial in these channels because of the cleaner background environment and better sensitivity compared with LHCb. Besides, an artificial model on the vertex resolution, or called  $\Delta t$  resolution has been finely studied using MC sample and sideband data. Several important dependence or behaviors of vertexing tools in the Belle II detector is understood to a good extension in the early phase of Belle II. Further, a new  $CP$  fitter which is based on these studies is built and being validated, which will provide a multi-functional analysis tool for Belle II time-dependent  $CP$  violation study in future.

This study has shown a good potential of performing  $CP$  measurement in Belle II for the incoming years with more and more data recorded. The precision on  $\mathcal{S}$  in  $b \rightarrow s$  penguin-modes is highly depending on the large luminosity as Fig 1-9 shows, which the current precision fits in the expectation. Along with the data collection

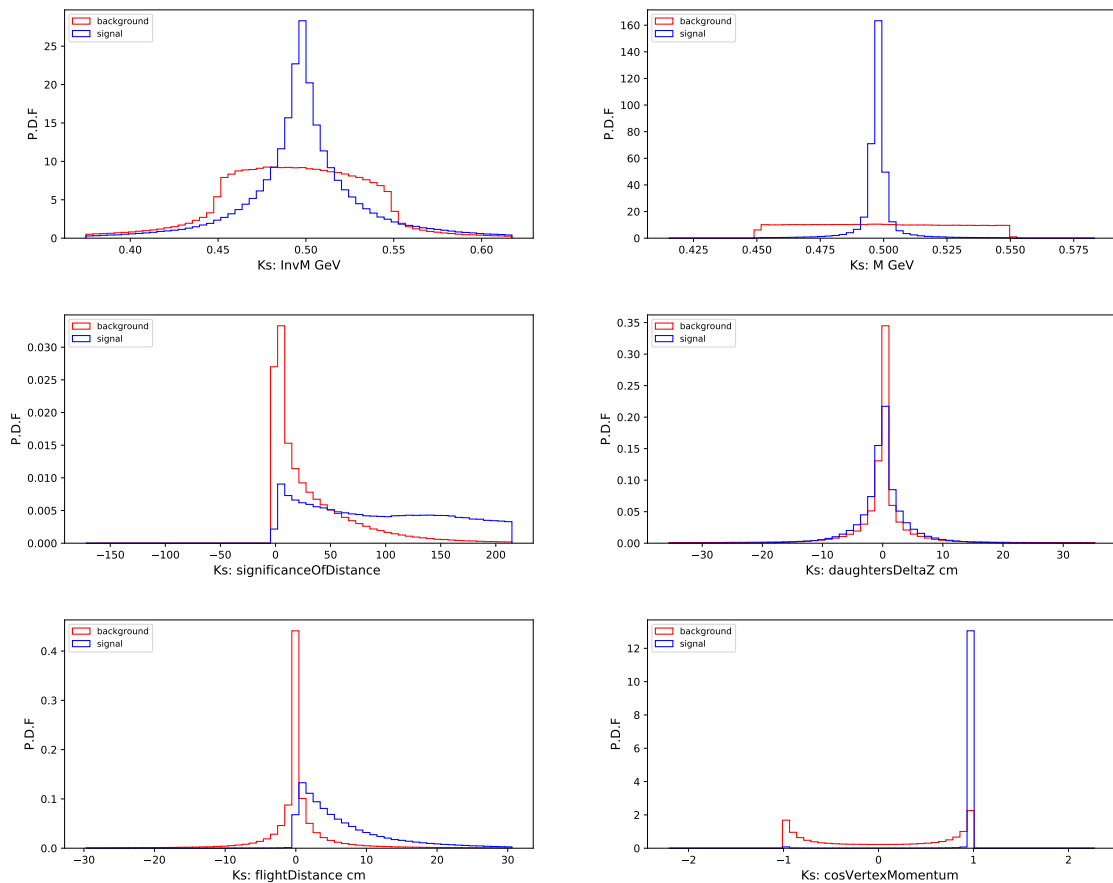
continues, we will be able to finely test and improve the analysis strategies and tools to a better stage using data, such as improving the reconstruction efficiency and purity of  $B^0$  when the luminosity ramps up to much higher level with much higher backgrounds. At integral luminosity at  $50 \text{ ab}^{-1}$  level, the statistical uncertainty of this decay on  $\Delta\mathcal{S}$  would be trimmed down to a comparable value around 0.03 which is close the Standard Model correction, offering a much better probe on whether New Physics is influential at this level of precision. The progress that has been made so far in this thesis paves a well-constructed and solid path towards future results. From the current result, the chance of having a much precised measurement in the next a few years on this channel is very promising and searching New Physics effect in penguin-mode  $b \rightarrow s$  transition from Belle II is proven to be an exciting and important topic.

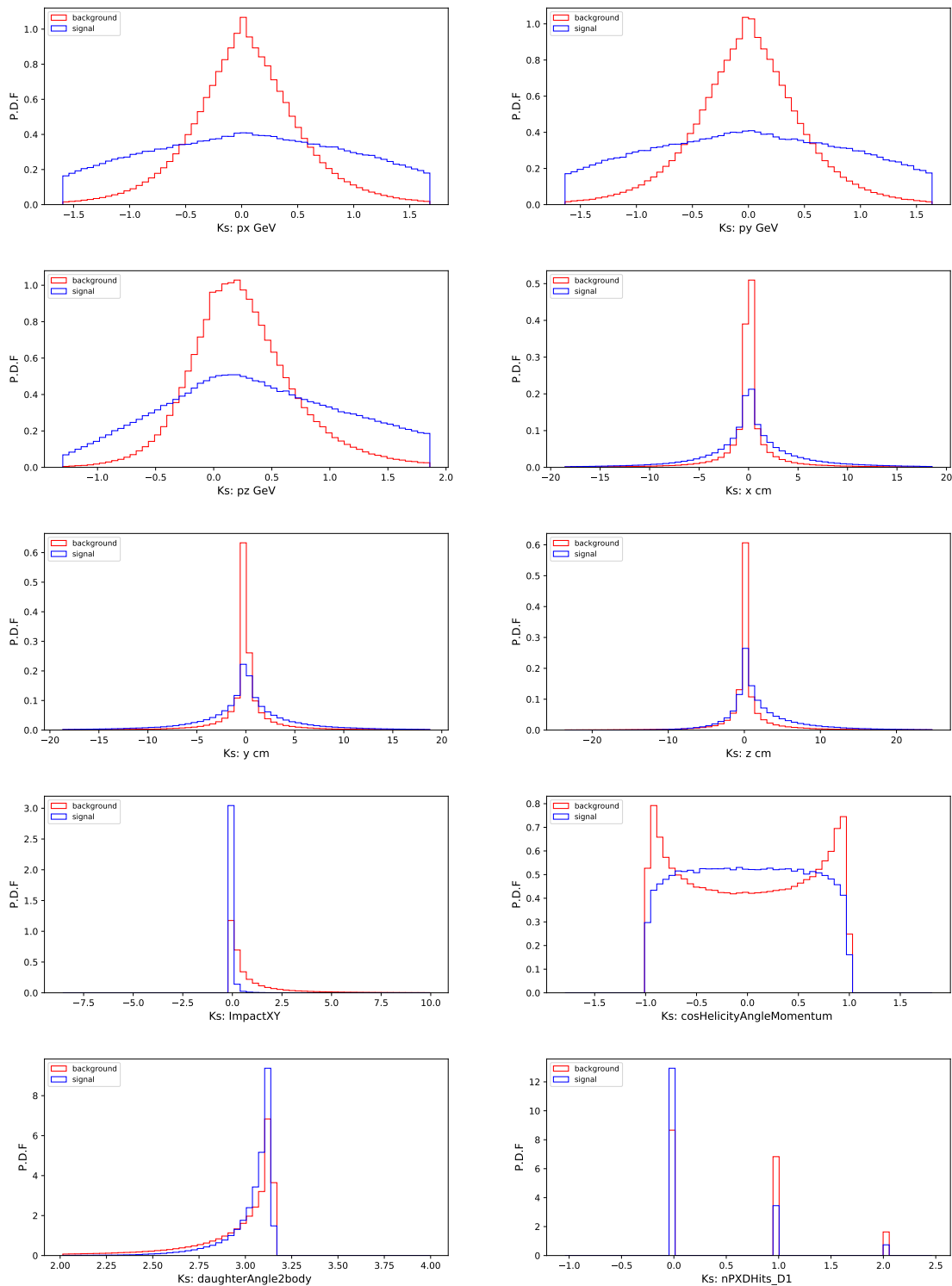


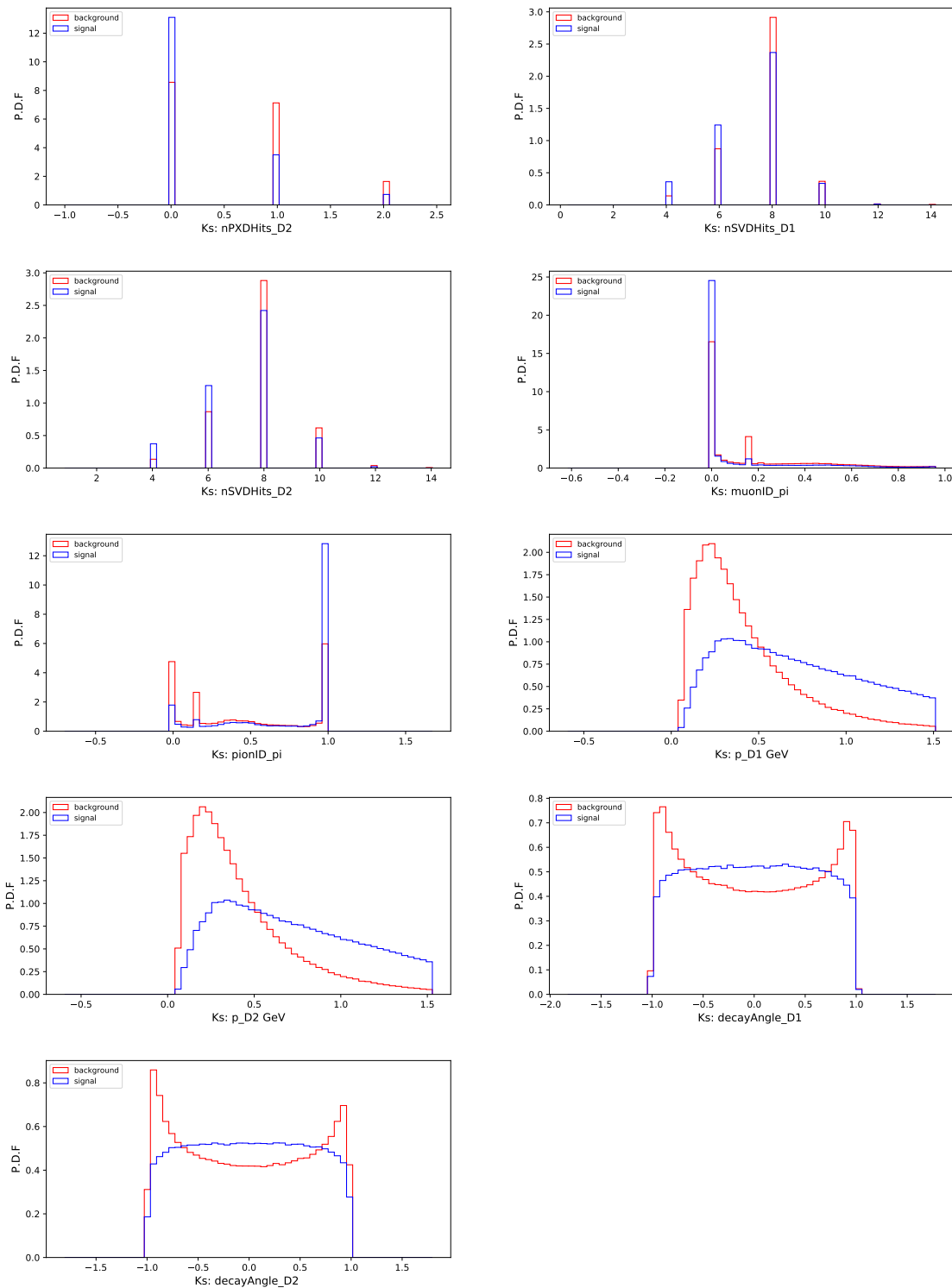
# Appendix A

## Training Observables for $K_S^0$ Classifier

Figure A-1: The distribution of Ks training variables. The red is from fake  $K_S^0$  and the blue is from true  $K_S^0$





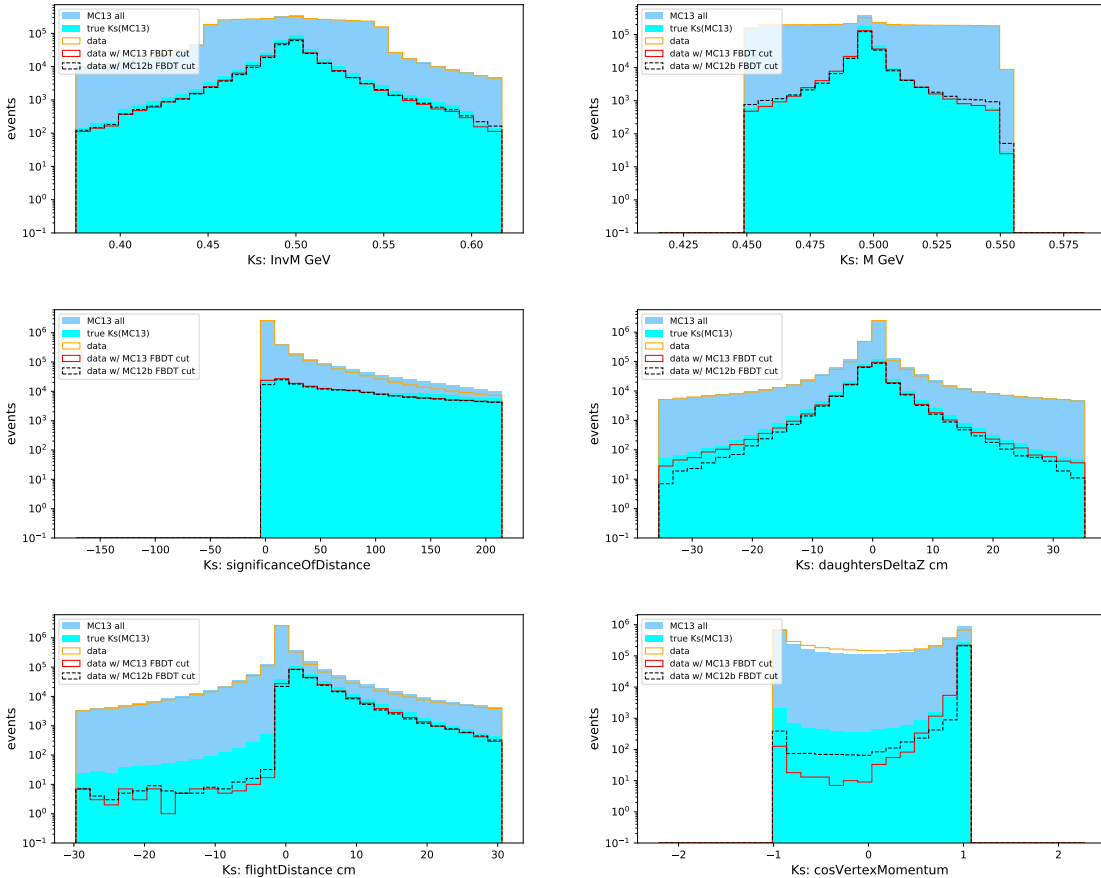


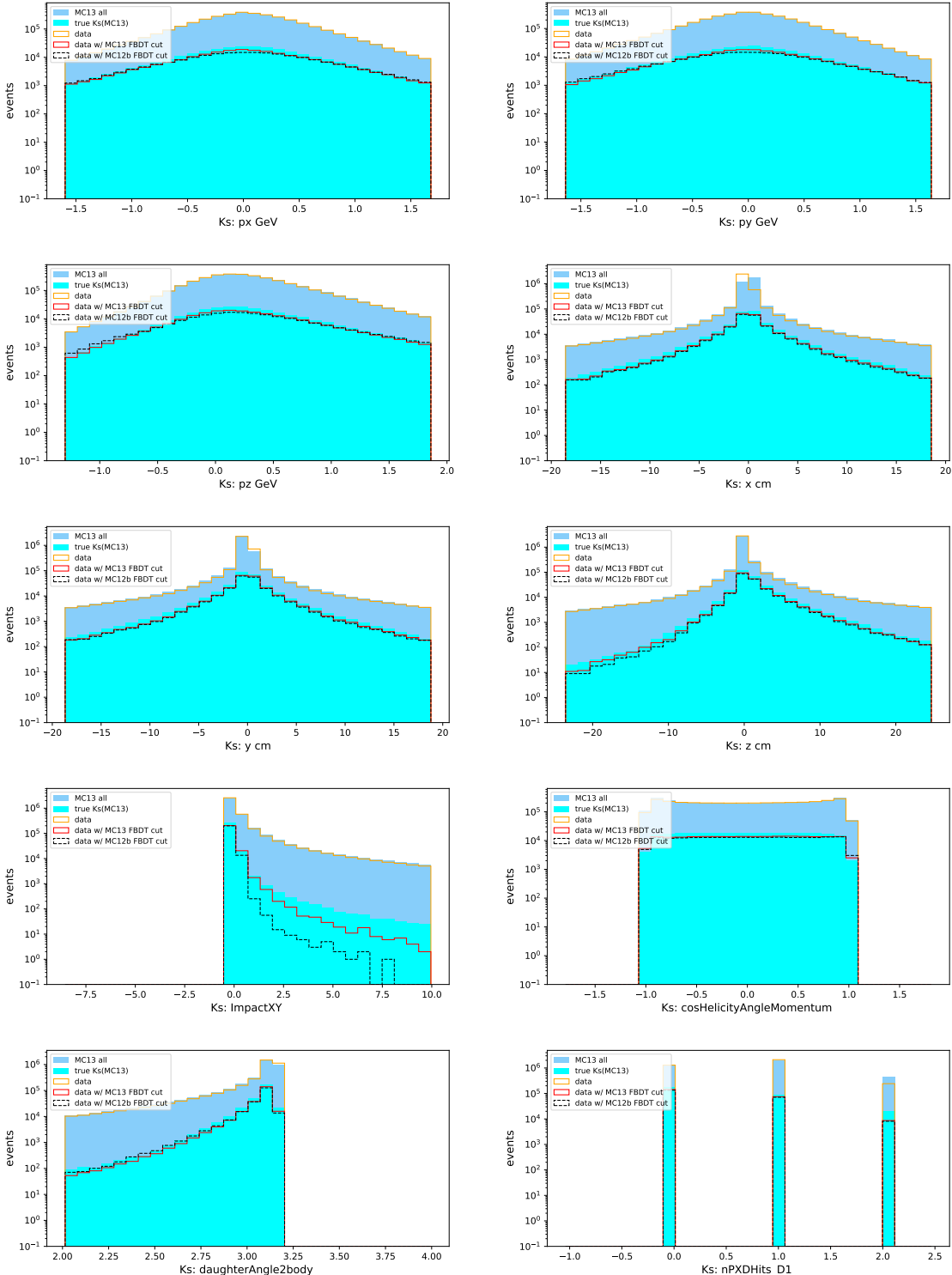


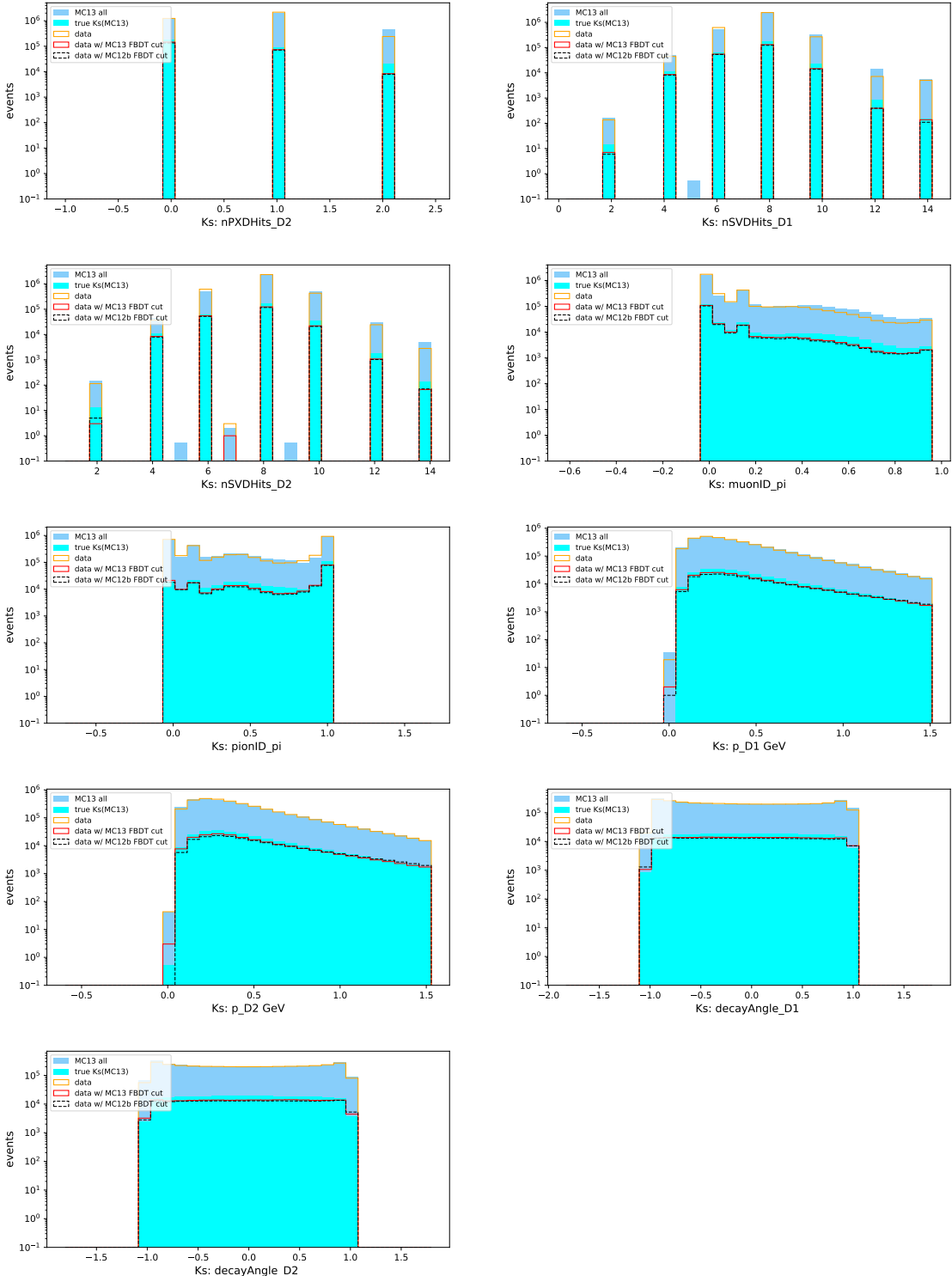
## Appendix B

# Data Validation Plots for $K_S^0$

Figure B-1: The distribution of variables used in KsFinder classification. The variables abbreviation can be referenced from Table III. The yellow solid lines are  $K_S^0$  from data without KsFinder, and red solid lines are  $K_S^0$  with KsFinder using MC13a for training. The black dashed lines are  $K_S^0$  with KsFinder using MC12b (run-dependent). Blue histogram is from MC13a without KsFinder and cyan histogram is from MC13a with KsFinder.







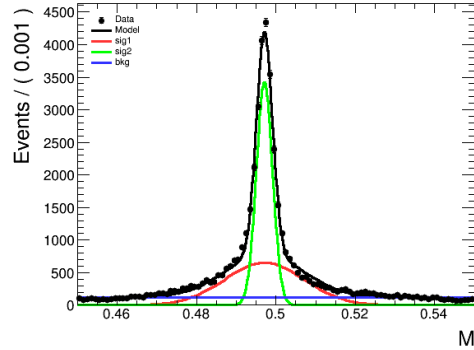


# Appendix C

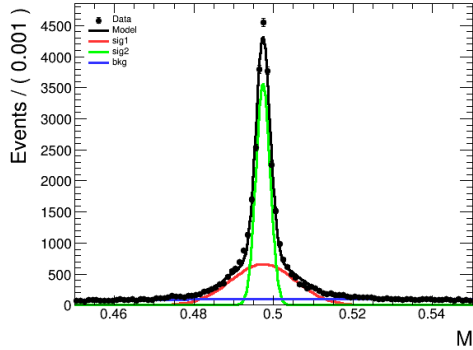
## $K_S^0$ mass fit with varied cut value

Figure C-1: Double-gaussian shape and 1st-poly are used for fitting signal and background  $K_S^0$  invariant mass under varies KsFinder cut values respectively. The data and MC are separately fitted to compared the yield in each cut, which defines the correction.

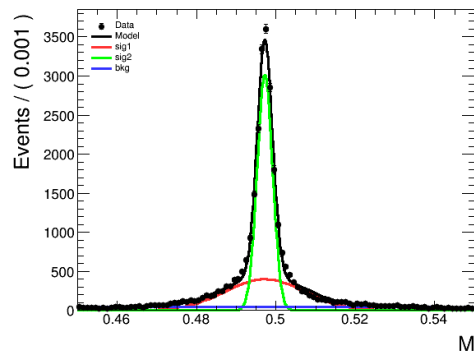
a) Data, cut=0.2



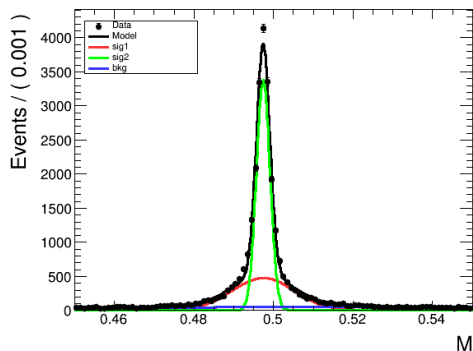
b) MC, cut=0.2



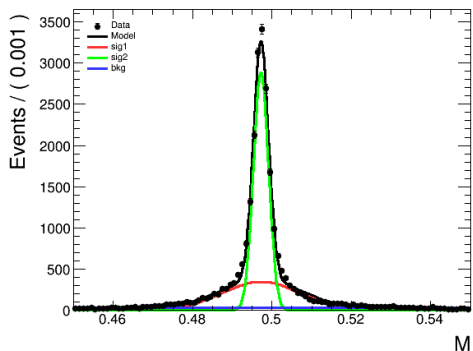
c) Data, cut=0.4



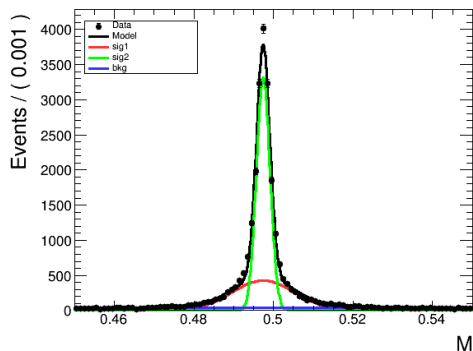
d) MC, cut=0.4



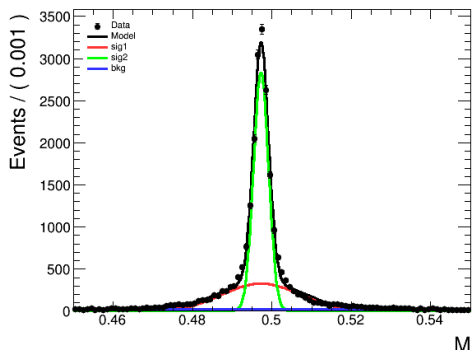
e) Data, cut=0.5



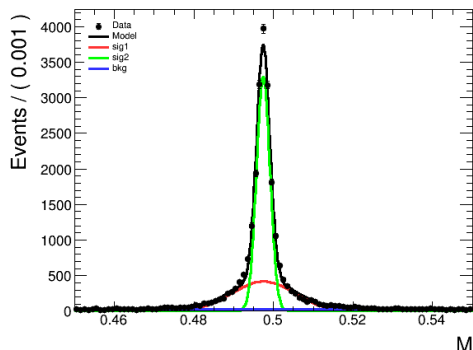
f) MC, cut=0.5



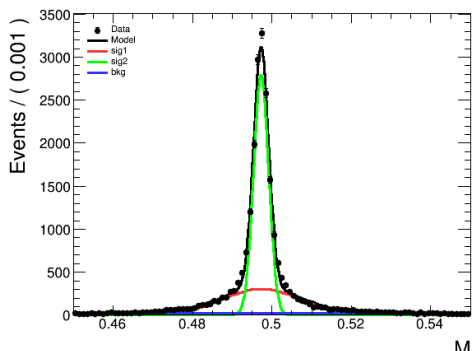
g) Data, cut=0.55



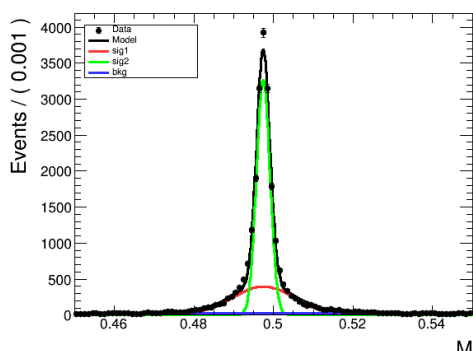
h) MC, cut=0.55



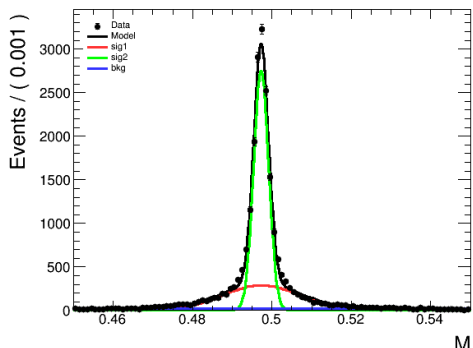
i) Data, cut=0.6



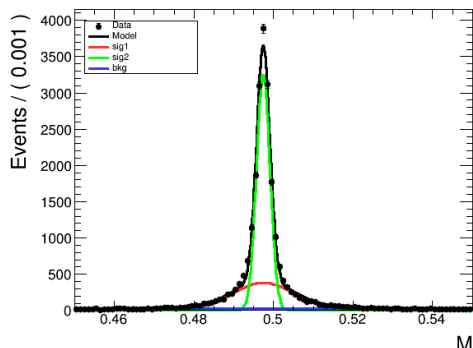
j) MC, cut=0.6



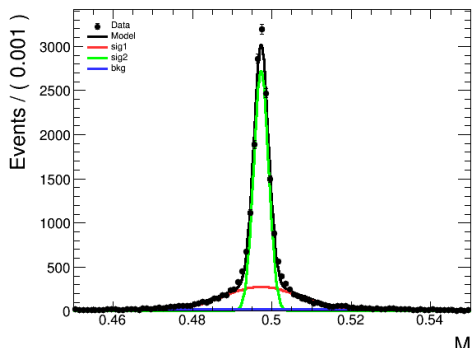
k) Data, cut=0.65



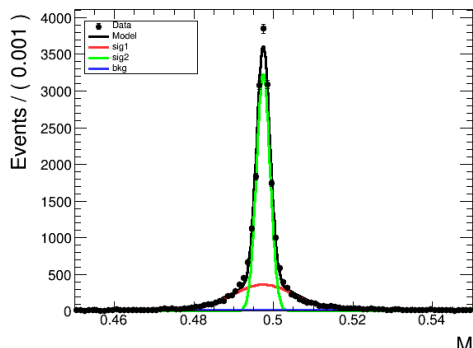
l) MC, cut=0.65



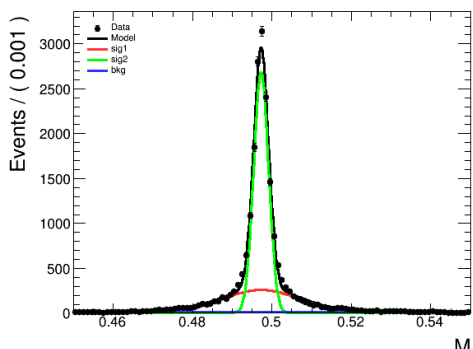
m) Data, cut=0.7



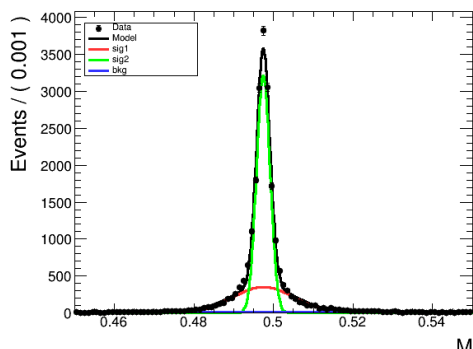
n) MC, cut=0.7



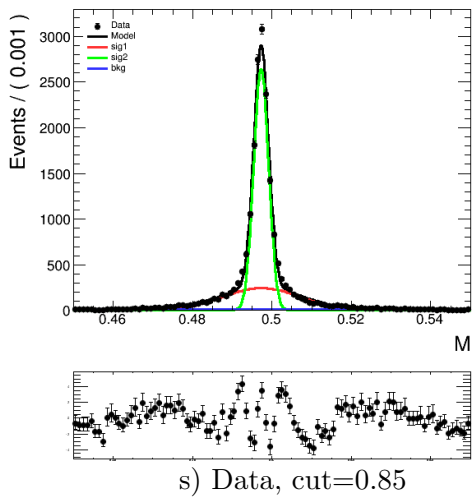
o) Data, cut=0.75



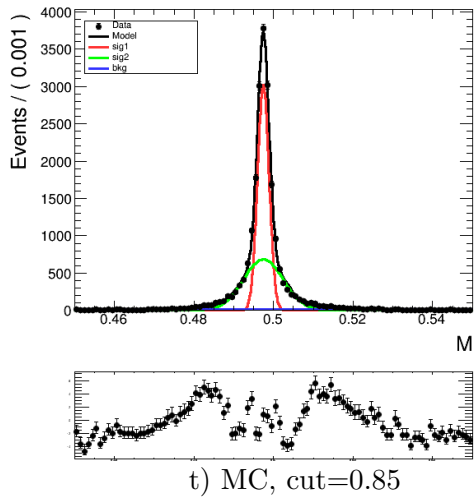
p) MC, cut=0.75



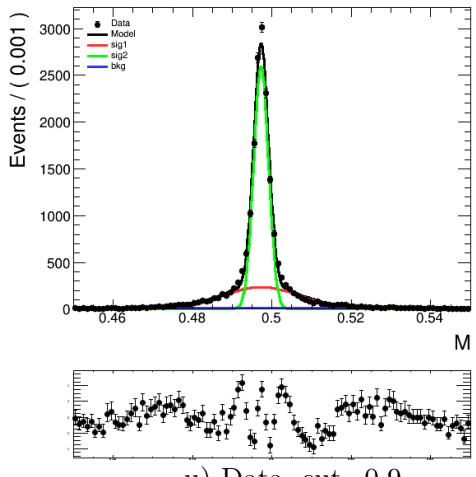
q) Data, cut=0.8



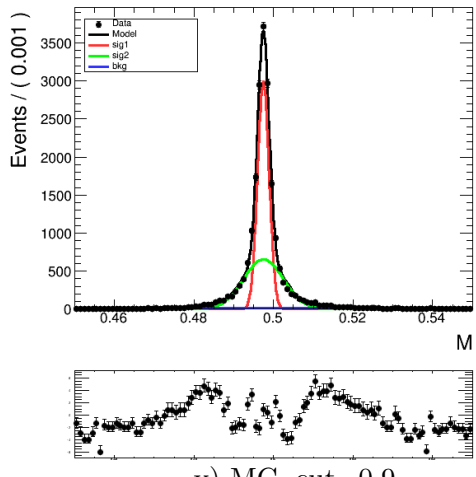
r) MC, cut=0.8



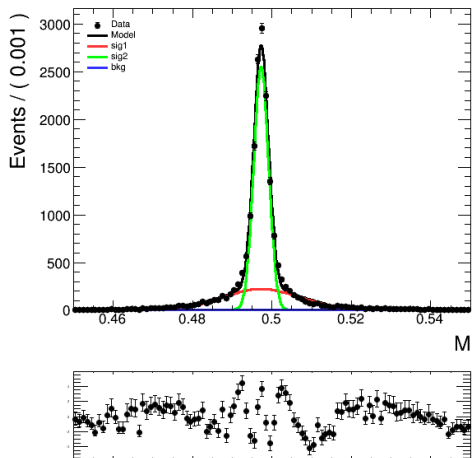
s) Data, cut=0.85



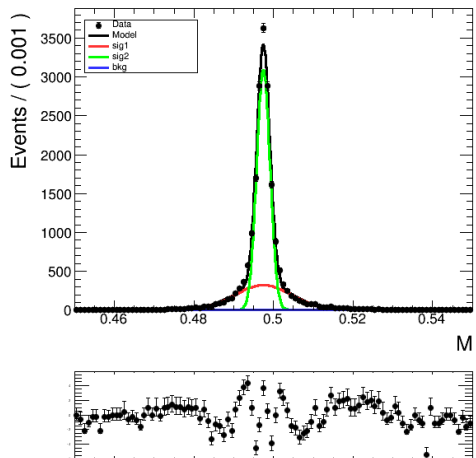
t) MC, cut=0.85



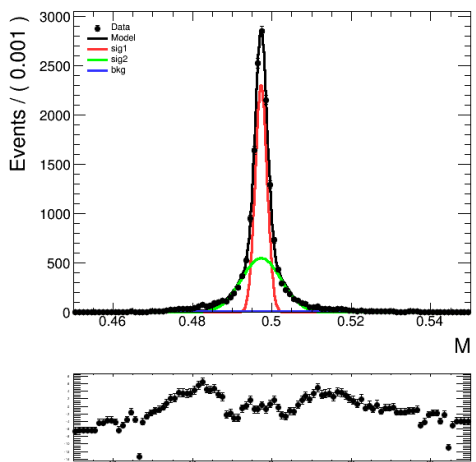
u) Data, cut=0.9



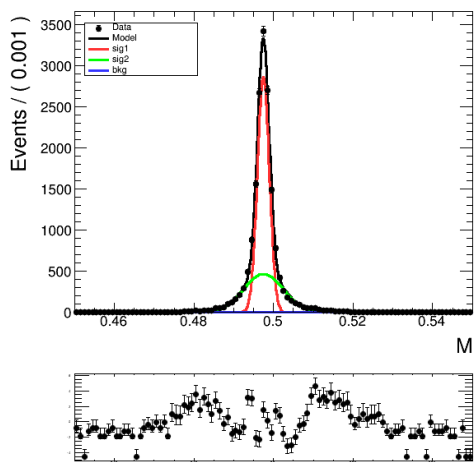
v) MC, cut=0.9



w) Data, cut=0.95



x) MC, cut=0.95



# Bibliography

- [1] wikipedia. Elementary particles in the Standard Model. [https://en.wikipedia.org/wiki/File:Standard\\_Model\\_of\\_Elementary\\_Particles\\_Anti.svg](https://en.wikipedia.org/wiki/File:Standard_Model_of_Elementary_Particles_Anti.svg), 2012.
- [2] Emmy Noether. Invariant variation problems. *Transport Theory and Statistical Physics*, 1(3):186–207, Jan 1971. doi:10.1080/00411457108231446.
- [3] T. D. Lee and C. N. Yang. Question of parity conservation in weak interactions. *Phys. Rev.*, 104:254–258, Oct 1956. doi:10.1103/PhysRev.104.254. URL <https://link.aps.org/doi/10.1103/PhysRev.104.254>.
- [4] C. S. Wu, E. Ambler, R. W. Hayward, D. D. Hoppes, and R. P. Hudson. Experimental test of parity conservation in beta decay. *Phys. Rev.*, 105:1413–1415, Feb 1957. doi:10.1103/PhysRev.105.1413. URL <https://link.aps.org/doi/10.1103/PhysRev.105.1413>.
- [5] Makoto Kobayashi and Toshihide Maskawa. CP-Violation in the Renormalizable Theory of Weak Interaction. *Progress of Theoretical Physics*, 49(2):652–657, 02 1973. ISSN 0033-068X. doi:10.1143/PTP.49.652. URL <https://doi.org/10.1143/PTP.49.652>.
- [6] ckmfitter. Results of the global CKM fit in the large complex plane. [http://ckmfitter.in2p3.fr/www/results/plots\\_summer19/ckm\\_res\\_summer19.html](http://ckmfitter.in2p3.fr/www/results/plots_summer19/ckm_res_summer19.html), 2019.
- [7] Amol Dighe, Tobias Hurth, Choong Sun Kim, and Tadashi Yoshikawa. The width difference of  $b_d$  mesons, 2001.
- [8] Julian Tarek Wishahi. *Measurement of CP Violation in  $B^0 \rightarrow J/\psi K_S^0$  Decays with the LHCb Experiment*. PhD thesis, Dortmund U., 2014.
- [9] E Kou, P Urquijo, W Altmannshofer, F Beaujean, G Bell, M Beneke, I I Bigi, F Bishara, M Blanke, C Bobeth, and et al. The belle ii physics book. *Progress of Theoretical and Experimental Physics*, 2019(12), Dec 2019. ISSN 2050-3911. doi:10.1093/ptep/ptz106. URL <http://dx.doi.org/10.1093/ptep/ptz106>.
- [10] K-F Chen, K Hara, M Hazumi, T Higuchi, K Miyabayashi, Y Nakahama, K Sumisawa, O Tajima, Y Ushiroda, Y Yusa, et al. Observation of time-dependent c p

- violation in  $b^0 \rightarrow \eta'$   $k^0$  decays and improved measurements of c p asymmetries in  $b^0 \rightarrow \varphi k^0$ ,  $k^+_s k^-_s k^0$  and  $b^0 \rightarrow j/\psi k^0$  decays. *Physical review letters*, 98(3):031802, 2007.
- [11] Tim Gershon and Masashi Hazumi. Time-dependent cp violation in  $b^0 \rightarrow p^0 p^0 x^0$  decays. *Physics Letters B*, 596(3-4):163–172, 2004.
  - [12] Martin Beneke. Corrections to  $\sin(2\beta)$  from cp asymmetries in  $b^0 \rightarrow (\pi^0, \rho^0, \eta, \eta', \omega, \phi) k^0$  decays. *Physics Letters B*, 620(3-4):143–150, 2005.
  - [13] KH Kang, H Park, T Higuchi, K Miyabayashi, K Sumisawa, I Adachi, JK Ahn, H Aihara, S Al Said, DM Asner, et al. Measurement of time-dependent cp violation parameters in  $b^0 \rightarrow k_s k_s k_s$  decays at belle. *arXiv preprint arXiv:2011.00793*, 2020.
  - [14] J. P. Lees et al. Amplitude analysis and measurement of the time-dependent CP asymmetry of  $B^0 \rightarrow K_S^0 K_S^0 K_S^0$  decays. *Phys. Rev. D*, 85:054023, 2012. doi:10.1103/PhysRevD.85.054023.
  - [15] T. Abe et al. Belle II Technical Design Report. 2010. arXiv:1011.0352.
  - [16] Giacomo De Pietro. First data at belle ii and dark sector physics. *arXiv preprint arXiv:1808.00776*, 2018.
  - [17] Caitlin MacQueen, Belle II collaboration, et al. Dark sector physics at belle ii. In *Journal of Physics: Conference Series*, volume 1468, page 012047. IOP Publishing, 2020.
  - [18] URL <https://root.cern/>.
  - [19] T. Kuhr, C. Pulvermacher, M. Ritter, T. Hauth, and N. Braun. The belle ii core software. *Computing and Software for Big Science*, 3(1), Nov 2018. ISSN 2510-2044. doi:10.1007/s41781-018-0017-9. URL <http://dx.doi.org/10.1007/s41781-018-0017-9>.
  - [20] URL <https://evtgen.hepforge.org/doc/models.html>.
  - [21] URL <https://pdglive.lbl.gov/Particle.action?init=0&node=S042&home=MXXX045>.
  - [22] URL <https://confluence.desy.de/display/BI/Phase+3+luminosity+monitoring>.
  - [23] J-F Krohn, F Tenchini, P Urquijo, F Abudinén, S Cunliffe, T Ferber, M Gelb, J Gemmler, P Goldenzweig, T Keck, et al. Global decay chain vertex fitting at belle ii. *Nuclear Instruments and Methods in Physics Research Section A: Accelerators, Spectrometers, Detectors and Associated Equipment*, 976:164269, 2020.

- [24] M Feindt and U Kerzel. The neurobayes neural network package. *Nuclear Instruments and Methods in Physics Research Section A: Accelerators, Spectrometers, Detectors and Associated Equipment*, 559(1):190–194, 2006.
- [25] Thomas Keck. Fastbdt: A speed-optimized and cache-friendly implementation of stochastic gradient-boosted decision trees for multivariate classification. *arXiv preprint arXiv:1609.06119*, 2016. URL <https://arxiv.org/pdf/1609.06119.pdf>.
- [26] L Breiman J Friedman RA Olshen and CJ Stone. Classification and regression trees. statistics/probability series, 1984.
- [27] Jerome H Friedman. Stochastic gradient boosting. *Computational statistics & data analysis*, 38(4):367–378, 2002.
- [28] Jerome H Friedman. Greedy function approximation: a gradient boosting machine. *Annals of statistics*, pages 1189–1232, 2001. URL [https://projecteuclid.org/download/pdf\\_1/euclid-aos/1013203451](https://projecteuclid.org/download/pdf_1/euclid-aos/1013203451).
- [29] Tenchini, Francesco and Krohn, Jo-Frederik. Decay chain reconstruction at belle ii. *EPJ Web Conf.*, 214:06023, 2019. doi:10.1051/epjconf/201921406023. URL <https://doi.org/10.1051/epjconf/201921406023>.
- [30] A. J. Bevan, B. Golob, Th. Mannel, S. Prell, B. D. Yabsley, H. Aihara, F. Anulli, N. Arnaud, T. Aushev, M. Beneke, and et al. The physics of the b factories. *The European Physical Journal C*, 74(11), Nov 2014. ISSN 1434-6052. doi:10.1140/epjc/s10052-014-3026-9. URL <http://dx.doi.org/10.1140/epjc/s10052-014-3026-9>.
- [31] URL <https://docs.belle2.org/record/1941/files/BELLE2-NOTE-PH-2020-027.pdf>.
- [32] URL [https://docs.belle2.org/record/1905/files/BELLE2-NOTE-PH-2020-013\\_v3.2.pdf?version=1](https://docs.belle2.org/record/1905/files/BELLE2-NOTE-PH-2020-013_v3.2.pdf?version=1).